**Phd Thesis**
**Doctoral Program in Physics**

# Electronic Spin Transport and Thermoelectric Effects in Graphene

**Ingmar Neumann**

Thesis Director
**Prof. Sergio O. Valenzuela**

Tutor
**Prof. Jordi Pascual i Gainza**

**Institut Català de Nanotecnologia**
**Universitat Autònoma de Barcelona**

Bellaterra, 2014

Für meine Eltern

# Contents

**1. Introduction** **1**

**2. Theoretical Background** **5**
2.1. Introduction . . . 5
2.2. Electrical and Thermal Conduction in Metals . . . 5
2.3. Magnetism in Solid State Physics and Electronics . . . 7
2.3.1. Stoner Wolfarth Model . . . 7
2.3.2. Magnetoresistance . . . 8
2.4. Spin Accumulation . . . 9
2.5. Non Local Spin Injection and Detection . . . 12
2.5.1. Motivation . . . 12
2.5.2. System . . . 12
2.5.3. Derivation of the Diffusion Equation . . . 14
2.5.4. Interfacial Currents . . . 15
2.5.5. Spin Dependent Voltage . . . 16
2.6. Hanle Spin Precession . . . 18
2.7. Spin Caloritronics . . . 20
2.8. Graphene . . . 23
2.8.1. Introduction . . . 23
2.8.2. Band Structure of Graphene in the Tight Binding Approach . . . 23
2.8.3. The Electric Field Effect . . . 26
2.8.4. Mobility . . . 29
2.9. Spin Relaxation in Graphene . . . 30
2.9.1. Introduction . . . 30
2.9.2. Elliot-Yafet Spin Relaxation . . . 31
2.9.3. D‘yakonov-Perel Spin Relaxation . . . 32
2.9.4. Comparison between EY and DP Mechanism . . . 33
2.9.5. Experimental Results . . . 34
2.9.6. Further Mechanisms of Spin Relaxation in Graphene . . . 34

**3. Experimental Techniques and Methods** **37**
3.1. Introduction . . . 37
3.2. Fabrication and Characterization of Single Layer Graphene . . . 37
3.2.1. Mechanical Exfoliation . . . 37

3.2.2. Optical Characterization and Raman Spectroscopy . . . . . . . 38
3.2.3. AFM characterization . . . . . . . . . . . . . . . . . . . . . . . 39
3.3. Properties of Crosslinked PMMA . . . . . . . . . . . . . . . . . . . . . 41
3.3.1. Crosslinking PMMA . . . . . . . . . . . . . . . . . . . . . . . . 41
3.3.2. Choosing the Stepsize . . . . . . . . . . . . . . . . . . . . . . . 42
3.3.3. Choosing the Electron Beam Dose . . . . . . . . . . . . . . . . . 44
3.3.4. Creating trenches in overexposed PMMA . . . . . . . . . . . . . 46
3.3.5. Controlling the Height Profile of the Polymer Substrate . . . . . 46
3.4. Fabrication and Engineering of Nanodevices . . . . . . . . . . . . . . . 48
3.4.1. Advantages of Electron Beam Lithography . . . . . . . . . . . . 48
3.4.2. Standard Electron Beam Lithography . . . . . . . . . . . . . . . 50
3.4.3. Graphene spin valve devices . . . . . . . . . . . . . . . . . . . . 50
3.4.4. Using Crosslinked PMMA as a substrate . . . . . . . . . . . . . 52
3.4.5. Suspended Graphene Spin Valves . . . . . . . . . . . . . . . . . 53
3.5. Measurement setup . . . . . . . . . . . . . . . . . . . . . . . . . . . . 55
3.5.1. Experimental Techniques . . . . . . . . . . . . . . . . . . . . . . 55
3.5.2. Four Point Measurements and the Electric Field Effect . . . . . 56
3.5.3. Non Local Spin Valve Measurements . . . . . . . . . . . . . . . 57
3.5.4. Hanle Measurements . . . . . . . . . . . . . . . . . . . . . . . . 59
3.5.5. Equipment . . . . . . . . . . . . . . . . . . . . . . . . . . . . . 59

**4. On the Theory of Spin Dependent Tunneling 61**
4.1. Introduction . . . . . . . . . . . . . . . . . . . . . . . . . . . . . . . 61
4.2. Free Electron Tunneling . . . . . . . . . . . . . . . . . . . . . . . . . 63
4.3. Discussion . . . . . . . . . . . . . . . . . . . . . . . . . . . . . . . . 67
4.4. Conclusion . . . . . . . . . . . . . . . . . . . . . . . . . . . . . . . . 69

**5. Electrical Detection of Spin Precession in freely-suspended Graphene Spin Valves 71**
5.1. Introduction . . . . . . . . . . . . . . . . . . . . . . . . . . . . . . . 71
5.2. Spin Injection in Graphene . . . . . . . . . . . . . . . . . . . . . . . 71
5.3. Results and Discussion . . . . . . . . . . . . . . . . . . . . . . . . . 73
5.4. Conclusion . . . . . . . . . . . . . . . . . . . . . . . . . . . . . . . . 77

**6. Enhanced Spin Accumulation in Graphene Spin Valves 79**
6.1. Introduction . . . . . . . . . . . . . . . . . . . . . . . . . . . . . . . 79
6.2. Motivation . . . . . . . . . . . . . . . . . . . . . . . . . . . . . . . . 79
6.3. Amorphous Carbon as Interface Material . . . . . . . . . . . . . . . . 81
6.4. Experimental Results and Discussion . . . . . . . . . . . . . . . . . . 83
6.5. Conclusion . . . . . . . . . . . . . . . . . . . . . . . . . . . . . . . . 87

**7. Spin Thermocouple and Giant Spin Accumulation in Single Layer Graphene 89**
7.1. Introduction . . . 89
7.2. General Concept . . . 89
7.2.1. Context . . . 89
7.2.2. Graphene NLSV as Spin Thermocouple . . . 91
7.3. Experimental Results . . . 93
7.3.1. Device Characteristics . . . 93
7.3.2. Non Local IV Measurements . . . 94
7.3.3. Analysis of the Data . . . 98
7.3.4. Hot Carriers . . . 101
7.4. Conclusion . . . 103

**8. Conclusions 105**

**9. Acknowledgements 109**

**A. List of Publications 113**

**B. Supplementary Material to Chapter 7 115**
B.1. Numerical Simulation of the Temperature Profile . . . 115
B.2. Non Local and Thermoelectric Voltage . . . 117
B.3. Temperature obtained via Mott Relation . . . 118
B.4. Spin Dependent Seebeck Coefficients . . . 119

**C. Recipes for the sample fabrication 121**

**D. List of Abbreviations 125**

**Bibliography 125**

# 1. Introduction

Solid state physics and electronics are historically closely related. One could say that advances in solid state physics are a requirement for new developments in electronics. The invention of the transistor in 1947 is a prime example for that. Without the development of the band structure theory of solids, the experimental realization of the transistor would not have been possible. In retrospect, it is safe to say that few inventions of the 20th century have influenced our society so thoroughly to the present day.

Throughout the last 50 years, progress in the semiconductor and information storage industry was mainly due to a miniaturization of the transistors and integrated circuits. However, nowadays the industry is facing a paradigm shift, as typical dimensions of the electronical components are approaching a limit where quantum mechanical effects start to play an important role.

Therefore, alternatives to traditional electronics will become necessary in the future. Again, an understanding of elementary physics is a prerequisite for the engineering of novel nanotechnological devices based on completely new concepts.

Two fields that could provide such alternatives are spintronics and graphene physics. Both are among the currently most active areas of solid state physics, which is expressed in the fact that in recent years, two nobel prizes have been awarded for discoveries in these fields. The numbers of publications concerning graphene is still exponentially increasing year after year, and also spintronics has seen a number of significant advances recently, which include effects such as the spin Hall effect or spin torque physics.

The aim of this thesis is to investigate spin and heat currents in graphene. Besides graphene and spintronics, it is also related to spin caloritronics, which is another area enjoying rapid growth.

While the search for new applications and technologies is important from a practical point of view, we hope to demonstrate that the work presented in this thesis constitutes a piece of research, which is justified in itself by shedding light on new and exciting physics.

### Spintronics

In contrast to electronics, which relies solely on the charge of the electron, the idea of spintronics is to also use its spin in order to build micro- and nanotechnological devices with enhanced perfomance or novel functionalities.

Between 1971 and 1973, Tedrow and Meservey demonstrated that spin polarized electrons can exist outside of a ferromagnet [1, 2]. They used the Zeeman splitting of a superconductor to detect the spin polarization of a tunneling current inside of a Ferromagnet/Insulator/Superconductor (FM/I/SC) junction. Two years later, Jullière demonstrated that it was possible to use the exchange splitting of a second Ferromagnet instead of the Zeeman splitted superconductor, leading to the discovery of tunneling magnetoresistance (TMR) in FM/I/FM junctions [3]. Finally, over a decade later giant magneto resistance (GMR) was discovered in multi layered structures by Grünberg and Fert in two indepedent pieces of research [4, 5], winning them the Nobel prize in physics in 2007.

Although closely related to TMR and GMR, the work presented in this thesis belongs to a second branch of research motivated by the Tedrow/Meservey experiments. Building on their pioneering work, Aronov and Pikus suggested in 1976 that it would be possible to create non equilibrium spin polarization in a non magnetic material by passing a current through a ferromagnet [6, 7]. Experimental evidence was first given by Johnson and Silsbee from 1985 on [8, 9, 10]. They experimentally demonstrated electrical spin injection using a non local geometry, which separates spin and charge currents.

In 2001, Jedema *et al.* demonstrated electrical spin injection at room temperature using a similar structure as Johnson and Silsbee [11]. Due to advances in nanolithography methods, they had been able to reduce the size of their samples three orders of magnitude, increasing the non local voltages for the same amount.

Following these experiments, a variety of spin related effects in solid state media has been discovered, such as the inverse spin Hall effect[12] or spin transfer torque[13, 14]. For a more detailed explanation of these fascinating phenomena, the reader is referred to ref. [15], which is a comprehensive review of spintronics and its applications, while the evolution of local techniques is described in detail in ref. [16].

**Graphene**

Graphene, a two dimensional system of carbon in a honeycomb lattice is one of the most promising materials for electronics, but also spintronics. The theoretical properties of graphene have been studied as early as 1947 [17]. However, until the seminal paper of Novoselov, Geim *et al.* in 2004 [18], experimental studies of graphene were scarce. Not only did they demonstrate that it was possible to obtain graphene by peeling off single layers from a bulk of graphite by simple Scotch tape, they did also show that those layers are visible in an optical microscope due to an interference effect with the substrate, which made the study of graphene straightforward and widely available. This contributed to the exponential increase in graphene related research activity. Geim and Novoselov were awarded with the Nobel prize in physics in 2010.

Graphene offers unique and exciting physics to study. Moreover, it exhibits superior material properties, such as electric and thermal conductivity, mechanical flexibility or

ultra-high electronic mobilities. These properties make it a potential building block of the next disruptive technology [19], and initially many efforts were put into realizing graphene based transistors, in order to replace Silicon as the abundant electronic material. However, the likelihood of this seem increasingly small. Instead, new applications for graphene are sought for, which exploit its excellent material qualities.

The spin injection measurements presented throughout this thesis underline the potential of graphene in the context of spintronics, but also the complexity and broad physical effects that can be studied with this material, such as novel ways to control the electronic spin. Charge transport studies have benefited considerably of the fabrication of freely suspended devices, which allow for the investigation of graphene undisturbed by the substrate. Similar benefits can be expected in the context of spin transport studies, and in order to gain insight into the relationship between mobility and spin relaxation lenght, we have developed a method to fabricate freely suspended graphene spin valves, which we present in chapter 5. Moreover, we have demonstrated that the spin injection efficiency in graphene can be greatly enhanced by the deposition of a thin layer of amorphous carbon at the FM/graphene interface. These results are presented in chapter 6.

For further reading, ref. [20] discusses the electronic properties of graphene, ref. [21] the experimental ones, while the search for applications is summarized in ref. [19]. A review of spintronics in graphene is ref. [22].

### Spin Caloritronics

The field of spin caloritronics is relatively new. It came to attention due to a renewed interest in classical thermoelectrical effects known and studied since the 1800s, such as the Seebeck effect. In spin caloritronics, spin dependent versions of these classical effects are investigated on a mesoscopic scale.

Massive interest in the interplay between heat and spin currents has been triggered by the observation of the so-called spin Seebeck effect in 2008 [23]. This motivated the exploration of similar and related effects, such as the spin-dependent Seebeck effect, or the magneto Seebeck effect, the spin dependent Peltier effect [24]. Our own group has contributed to the topic with the experimental realization of a magnon-drag thermopile [25].

It is intriguing to explore the possibility of spin caloritronics in graphene. Considerable efforts have been taken in order to investigate the thermal properties of graphene, such as thermal conductivity [26] or its Seebeck coefficient [27]. As we demonstrate in chapter 7, the interplay of spin and heat currents in graphene allows for the realization of novel devices which we descibe as a spin thermocouple.

An excellent review of spin caloritronics is ref. [24], while the thermal properties of graphene are summarized in ref. [28].

### Contents of this thesis

The structure of this thesis is as follows:

- In chapter 2, we introduce basic theoretical concepts required for the interpretation of the experiments presented throughout this thesis. We focus on spin injection into non magnetic materials, discussing topics such as spin accumulation or the phenomenological model of spin injection. These concepts can easily be applied to spin injection into graphene. We conclude the chapter with a discussion of spin relaxation in graphene.

- In chapter 3, we describe the fabrication process of our devices, including a detailed description of the mechanical exfoliation of graphene as well as the characterization of crosslinked PMMA. We further discuss the different processes used for the device fabrication and explain basic measurement configurations as well as the equipment used during fabrication and measurements.

- Chapter 4 consists of a theoretical study of the spin polarization of electrons tunneling between ferro- and non magnetic material. The model allows us to study electronic tunneling more thoroughly, and to introduce basic concepts regarding spin dependent electronic transport.

- In chapter 5, we demonstrate succesful electrical spin injection into freely suspended graphene spin valves. These devices are fabricated using an acid free method developed in the context of this thesis, where we use crosslinked PMMA in order to suspend the graphene flake. Moreover, we demonstrate Hanle spin precession in our devices, yielding a spin relaxation length of approx. $1.8\,\mu$m. These results have been published in *Small*.

- In chapter 6 we discuss how we obtain enhanced non local voltages in our spin valve devices by an additional step during the fabrication process. The results of this chapter have been published in *Applied Physics Letters*.

- In chapter 7 we present measurements of giant spin accumulation in graphene. This is due to the enhanced signal in the non local spin valves and a further enhancement due to a second order contribution of the bias current. We show that at the Dirac point of graphene, the device can be seen as a spin thermocouple, where the two arms are formed by the spin channels. These results are currently in preparation for submission to a scientific journal.

- The main results of this thesis are summarized in chapter 8.

- Supplementary material regarding chapter 7, recipes for the device fabrication, as well as a list of publications and a list of abbreviations are given in the appendix.

# 2. Theoretical Background

## 2.1. Introduction

The experimental work presented in this thesis is related to several areas of currently active research in solid state physics, such as spintronics, spin caloritronics and graphene. Therefore, this theorectical chapter has to cover a wide range of different topics. The aim of this chapter is to introduce basic principles of each topic, providing a basis for the understanding of the work presented in the later sections of this thesis.

The layout of this chapter is as follows:

We start with a brief introduction to the classic theory of electronic and thermal conduction in metals, including a description of the Seebeck effect (section 2.2).

Then, we discuss the theory of magnetism in solid state physics, especially the Stoner Wolfarth model of ferromagnetism, the two-current model of Mott and magnetoresistance (section 2.3). Then, we introduce the concept of spin accumulation in non magnetic materials (section 2.4). We also present a detailed description of the standard model of spin injection into non magnetic materials (section 2.5), and introduce Hanle spin precession (section 2.6).

We then give a basic introduction to the newly emerging field of spin caloritronics (section 2.7). Here, we make the attempt to show the formal similarity between the different types of transport, be it charge, heat or spin current.

Finally, we discuss basic properties of graphene such as the electronic band structure and the electric field effect (section 2.8). An introduction to spin relaxation in graphene concludes the chapter (section 2.9).

## 2.2. Electrical and Thermal Conduction in Metals

Electrical and thermal transport in metals can be understood within a semi-classical model similar to the kinetic gas theory, the Drude model [29, 30, 31]. According to this model, conduction is mediated by scattering events between the valence electrons and the ions of the metals. This defines the mean free path of the electrons $\lambda_\mathrm{e}$ as well as the mean free time $\tau_\mathrm{e}$ between scattering events.

The DC conductivity $\sigma$ of a metal is related to the electric field $\vec{E}$ by Ohm´s rule [32] $\vec{j}_c = \sigma\vec{E}$, where $\vec{j}_c$ the charge current density. The index $c$ stands for charge.

Using the electrical potential $V$ and $\vec{E} = -\nabla V$, it can be written as

$$\vec{j}_c = -\sigma \nabla V \tag{2.1}$$

Hence, a charge current within a metal is caused by a gradient in an electrical potential.

In a similar way, a heat current within a metal is caused by a gradient in temperature, as expressed by Fourier´s rule

$$\vec{j}_h = -\kappa \nabla T \tag{2.2}$$

Here, the index $h$ stands for heat, while $\kappa$ is the thermal conductivity and $\nabla T$ a gradient in temperature. The similarity between the two types of conduction is illustrated in Fig. 2.1 (a) and (b), while we introduce the spin current, shown in (c), in section 2.4. All types of conduction are examples of diffusive transport.

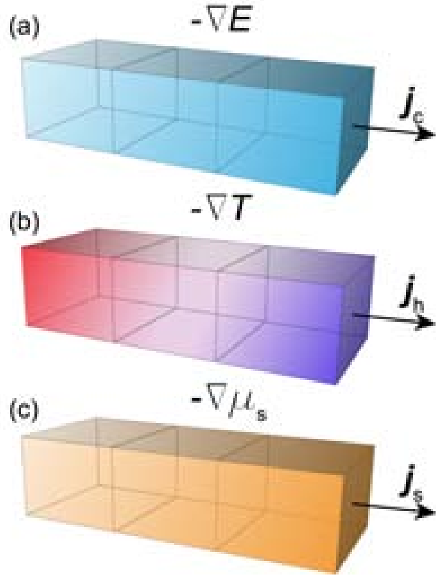


Figure 2.1.: Conduction of (a) charge, (b) heat and (c) spin currents in metals

As heat and charge currents in metals are both dominated by the electrons, an interplay between the two types of conduction exists. It manifests itself in thermoelectric effects such as the Seebeck effect, which is highly important for the understanding of the measurements presented in chapter 7. If a temperature gradient is applied to a metal bar, as shown in Fig. 2.1 (b), electrons travel from the hot to the cold end of the rod. The resulting thermoelectric field builds up until it compensates for the thermal gradient. This is the Seebeck effect, which can be written as

$$\vec{E} = -S \nabla T \tag{2.3}$$

Here, $S$ is the Seebeck coefficient of the material. It can be expressed as [33]

$$S = -\frac{\pi^2 k_{\mathrm{B}}^2 T}{3|e|} \frac{1}{\sigma} \frac{\partial \sigma}{\partial E}|_{E=E_{\mathrm{F}}} \tag{2.4}$$

Equation 2.4 is the so-called Mott relation or Mott formula of the Seebeck coefficient.

For systems such as graphene, where the Fermi energy $E_{\mathrm{F}}$ can be tuned by applying a gate voltage $V_g$ over a capacitance $C_g$, $S$ can be written as [27]

$$S = -\frac{\pi^2 k_{\mathrm{B}}^2 T}{3|e|} \frac{1}{\sigma} \frac{\partial \sigma}{\partial V_g} \frac{\partial V_g}{\partial E}|_{E=E_{\mathrm{F}}} \tag{2.5}$$

where

$$\frac{\partial V_g}{\partial E_\mathrm{F}} = \sqrt{\frac{|e|}{C_g \pi} \frac{2}{\hbar v_\mathrm{F}} \sqrt{|\Delta V_g|}} \tag{2.6}$$

with the Fermi velocity $v_\mathrm{F}$ and $\Delta V_g = V_g - V_\mathrm{D}$. $V_\mathrm{D}$ is the Dirac point of graphene. A detailed description of graphene is given in section 2.8.

The interplay between charge, heat and also spin currents has recently received renewed attention by the solid state physics community. The field is labeled Spin Caloritronics [24], which is treated in section 2.7.

## 2.3. Magnetism in Solid State Physics and Electronics

### 2.3.1. Stoner Wolfarth Model

Many electronical properties of solid state materials can be explainded using a band structure model [29]. These bands can be derived from the atomic configuration of the crystal lattice of the material.

Similarly, also ferromagnetism can be understood using a band structure model, the Stoner Wolfarth model of ferromagnetism [34]. Within this model, the $d$ band of the $3d$ transition metals Ni, Co and Fe is split into two spin subbands.

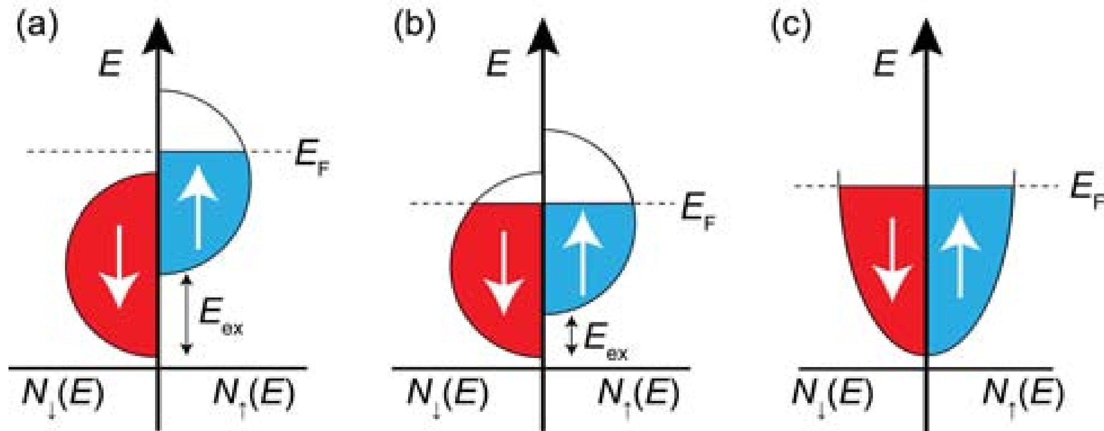


Figure 2.2.: (a) Ideal Stoner FM with one filled subband (b) Stoner FM with two partially filled subbands (c) Nonmagnetic material with two equally filled subbands

The densities of states (DOS) of an ideal Stoner Ferromagnet (FM) are shown in Fig. 2.2 (a). We label the majority spins as spin down and the minority as spin up, without loss of generality. The bottom of their bands are shifted in respect to each

other by $E_{\text{ex}}$. The spin down band is completely filled, as it lies below the Fermi energy. This implies that the spin polarization $P$ of such a material is 100 %.

Ferromagnetic alloys have been developed, which act as ideal Stoner FMs, e.g. the oxide $La_{0.6}Sr_{0.33}MnO_3$ (LSMO) [35] or Heusler alloys such as NiMnSb [36]. However, in most ferromagnetic materials, the spin bandstructure consists of two partially filled subbands, as shown in Fig. 2.2 (b).

Finally, a sketch of a nonmagnetic material (NM) is shown in Fig. 2.2 (c). Here, the electronic properties are dominated by the $s$ electrons, while there is no imbalance between the two spin subbands and the spin polarization is zero.

Considering the electrical currents in such materials, we make use of the two-current model of Mott [37, 38]: We assume that the propability of spin-flips during scattering events is negligible. This means that electrons of different types of spin do not mix during scattering processes, i.e. during electrical or thermal conduction. The conductivity $\sigma$ of a given material can therefore be expressed as a sum of two independent channels for spin up and spin down, $\sigma = \sigma_\uparrow + \sigma_\downarrow$.

The electrical current in an ideal Stoner FM is completely spin polarized, as only spin up particles can participate in the conduction process. If the two subbands are partially filled, as shown in Fig. 2.2 (b), both subbands contribute to electrical conduction.

### 2.3.2. Magnetoresistance

A change in the electrical resistance of a material by applying a magnetic field is referred to as magnetoresistance (MR). There are different kinds of MR, but for the spin valve measurements, introduced in section 2.5, anisotropic magnetoresistance is especially important, as it might occur as spurious effect. We further introduce tunnel magnetoresistance, as an example of a (local) spin valve structure.

**Anisotropic Magnetoresistance (AMR)** In 1857, Lord Kelvin discovered that the electrical resitivity of a ferromagnetic strip changes depending on the angle between the magnetization and the direction of the current [39]. AMR is a band structure effect, and the difference between perpendicular and parallel resistivities $\rho_\parallel$ and $\rho_\perp$ can be derived as

$$\rho_\parallel - \rho_\perp = \Delta\rho\cos^2(\theta) \tag{2.7}$$

where $\theta$ is the angle between current and magnetization of the FM.

**Tunneling Magnetoresistance (TMR)** In contrast to AMR, which can be observed in a single FM, TMR occurs in FM/I/FM junctions, where I stands for an insulator. Applying a bias voltage between the two ferromagnets leads to a tunneling current via the insulating layer which depends on the relative orientation of the

magnetizations of the FMs. TMR is historically defined as [3]

$$TMR := \frac{R_{\uparrow\downarrow} - R \uparrow\uparrow}{R_{\uparrow\uparrow}} \tag{2.8}$$

where $R_{\uparrow\downarrow}$ stands for the anti parallel (AP) alignment of the ferromagnet and $R_{\uparrow\uparrow}$ for the parallel (P) alignment.

A graphical representation of TMR is shown in Fig. 2.3. As indicated by the arrows, tunneling takes place only between equal types of spin. For parallel (P) alignment, there is the same amount of spin up and spin down states available at the Fermi energy (Fig. 2.3 (a)).

In case of anti parallel (AP) alignment of the FMs, as depicted in Fig. 2.3 the majority spins tunneling out of FM1 have few states available at the Fermi energy in FM2 to tunnel to. For the minority spin, there are many states available to tunnel to, but few electrons in FM1 at the Fermi energy. Therefore, the resistance of the junction is higher in the anti parallel case.

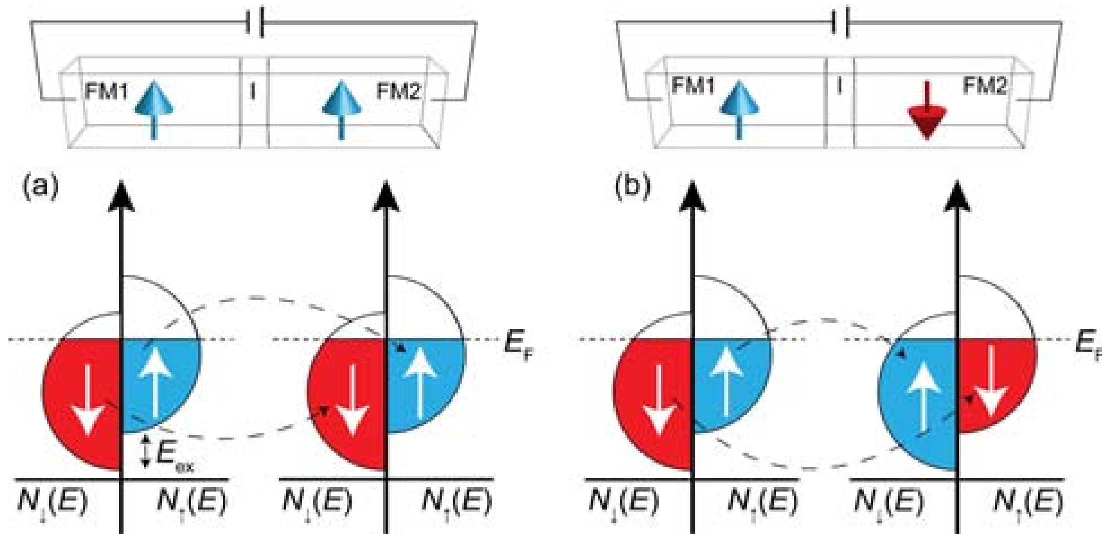


Figure 2.3.: Graphical representation of TMR

TMR based devices are examples of so-called spin valve structures. A spin valve is a device consisting of at least two ferromagnetic layers, whose resistance changes by changing the relative magnetization between the layers. Moreover, this orientation is preserved even if the power supply is switched off.

## 2.4. Spin Accumulation

In order to investigate magnetic phenomena such as GMR and TMR, there are many advantages in using non local devices, where spin and charge current are separated.

A detailed theoretical description of such systems is given in section 2.5. Here, we introduce the main concepts of electrical spin injection into non magnetic materials. Especially, we demonstrate that an electrical current via a FM/NM interface is a source of spin current [8].

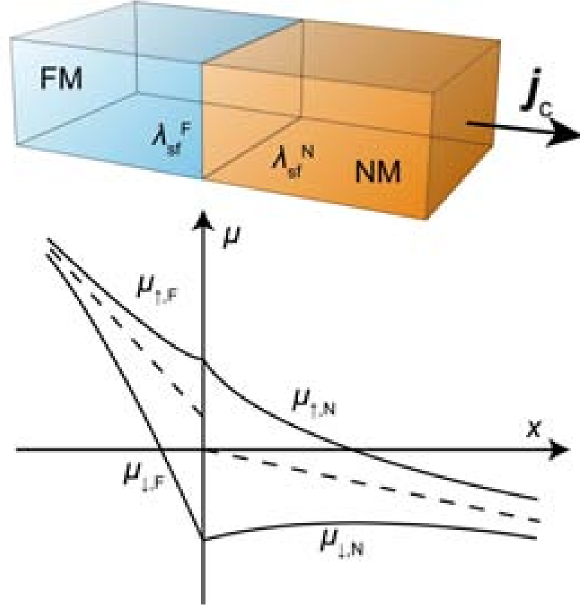


Figure 2.4.: Electrochemical potentials near an FM/NM interface

There is an important consequence of the Stoner model of FM in combination with the two-current model of Mott. When an electrical current flows from a FM into an NM, the distribution of the current over spin up and spin down has to change [40]. This follows from the fact that in the NM the two spin subbands are equal, thus also the number $n_{\uparrow,\downarrow}$ of spins of a given state as well as the conductivities $\sigma_{\uparrow,\downarrow}$ for spin up and spin down electrons. In contrast, there is an imbalance in the FM, meaning that $n_\uparrow \neq n_\downarrow$ and $\sigma_\uparrow \neq \sigma_\downarrow$. As the total number of electrons is conserved, this results in a redistribution of spin up and spin down electrons.

We consider a system as schematically shown in Fig. 2.4. An electrical current $\vec{j}$ flows via a rod consisting of an NM and an FM. We choose the lateral dimensions of the system to be small, so that we can treat it as one-dimensional. The direction of the current is the $x$ axis, with the FM/NM interface at $x = 0$. The charge current density is given by $\vec{j}_c = \vec{j}_\uparrow + \vec{j}_\downarrow$ and the spin current density by $\vec{j}_s = \vec{j}_\uparrow - \vec{j}_\downarrow$. In the same way, the electrochemical potentials are given by $\mu = \mu_\uparrow + \mu_\downarrow$ and $\mu_s = \mu_\uparrow - \mu_\downarrow$.

In the following, we use the index $N$ to indicate parameters of the NM, and $F$ for those of the FM, as well as $\uparrow, \downarrow$ for spin up and down.

In this system, the gradient of the electrochemical potential in the direction of the

current is given by [40] $\partial_x \mu_{\uparrow,\downarrow} = -(e/\sigma_{\uparrow,\downarrow}) j_{\uparrow,\downarrow}$. It follows that in the NM

$$\vec{j}_s = -\frac{\sigma_N}{e} \nabla \mu_s \tag{2.9}$$

where we wrote $\partial_x$ as $\nabla$ in order to stress the formal analogy to Eqs. 2.1 and 2.2 for charge and heat currents. The three types of transport are shown in Fig. 2.1. Independently of the nature of the current, all are linear responses to a gradient in the a potential. Like charge and heat, spin transport is of diffusive nature and in steady state the diffusion equation for the potential difference is given by [40]

$$\mu_s = \tau_{\mathrm{sf}} D \partial_x^2 \mu_s \tag{2.10}$$

where $D$ is the the diffusion constant of the material and $\tau_{\mathrm{sf}}$ the spin relaxation time: If the source of spins is switched off at a given time, then the excess of one type of spins would decay exponetially with $\tau_{\mathrm{sf}}$. It becomes clear from Eq. 2.10 that the spin splitting of the electrochemical potential also decays exponentially with $x$, i.e. away from the FM/NM interface:

$$\mu_s \propto \mu(x=0) e^{-\lambda_{\mathrm{sf}}/x} \tag{2.11}$$

The splitting is the largest at the interface, while far away, $\mu^{\uparrow} = \mu^{\downarrow}$ has to be valid for both materials. This is a so-called spin accumulation close to the interface. The characteristic length scale over which $\mu_s$ decays is the spin relaxation lenght $\lambda_{\mathrm{sf}}$ and from Eq. 2.10 follows that

$$\lambda_{\mathrm{sf}} = \sqrt{\tau_{\mathrm{sf}} D} \tag{2.12}$$

The electrochemical potentials $\mu^{\uparrow}$ and $\mu^{\downarrow}$ within both materials are schematically shown in Fig. 2.4. Note that for most FMs, $\lambda_{\mathrm{sf}}$ is of the order of a few nm, while in NM it can be hundreds of nm or even $\mu$m.

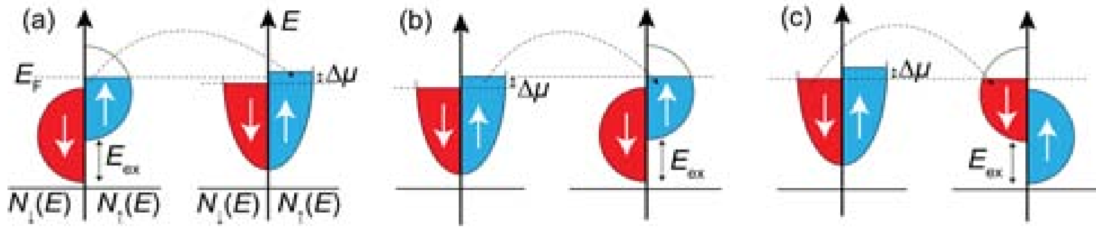


Figure 2.5.: Spin injection and detection between idealized Stoner FM and NM (a) Injection (b) Detection, parallel (c) Detection, anti parallel

Using the bandstructure model introduced in section 2.3.1, we can illustrate electrical spin injection as shown in Fig. 2.5 (a) [9, 10]. We assume the FM to act as an ideal Stoner FM, with only one spin subband partially filled. Spin up electrons are

injected into the NM, creating an imbalance between the chemical potentials of spin up and spin down, which is the spin accumulation $\mu_s$.

In order to detect the spin accumulation, a second FM is required. In Fig. 2.5 (b) and (c), we show a NM on the left hand side, which exhibits a spin accumulation $\mu_s$. Electrons traveling from the NM into the FM are spin polarized. In Fig. 2.5 (b), the detector FM is polarized in the same way as the current, while in (c), the polarization of the detector is opposite. These configuration are referred to as parallel (P) and anti parallel (AP). In the parallel case, the Fermi energy of the spin up electrons in the FM aligns with the Fermi level of the spin up electrons in NM. In the antiparallel case, the spin down Fermi levels align. Therefore, a voltage $V$ can be detected between NM and FM, which is proportional to $\mu_s/2e$.

## 2.5. Non Local Spin Injection and Detection

### 2.5.1. Motivation

We have shown in the previous sections that a current flowing via a FM/NM interface creates a spin accumulation close to the interface. This spin accumulation results in a voltage between FM and NM, which is related to the change in electrochemical potential. When trying to measure such spin accumulation however, it is beneficial to use a non local detection scheme, as otherwise the effect of the magnetoresistance is masked by the conventional electrical resistance of such a device, which is orders of magnitude bigger. Also, the use of a non local setup allows for the elimination of spurius effects such as AMR.

In the following we give a detailed derivation of the non local voltages as a function of the system parameters. Especially, we show that there are different regimes depending on the contact resistance between NM and FM. In actual devices these regimes are given by the type of contact, being either transparent, low resistance contacts, or tunnel, high resistance contacts. The derivation is based closely on [41] and [42].

### 2.5.2. System

In order to obtain a general description of non local spin injection into nonmagnetic materials, we consider the system shown in Fig. 2.6. It consists of two ferromagnets on top of a nonmagnetic material, forming two FM/NM junctions. The FMs have the same width $w_F$ and height $d_F$ and the nonmagnetic material $w_N$ and $d_N$. The center-to-center distance of the FMs is labeled $L$. A bias current is applied to the left hand FM/NM junction, so that a charge current flows only in the left hand part of the nonmagnetic material, while a voltage $V_{\mathrm{NL}}$ is detected non locally between the NM and the second FM. This voltage is due to the spin accumulation close to the FM/NM interface. The model system corresponds well to the experimental situation.

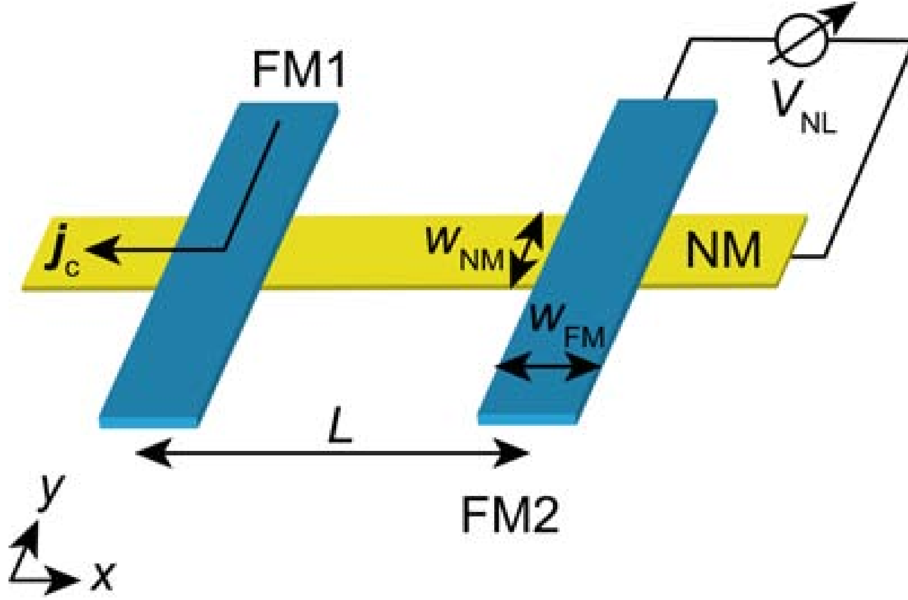


Figure 2.6.: Schematic diagram of a non local spin valve

As we have shown in section 2.2, the conductivity of a given material can be calculated by considering the current flowing via a cross section of the material. Here, the situation is slightly more complicated, as there are two cross sections to consider, as shown in Fig. 2.7: The first one, labeled $A_J$, is the interface between the left ferromagnet and the nonmagnetic material, where the charge current passes through (thus the index $J$). This is the source of the spin current we are interested in. The second one is the cross section of the non magnetic material $A_N$, where named spin current flows. Therefore

$$A_J = w_F \times w_N, \quad A_N = w_N \times d_N \tag{2.13}$$

In the following derivation we make repeated use of the continuity equations for spin and charge currents passing through these cross sections.

It is straightforward to obtain a model for spin transport in the system when using the two-current model of Mott. In the ferromagnet, the material parameters are spin dependent:

$$n \mapsto n_\uparrow, n_\downarrow, \quad \mu \mapsto \mu_\uparrow, \mu_\downarrow, \quad \sigma \mapsto \sigma_\uparrow, \sigma_\downarrow, \quad D \mapsto D_\uparrow, D_\downarrow \tag{2.14}$$

Here, $n$ is the density of carriers of a given spin type, $\mu$ the electrochemical potential, $\sigma$ conductivity and $D$ diffusion constant of the material. In nonmagnetic materials the parameters are spin independent. For instance for $\sigma$: $\sigma_{N,\uparrow} = \sigma_{N,\downarrow} = \frac{1}{2}\sigma_N$. It is also important to keep in mind that the material parameters are discontinous at the interface : $\sigma_N \neq \sigma_{F,\uparrow} \neq \sigma_{F,\downarrow}$.

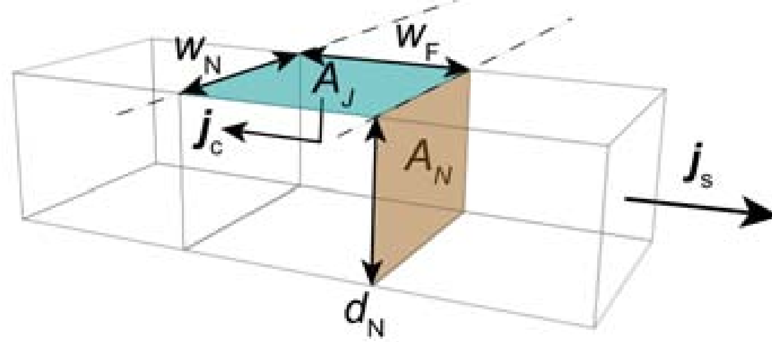


Figure 2.7.: Sketch of the current flow from Ferromagnet to non magnetic metal (via $A_J$) and through it (via $A_N$)

### 2.5.3. Derivation of the Diffusion Equation

In the following, we derive an expression for the non local voltage detected at the right side of our system. First, we write down the continuity equations for spin and charge, which have to be conserved in the process. These equations read:

$$\nabla\vec{j}_c = \nabla(\vec{j}_\uparrow + \vec{j}_\downarrow) = 0 \tag{2.15}$$

$$\nabla\vec{j}_s = \nabla(\vec{j}_\uparrow - \vec{j}_\downarrow) = -e\delta n_\uparrow/\tau_{\uparrow\downarrow} + e\delta n_\downarrow/\tau_{\downarrow\uparrow} \tag{2.16}$$

Equation 2.15 is the continuity equation for charge $\nabla\vec{j}_c + \dot{\rho}_c = 0$, where we already demanded a steady state situation: $\dot{\rho} = 0$. In equation 2.16, $\delta n_{\uparrow,\downarrow}$ is the deviation from equilibrium of carrier densities $n_{\uparrow,\downarrow}$, while $\tau_{\uparrow\downarrow}$ ($\tau_{\downarrow\uparrow}$) is the characteristic time for spin flips from state $\uparrow$ ($\downarrow$) to $\downarrow$ ($\uparrow$). Therefore, eq. 2.16 accounts for the change in carrier density $n_i$ due to spin flips. We demand detailed balancing [42] between these events, meaning that

$$\frac{n_\uparrow}{\tau_{\uparrow\downarrow}} = \frac{n_\downarrow}{\tau_{\downarrow\uparrow}} \tag{2.17}$$

The current densitity in the nonmagnetic material $\vec{j}_{\uparrow,\downarrow}$ can be written within the two current model as [41]

$$\vec{j}_{\uparrow,\downarrow} = -\sigma_{\uparrow,\downarrow}\nabla V - eD\nabla\delta n_{\uparrow,\downarrow} \tag{2.18}$$

Here, the first term is the spin dependent equivalent to eq. 2.1, while the second one accounts for diffusion of spins due to the deviation $\delta n_{\uparrow,\downarrow}$ from equilibrium of the spin

population. In a nonmagnetic material without external source of spin polarization, these populations are in equilibrium and eq. 2.18 becomes Ohm´s rule, eq. 2.1.
Next, we use the Einstein relation between $\sigma$ and $n$

$$\sigma_{\uparrow,\downarrow} = e^2 n_{\uparrow,\downarrow} D \tag{2.19}$$

and note that $\delta n_{\uparrow,\downarrow} = n_{\uparrow,\downarrow} \delta E_{\uparrow,\downarrow}$ [41]. It is therefore possible to use the energy $E$ instead of carrier density $n$ as variable. We further define the electrochemical potential for each spin sub band:

$$\mu_{\uparrow,\downarrow} = E_{\uparrow,\downarrow} + eV \tag{2.20}$$

where we use the bias voltage $V$. With these definitions, it is possible to write eq. 2.18 as

$$\vec{j}_{\uparrow,\downarrow} = -(\sigma_{\uparrow,\downarrow}/e)\nabla\mu_{\uparrow,\downarrow} \tag{2.21}$$

It follows for a spin current in nonmagnetic material

$$\boxed{\vec{j}_s = -\frac{\sigma_N}{e}\nabla\mu_s} \tag{2.22}$$

This is the same result as Eq. 2.9.

By using the continuity equations for charge and spin, Eq. 2.15 and 2.16, as well as detailed balancing, eq. 2.17, in eq. 2.21, we obtain the spin diffusion equations [40]

$$\nabla^2(\sigma_\uparrow\mu_\uparrow + \sigma_\downarrow\mu_\downarrow) = 0 \tag{2.23}$$

$$\nabla^2(\mu_\uparrow - \mu_\downarrow) = \lambda_{\text{sf}}^{-2}(\mu_\uparrow - \mu_\downarrow) \tag{2.24}$$

Equation 2.24 is equivalent to 2.10, as $\lambda_{\text{sf}} = \sqrt{D\tau_{\text{sf}}}$, where $\tau_{\text{sf}}^{-1} = \frac{1}{2}(\tau_{\uparrow\downarrow}^{-1} + \tau_{\downarrow\uparrow}^{-1})$ and $D^{-1} = (n_\uparrow D_\downarrow^{-1} + n_\downarrow D_\uparrow^{-1})/(n_\uparrow + n_\downarrow)$. Furthermore, here and in the following $\lambda_{\text{sf}} = \lambda_N$ and $\tau_{\text{sf}} = \tau_N$.

### 2.5.4. Interfacial Currents

In order to find solutions for $\mu_\uparrow$ and $\mu_\downarrow$ that satisfy eq. 2.23 and 2.24, one can write the interfacial currents (for the interface at $z = 0$) as

$$I_i^{\uparrow,\downarrow} = (G_i^{\uparrow,\downarrow}/e)(\mu_F^{\uparrow,\downarrow}|_{z=0} - \mu_N^{\uparrow,\downarrow}|_{z=0}) \quad \text{for } \ i = 1, 2 \tag{2.25}$$

where $G_i$ is the interface conductance, $G_i = G_i^\uparrow + G_i^\downarrow = R_i^{-1}$. This allows us to take into account different regimes of the interface: In the transparent regime, $G_i \to \infty$, the electrochemical potential are continous at the interface, while for the tunneling regime, $G_i$ is small. The interfacial charge and spin currents are given by $I_i^c = I_i^\uparrow + I_i^\downarrow$ and $I_i^s = I_i^\uparrow - I_i^\downarrow$.

In NM, the electrochemical potential only changes in the $x$ direction $(w_N, d_N \ll \lambda_N)$. Therefore, $\mu_N$ can be written as

$$\mu_N^{\uparrow,\downarrow} = \bar{\mu}_N \pm \delta\mu_N \tag{2.26}$$

Here, the first terms describes the effect of the bias and the second one the spin dependent shift of the electrochemical potential due to the ferromagnetic electrodes. The effect of the bias can be written as

$$\begin{aligned} \bar{\mu}_N &= \frac{eI}{\sigma_N}x, \qquad x < 0 \\ &= 0, \qquad\quad x > 0 \end{aligned} \tag{2.27}$$

which takes into account the layout of the system: The bias is applied only to the left hand side ferromagnet. The second term of eq. 2.26 can be written as

$$\delta\mu_N = a_1 e^{-\frac{|x|}{\lambda_{\mathrm{sf}}}} + a_2 e^{-\frac{|x-L|}{\lambda_{\mathrm{sf}}}} \tag{2.28}$$

for the spin injection at $x = 0$ by FM1 as well as a feedback term at $x = L$ due to FM2. The spin current $\vec{j}_s$ flows from left to right according to eq. 2.21. This means

$$\begin{aligned} \vec{j}_s &= -(\frac{\sigma_N}{e})\nabla\delta\mu_N \\ \Rightarrow \vec{j}_s &= (\frac{\sigma_N}{e\lambda_{\mathrm{sf}}})(\delta\mu_N) \end{aligned}$$

The continuity of the spin current at each junction yields

$$I_i^S = 2\frac{\sigma_N A_N}{e\lambda_N}a_i \tag{2.29}$$

Using similar consideration, an expression for the interfacial currents in the FMs can be derived as well.

### 2.5.5. Spin Dependent Voltage

In order to give an expression for the spin dependent, nonlocal voltage detected at FM2, we introduce the following abbreviations: The spin resistances of NM and the FM are given by $R_N = \rho_N\lambda_N/A_N$ respectively $R_F = \rho_F\lambda_F/A_F$. The interfacial current polarization is given by $P_J = \left|G_i^{\uparrow} - G_i^{\downarrow}\right|/G_i$. Finally, the resistivities are $\rho_N = \sigma_N^{-1}$ and $\rho_F = \sigma_F^{-1}$.

Using these definitions, the nonlocal voltage $V_2$ detected at FM2 divided by the injected current at FM1 can be written as [41]

$$V_2/I = \pm 2R_N e^{-L/\lambda_N} \frac{\prod_{i=1}^{2} \left( \frac{P_J \frac{R_i}{R_N}}{1-P_J^2} + \frac{p_F \frac{R_F}{R_N}}{1-p_F^2} \right)}{\prod_{i=1}^{2} \left( 1 + \frac{2\frac{R_i}{R_N}}{1-P_J^2} + \frac{2\frac{R_F}{R_N}}{1-p_F^2} \right) - e^{-2l/\lambda_N}} \tag{2.30}$$

The + and - signs correspond to parallel and antiparallel alignment of the magnetizations of FM1 and FM2. Experimentally, the detected voltage change due to the spin accumulation is

$$\Delta V_{\text{NL}} = 2|V_2| = V_2^{\text{P}} - V_2^{\text{AP}} \tag{2.31}$$

or in terms of the transresistance $\Delta R_{\text{NL}} = \Delta V_{\text{NL}}/I$.
The spin accumulation therefore depends on the ratios $R_F/R_N$ and $R_i/R_N$, where the $R_i$ are the contact resistances of the interfaces. $R_F/R_N$ is known as the resistance mismatch.
It is possible to classify a system depending on the resistance mismatch, which is determined by the type of contact

1. **Transparent contacts,** $R_1, R_2 \ll R_F$
   In this case only one term in the products of eq. 2.30 contributes, $p_F(R_F/R_N)/(1-p_F^2)$. Therefore, we can write the spin dependent signal $\Delta R_{\text{NL}}$ as

$$\Delta R_{\text{NL}} = \frac{4p_F^2}{(1-p_F^2)^2} R_N \left(\frac{R_F}{R_N}\right)^2 \frac{e^{-L/\lambda_N}}{1-e^{-2L/\lambda_N}} \tag{2.32}$$

2. **Tunneling contacts,** $R_1, R_2 \gg R_N$ Here, eq. 2.30 becomes

$$\Delta R_{\text{NL}} = P_J^2 R_N e^{-L/\lambda_N} \tag{2.33}$$

   Using the definition of $R_N$ and $\rho_N$, we can write this as

$$\Delta R_{\text{NL}} = \frac{P_J^2 \lambda_N}{\sigma_N A_N} e^{-L/\lambda_N} \tag{2.34}$$

It can be seen from eq. 2.32 and 2.34 that in case of transparent contacts, $\Delta R_{\text{NL}}$ scales with $\sigma_N$ while for tunneling contacts, it scales with $1/\sigma_N$. It also becomes apparent that in case of transparent contacts, $\Delta R_{\text{NL}}$ is proportional to $(R_F/R_N)^2$, while for tunneling contacts, the resistance mismatch is removed. Since $(R_F/R_N)$ is typically small, e.g. 0.01 in [11], the maximum spin signal can be achieved by using tunneling barriers as interfaces between NM and FM.

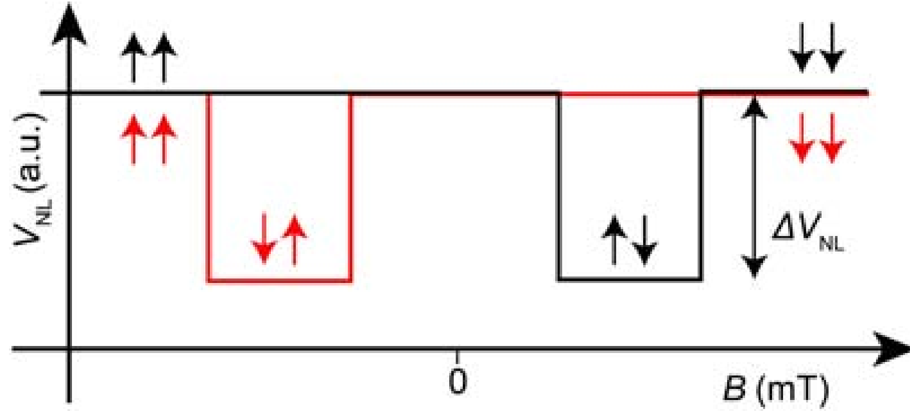


Figure 2.8.: Schematic representation of a non local spin valve measurement

In Fig. 2.8, we show a schematical representation of a non local spin valve measurement. At first we consider the black trace in Fig. 2.8: Starting at high negative magnetic fields both FMs point up (↑↑), in direction of the field. This alignment does not change for negative magnetic fields. After crossing zero, the magnetic field points into the direction opposite of the magnetizations of the FMs. The ferromagnetic electrode with the lower coercive field switches first, creating an anti parallel alignment of the FMs (↑↓). The value of the non local voltage $V_{\mathrm{NL}}$ switches as well. For ideal devices, the values of $V_{\mathrm{NL}}$ for P and AP alignment are symmetric around zero and the magnitude $\Delta V_{\mathrm{NL}}$ is given by eq. 2.31. Further increasing the external field leads to the switching of the second FM, creating P alignment again, but opposite in respect to the start of the measurement (↓↓).

Sweeping the field back in the opposite direction, a measurement of $V_{\mathrm{NL}}$ results in a curve such as the red one in Fig. 2.8, which exhibits the same physics for opposite magnetic fields, due to the hysteresis of the FMs.

## 2.6. Hanle Spin Precession

In section 2.5, we consider a system where the external magnetic field lies in the plane of the ferromagnetic electrodes of the spin valve devices. The non local voltage we detect in these systems depends on the relative alignments of the magnetizations of the FMs. But what happens to this voltage when the magnetic field is tilted out of plane, perpendicular to the magnetization of the ferromagnets, as shown in Fig. 2.9 (a)?

In the following, we show that this results in a precession of the injected spins around the external field. This is the Hanle effect, which originally described a magnetic resonance phenomenom in gases [43].

We consider a system with tunneling contacts, meaning that Eq. 2.34 is valid. In

combination with the Einstein relation, Eq. 2.19, we can write the voltage $V_2$ detected at FM2 as

$$\begin{aligned} V_2 &= \frac{1}{2} I \frac{P^2 \lambda_N}{\sigma_N A_N} e^{(-L/\lambda_N)} \\ &= \frac{1}{2} I \frac{P^2 \lambda_N}{e^2 NDA} e^{(-L/\lambda_N)} \end{aligned} \tag{2.35}$$

where $\lambda_N = \lambda_{\text{sf}}$ of the non magnetic material.

Now, the perpendicular field induces a coherent precession of the spins injected by FM1 with the Larmor frequency, which is determined by the external magnetic field:

$$\Omega = \gamma B_\perp = \frac{g\mu_\text{B}}{\hbar} B_\perp \tag{2.36}$$

Here, $g$ is the electronic g-factor, $\mu_\text{B}$ is the Bohr magneton and $\hbar$ is the reduced Planck´s constant. At FM2, only the component parallel to the magnetization results in a measurable voltage, i.e. the projection of the magnetization of the spins to the axis of FM2. The detected voltage $V_2$ is therefore proportional to $\cos(\Omega t)$.

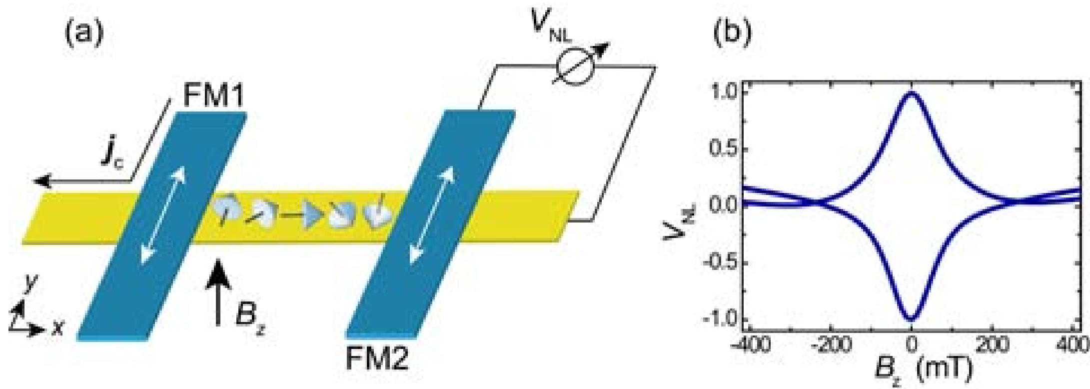


Figure 2.9.: Hanle spin precession (a) NLSV in a perpendicular magnetic field. The magnetization of the FMs can be P or AP, as indicated by the white arrows. Spins injected into the NM precess around the external field (b) Normalized non local voltage as a function of the perpendicular field as given by Eq. 2.39

Furthermore, the diffusive nature of the electronic conduction has an effect on the detected voltage as well. There are many possible paths with different lengths for the diffusion of the electrons, which leads to a distribution in diffusion times. This corresponds to a distribution in precession angles $\Omega t$ at FM2 given by [44]

$$f(t) = \frac{1}{\sqrt{4\pi Dt}} e^{(-L^2/4Dt)} \tag{2.37}$$

Additionally, we have to take into account the possibility of spin flips during the diffusion time $t$, which decays exponentially with $\tau_{\mathrm{sf}}$.

As these three contributions depend on $t$, one has to integrate over all possible times in order to get the total contribution of the precession to the spin dependent voltage [42]

$$V_2(B_\perp) = \pm I \frac{P^2}{e^2 N A_N} \int_0^\infty dt \quad \cos(\Omega t) f(t) e^{(-t/\tau_{\mathrm{sf}})} \tag{2.38}$$

Finally, for large perpendicular magnetic fields $B_\perp$, the magnetization of the ferromagnetic electrodes tilts out of the plane of the substrate with an angle $\theta$. This effect has to be included in the calculation of the spin dependent voltage [44]:

$$V_2(B_\perp, \theta) = V_2(B_\perp)\cos^2(\theta) + |V_2(B_\perp = 0)|\sin^2(\theta) \tag{2.39}$$

An example is shown in Fig. 2.9 (b). By fitting the experimental data to Eq. 2.39, it is possible to extract values for $\lambda_{\mathrm{sf}}, \tau_{\mathrm{sf}}, D$ and therefore also $P$.

## 2.7. Spin Caloritronics

In section 2.2, we introduce charge and heat current as well as the Seebeck effect as an example for the interplay between the two. Together with the Peltier effect [34], which is the opposite of the Seebeck effect, these phenomena can be combined in the thermoelectric equations.

The newly emerging field of Spin Caloritronics deals with spin dependent versions of these thermoelectric effects, such as the spin Seebeck effect (SSE) [23], or the spin-dependent Seebeck effect [45]. Our own group has contributed to the field with the experimental realization of a magnon-drag thermopile [25].

In this theoretical introduction, our aim is to demonstrate how charge, heat and also spin current are closely connected to each other. Further details regarding experimental advances can be found in chapter 7.

In respect to section 2.2, we introduce additional indices in Eq. 2.1 and 2.2: $\vec{j}_c^0 = -\sigma\nabla V$ and $\vec{j}_h^0 = -\kappa\nabla T$ Using these definitions, we can write the charge current density in a given material as

$$\vec{j}_c = \sigma(-\nabla V) + \sigma(-S\nabla T) \tag{2.40}$$

Here, the first term on the right hand side is given by Ohm´s rule ($\vec{j}_c^0$) and the second one by the Seebeck effect. Charge transport in a metal is due to a gradient in electrical potential or to a temperature gradient in the metal: $\vec{j}_c = \vec{j}_c^0 + \vec{j}_{Seebeck}$
The heat current density can be written as

$$\vec{j}_q = \Pi(-\sigma\nabla V) + (-\kappa\nabla T) \tag{2.41}$$

where Π is the Peltier coefficient of the material. The first term on the right hand side is given by the Peltier effect while the second one is Fourier´s rule. Similar to electrical conduction, heat transport in a metal is caused by gradient in temperature or electrical potential: $\vec{j}_q = \vec{j}_{Peltier} + \vec{j}_q^0$
It is therefore possible to write charge and heat current as components of a vector and the coefficients as elements of a matrix, which operates on the gradients:

$$\begin{pmatrix} \vec{j}_c \\ \vec{j}_q \end{pmatrix} = -\sigma \begin{pmatrix} 1 & S \\ \Pi & \kappa/\sigma \end{pmatrix} \begin{pmatrix} \nabla V \\ \nabla T \end{pmatrix} \tag{2.42}$$

The relation between spin and charge currents can be combined in the thermoelectric equations. By applying the two-current model introduced in section 2.3.1, the spin degree of freedom can be introduced into the theory in a similar way as in section 2.5.

Recall that the current densities for majority and minority spin are given by $\vec{j}^{\uparrow}$ and $\vec{j}^{\downarrow}$, so that $\vec{j}_c = \vec{j}^{\uparrow} + \vec{j}^{\downarrow}$ and $\vec{j}_s = \vec{j}^{\uparrow} - \vec{j}^{\downarrow}$. Also, as shown in section 2.5, $\vec{j}_s = -(\sigma/e)\nabla\mu_s$, where $\mu_s = \mu_{\uparrow} - \mu_{\downarrow}$. Finally, we define $\mu_c = (\mu_{\uparrow} + \mu_{\downarrow})/2$, where $\mu_{\uparrow,\downarrow} = E_{\uparrow,\downarrow} + eV$.

As pointed out in section 2.5, the simple equations for charge, heat and spin current are formally equal. In each case, the current is a (linear) response to the generalized forces, which are the gradients. It is possible to express this result in an elegant way by defining a current vector [46]

$$\vec{J} = (\vec{j}_c, \vec{j}_s, \vec{j}_q) \tag{2.43}$$

as well as a vector containing the generalized forces

$$\nabla X = (\nabla\mu_c/e, \nabla\mu_s/e, \nabla T) \tag{2.44}$$

Charge, spin and heat current can therefore be written as

$$\boxed{\vec{J} = \tilde{L}\nabla X} \tag{2.45}$$

Here, $\tilde{L}$ is a linear $3 \times 3$-matrix, whose elements can be obtained by demanding that Eq. 2.45 fulfills Ohm´s rule (Eq. 2.1), Fourier´s rule of heat conduction (Eq. 2.2), Eq. 2.9 for the spin current, as well as the Seebeck effect (Eq. 2.3) and its inverse, the Peltier effect. The latter two are connected via an Onsager relation, $\Pi = TS$. This allows for eliminating off diagonal elements of the matrix, while the simple equations for spin, heat and charge current determine the diagonal elements. One obtains [24]

$$\begin{pmatrix} \vec{j}_c \\ \vec{j}_s \\ \vec{j}_q \end{pmatrix} = -\sigma \begin{pmatrix} 1 & P & ST \\ P & 1 & P'ST \\ ST & P'ST & L_0T^2 \end{pmatrix} \begin{pmatrix} \nabla\mu_c/e \\ \nabla\mu_s/e \\ \nabla T/T \end{pmatrix} \tag{2.46}$$

where $P$ and $P'$ are the spin polarizations of the conductivity and the differential polarization at the Fermi energy:

$$P = \frac{\sigma_{\uparrow} - \sigma_{\downarrow}}{\sigma_{\uparrow} + \sigma_{\downarrow}}|_{E_{\mathrm{F}}}, \qquad P' = \frac{\partial_E\sigma_{\uparrow} - \partial_E\sigma_{\downarrow}}{\partial_E\sigma_{\uparrow} + \partial_E\sigma_{\downarrow}}|_{E_{\mathrm{F}}} \tag{2.47}$$

Equation 2.46 requires the Wiedemann-Franz-law to hold in order to be valid, so that $L_0 T = \kappa/\sigma$, where $L_0$ is the Lorentz number. In case of a nonmagnetic material, $P = P' = \nabla\mu_s = 0$ and Eq. 2.46 becomes Eq. 2.42. Finally, note that in the above discussion the charge current is understood as a sum of two independent spin channels, while this is not the case for the heat current. In principle the heat current has to be treated as a sum of spin up and down contributions as well, $\vec{j}_q = \vec{j}_q^{\uparrow} + \vec{j}_q^{\downarrow}$. Consequently a spin heat current $\vec{j}_{sq} = \vec{j}_q^{\uparrow} - \vec{j}_q^{\downarrow}$ can be expected. The absence of such a spin heat current can be justified by the assumption that there is no spin temperature gradient $T_s = T^{\uparrow} - T^{\downarrow}$ [47].

# 2.8. Graphene

## 2.8.1. Introduction

Throughout the following section, we introduce basic properties of graphene, such as the relativistic dispersion relation of the electrons and the electric field effect. Since the first succesful experimental observation of graphene in 2004 [18], these properties have been discussed multiple times. An excellent review can be found in [20]. However, since they are vital to the understanding of the work presented in the later chapters of this thesis, we shortly resume them here, before we discuss the topic of spin injection and detection in graphene in section 2.9.

## 2.8.2. Band Structure of Graphene in the Tight Binding Approach

Graphene is a two dimensional structure consisting of carbon. The atomic structure of carbon allows for several types of bonding, which results in many different atomic configurations. One example is amorphous carbon, another one diamond. Graphite is another example. Here, $sp^2$ hybridization of the carbon atomic orbitals leads to strong bonds in a two-dimensional plane (we choose the $xy$ plane, without loss of generality). In the third spatial direction, the atoms are coupled by van der Waals forces, resulting in much weaker bonds. Graphite can therefore be seen as a stack of twodimensional layers only weakly coupled in the third dimension. These twodimensional layers are graphene. Due to the interest in the properties of graphite, graphene has been studied theoretically from as early as 1947 [17].

The Brillouin zone (BZ) of graphene exhibits two points of special interest, the so-called Dirac points ($\vec{K}, \vec{K}'$) at the corners of the first BZ. Around these points, $E(\vec{k})$ can be written as [20]

$$E_{\pm}(q) = \pm v_{\mathrm{F}}|q| + O\left[(q/K)^2\right] \tag{2.48}$$

Here, $\vec{k} = \vec{K} + \vec{q}$, where $|\vec{q}| \ll \left|\vec{K}\right|$. The Fermi velocity $v_{\mathrm{F}}$ is of the order $v_{\mathrm{F}} \approx 1 \times 10^6\,\mathrm{m/s}$.

The dispersion relation $E(\vec{k})$ is shown in Fig. 2.10 (a) as a function of $k$. As a function of $k_x, k_y$, $E(\vec{k})$ becomes a cone, as shown in Fig. 2.10 (b). These are the so-called Dirac cones. As in the case of semiconductors, the conduction in the upper band is mediated by electrons, while for the lower bands, the charge carriers are holes.

Equation 2.48 is a linear dispersion relation between energy and momentum, $E \propto q$. This is similar to the particles described by the Dirac equation, which combines quantum mechanics and special relativity. In fact, around the Dirac points the charge carriers can be described by an equation formally equivalent to the Dirac equation, only exchanging the speed of light by $v_{\mathrm{F}}$. Therefore, the conduction electrons in graphene can be seen as relativistic particles.

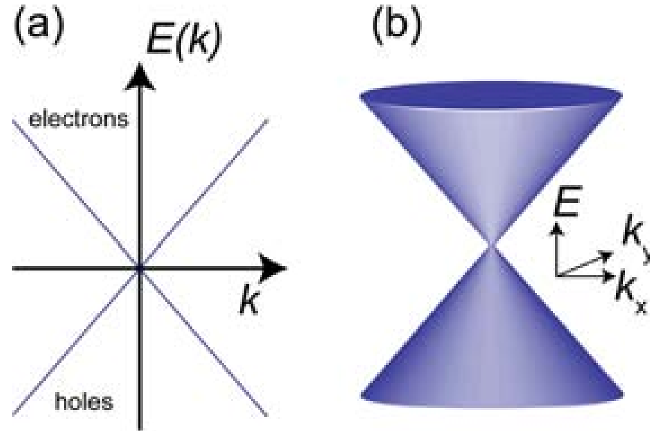


Figure 2.10.: Dispersion relation of graphene close to the Dirac points (a) in one dimension in $k$ space (b) in two dimensions in $k$-space, forming the so-called Dirac cone

In the following, we show how these properties of the band structure of graphene can be derived in an elementary way from its crystal lattice. The calculation is based on the tight-binding method, which is a method to calculate the bandstructure of a given materials based on a linear combination of its atomic orbitals [29]. Tight-binding calculations take into account that some of these orbitals might form non-negligible overlaps by introducing correction terms to the simple atomic picture.

The crystal structure of graphene is a hexagonal honeycomb as shown in Fig. 2.11. It can be understood as a triangular lattice, where the unit cell consists of two atoms. The lattice vectors are given by [17]

$$\vec{a}_1 = \frac{a}{2}(3, \sqrt{3}), \quad \vec{a}_2 = \frac{a}{2}(3, -\sqrt{3}) \tag{2.49}$$

where $a = 1.42\,\text{Å}$ is the lattice constant.

It is also possible to understand the crystal structure of graphene as the superposition of two identical sublattices $A$ and $B$, as indicated in Fig. 2.11.

In order to understand electronic transport in graphene, we consider an electron siting at site $\vec{R}_i$ on sublattice $A$. There are three nearest neighbors in the vicinity of $\vec{R}_i$ in a distance $a$, and six second nearest neighbors. It becomes clear that the nearest neighbors belong to sublattice $B$ and the second nearest neighbors to sublattice $A$. Disregarding higher order contributions, we can therefore describe the proces via a creator/annihilator algebra for both sublattices.

Be $a_{i,\sigma}$ an operator which annihilates an electron with spin $\sigma =\uparrow, \downarrow$ on site $\vec{R}_i$ of sublattice $A$, and $a^*_{i,\sigma}$ an operator which creates an electron with spin $\sigma$ on site $\vec{R}_i$.

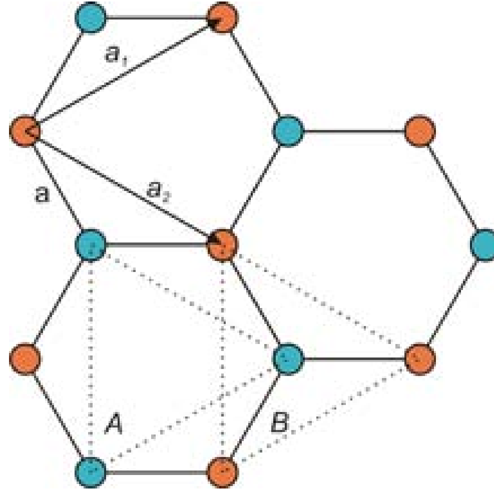


Figure 2.11.: The crystal structure of graphene forms a hexagonal honeycomb pattern with lattice constant a and lattice vectors $a_1$ and $a_2$. The structure can also be seen as a triangular lattice with two atoms in per unit cell, resulting in sublattices $A$ and $B$.

We define $b_{i,\sigma}$ and $b^*_{i,\sigma}$ in an analog fashion for sublattice $B$. Using these definitions, the tight-binding Hamiltonian for hopping of electrons between nearest and second nearest neighbors takes the following form [20]

$$H = \underbrace{-t \sum_{\langle i,j\rangle,\sigma} (a^\dagger_{\sigma,i} b_{\sigma,j} + a_{\sigma,i} b^\dagger_{\sigma,j})}_{\text{hopping nearest neighbors}} \underbrace{- t' \sum_{\langle i,j\rangle,\sigma} (a^\dagger_{\sigma,i} a_{\sigma,j} + b^*_{\sigma,i} b_{\sigma,j} + \text{H.c.})}_{\text{hopping 2nd nearest neighbors}} \tag{2.50}$$

where we set $\hbar = 1$ and H.c. is the Hermitian conjugate. The first term stands for the hopping of electrons to the nearest neighbors, while the second one accounts for the hopping to the second nearest neighbors. The parameters $t$ and $t'$ are the related hopping energies. Here, $t \approx 2.8\,\text{eV}$ [20], while $t'$ has recently been determined experimentally to $t' \approx 0.3\,\text{eV}$ [48].

The energy bands derived from the tight-binding Hamiltonian read [17]

$$\begin{aligned} E_\pm &= \pm\, t\sqrt{3 + f(\vec{k})} - t' f(\vec{k}), \quad \text{where} \\ f(\vec{k}) &= 2\cos(\sqrt{3}k_y a) + 4\cos\left(\frac{\sqrt{3}}{2}k_y a\right)\cos\left(\frac{3}{2}k_x a\right) \end{aligned} \tag{2.51}$$

Here, the + sign refers to the upper and the - sign to the lower band. Now, we can obtain Eq. 2.48 by expanding the dispersion relation 2.51 around the Dirac points.

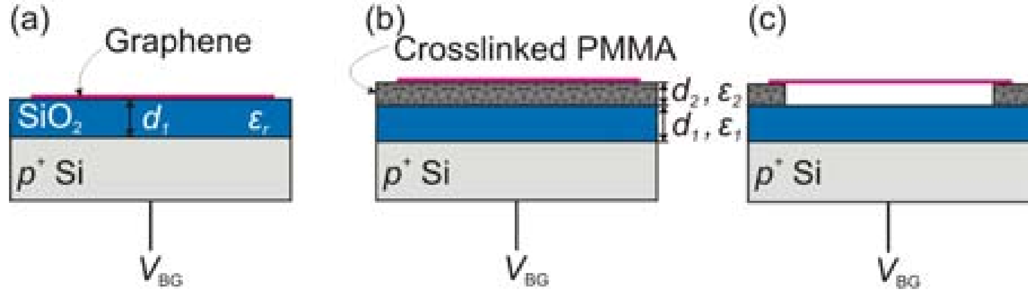


Figure 2.12.: Field effect in graphene for different substrates (a) Graphene sheet and $p^+$ Si can be seen as two plates of a two dimensional capacitor (b) Graphene on top of serveral dielectrica, the insulating layers can be seen as capacitors in series. (c) Suspended graphene: Here, the second dielectric is vacuum

## 2.8.3. The Electric Field Effect

### Carrier Density

The electric field effect of graphene means that the charge carrier concentration of graphene can be tuned by applying an external field [18]. It is thus a tool to change properties such as conductivity and resistivity. Here, we show how the strenght of the electric field close to the graphene depends on the thickness and dielectric constant on which graphene is deposited.

We consider the following cases, as shown in Fig. 2.12, the field effect for one or multiple dielectrica in series.

1. **The electric field effect for one dielectric** *(Figure 2.12)* (a)
The graphene flake can be seen as one plate of a two dimensional capacitor. The $p$ doped Si substrate serves as the second electrode, while the two are separated by the dielectric material $SiO_2$. For a capacitor it is valid [49] that $C = Q/U$, where $Q = N \cdot e$ is the charge of the graphene flake and $U = V_{\mathrm{BG}}$ is the backgate voltage applied to the Si substrate. The capacitance $C$ of a two dimensional capacitor is given by $C_{\mathrm{Diel}} = (\varepsilon_0 \varepsilon_r / d) A$, where $\epsilon_0$ is the dielectric constant, $\epsilon_r$ the relative dielectric constant of the $SiO_2$, $d$ the distance between the plates (the thickness of the $SiO_2$) and $A$ the area of the flake. Using $n = N/A$, we obtain for the carrier concentration of the graphene [18]
$$n = \frac{\varepsilon_0\, \varepsilon_r}{d\, e} V_{\mathrm{BG}} \tag{2.52}$$
The carrier concentration depends linearly on the backgate voltage, and for a voltage $V_{\mathrm{BG}} = 0$ it follows that $n = 0$. Here, we assume that the Dirac point $V_{\mathrm{D}}$ lies at zero backgate voltage. In experimentally fabricated graphene,

a shift is observed frequently and in the above formulas we have to substitute $V_{\mathrm{BG}} \mapsto V_{\mathrm{BG}} - V_{\mathrm{D}}$.

2. **Multiple dielectrica in series** *(Figure 2.12 (b), (c))*
   For the graphene devices, as shown in chapter 3.4.4 and 3.4.5, we have to extend the above formula in order to use it for different substrates. In both cases, an additional dielectric layer separates the $p$ doped Si and the graphene. We can therefore see these systems, as shown in Fig. 2.12, as two capacitors in series. The total capacitance of such a system is given by [49] $1/C = \sum_i 1/C_i$. Therefore, Eq. 2.52 becomes

$$n = \frac{\varepsilon_1\,\varepsilon_0}{e(d_1 + d_2\frac{\varepsilon_1}{\varepsilon_2})} V_{\mathrm{BG}} \tag{2.53}$$

In summary, in both cases the carrier density can be expresed as

$$n = \alpha V_{\mathrm{BG}} \tag{2.54}$$

As shown, the parameter $\alpha$ depends on the geometry as well as on the material properties of the system.

### Gate Capacity

The capacity $C_g$ between gate and substrate is closely related to the factor $\alpha$. The charge carrier concentration of a $2D$ capacitor is given by $n \cdot e = C_g \cdot V_{\mathrm{BG}}$. Since $n = \alpha V_{\mathrm{BG}}$ it immediately follows that

$$C_g = e \cdot \alpha \tag{2.55}$$

For instance, in case of non suspended samples, that means that

$$C_g = \frac{\varepsilon_0 \varepsilon_r}{d} \tag{2.56}$$

For our devices, we obtain

| Dielectrica | $\alpha$ $[10^9 \mathrm{V}^{-1}\mathrm{cm}^{-2}]$ | $C_g$ $[\frac{\mathrm{aF}}{\mu\mathrm{m}^2}]$ |
|---|---|---|
| 440 nm $SiO_2$ | 49 | 78,5 |
| 285 nm $SiO_2$ / 200 nm PMMA | 44,5 | 71,2 |
| 285 nm $SiO_2$ / 200 nm vacuum | 20 | 32 |

### Seebeck coefficient

As noted in section 2.2, the Mott relation of the Seebeck coefficent reads

$$S = -\frac{\pi^2 k_{\mathrm{B}}^2 T}{3|e|}\frac{1}{\sigma}\frac{\partial\sigma}{\partial V_g}\frac{\partial V_g}{\partial E}|_{E=E_{\mathrm{F}}} \tag{2.57}$$

where

$$\frac{\partial V_g}{\partial E_{\mathrm{F}}} = \sqrt{\frac{|e|}{C_g\pi}}\frac{2}{\hbar v_{\mathrm{F}}}\sqrt{|\Delta V_g|} \tag{2.58}$$

with the Fermi velocity $v_{\mathrm{F}}$ and $\Delta V_g = V_g - V_{\mathrm{D}}$. Therefore, $S$ can be written as

$$\begin{aligned} S &= -\tfrac{\pi^2 k_{\mathrm{B}}^2}{3|e|}\sqrt{\tfrac{|e|}{C_g\pi}}\tfrac{2}{\hbar v_{\mathrm{F}}}T\cdot\sqrt{|\Delta V_g|}\tfrac{1}{\sigma}\tfrac{\partial\sigma}{\partial V_g} \\ &= A\cdot\sqrt{|\Delta V_g|}\tfrac{1}{\sigma}\tfrac{\partial\sigma}{\partial V_g} \end{aligned} \tag{2.59}$$

where $A$ is a parameter depending on the geometry and on the temperature of the sample. For our different types of sample we obtain

| Dielectrica | $A$ at RT | $A$ at 77 K | $A$ at 4.2 K |
|---|---|---|---|
| 440 nm $SiO_2$ | $564\cdot10^{-6}$ | $145\cdot10^{-6}$ | $7.9\cdot10^{-6}$ |
| 285 nm $SiO_2$ / 200 nm PMMA | $578\cdot10^{-6}$ | $149\cdot10^{-6}$ | $8.1\cdot10^{-6}$ |
| 285 nm $SiO_2$ / 200 nm vacuum | $1111\cdot10^{-6}$ | $285\cdot10^{-6}$ | $15.6\cdot10^{-6}$ |

Finally, the latter three expressions in eq. 2.59 can be obtained by measuring $\sigma(V_{\mathrm{BG}})$ and numerically processing the data.

### Residual Carrier Concentration

The carrier concentrations given by eq. 2.54 are calculated taking into account only the effect of the electric field and the nature of the graphene crystal. However, extrinsic sources such as impurities, adatoms or ripples in the graphene also contribute to the carrier concentration. This can be accounted for by expressing the total carrier concentration as [50]

$$n_{\mathrm{tot}} = \sqrt{n_0^2 + n(V_{\mathrm{BG}})^2} \tag{2.60}$$

For our devices, the residual carrier concentration is of the order of $n_0 = 10^{11}\,\mathrm{cm}^{-2}$, meaning that it can be mostly neglected. However, close to the Dirac point, the residual carrier concentration matters, as we show graphically in Fig. 2.13 Especially, when extracting the mobilities of the devices, it is important to take into account the extrinsic carrier concentration at the Dirac point as we show in the following section.

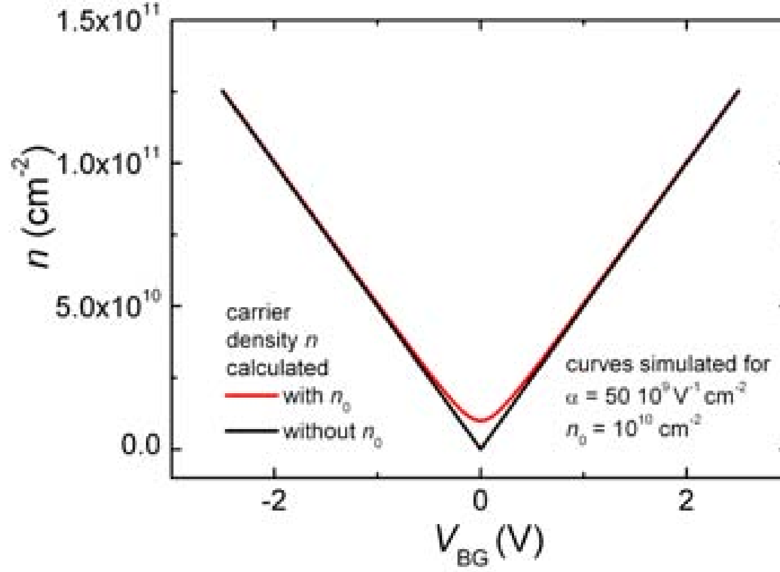


Figure 2.13.: Comparision of the carrier densities according to formulas 2.52 and 2.60. The former formula neglects the finite carrier concentration $n_0$ at the Dirac point.

### 2.8.4. Mobility

The mobility $\mu$ of the charge carriers is a quantity often used in semiconductor physics. It is a measure of how well the charge carrier move via a given material, closely related to the density of carriers and the conductivity. The conductivity can be written as $\sigma = n \cdot e \cdot \mu$. For semiconductors, as well as for graphene, one has to include the contributions of electrons and holes [29] $\sigma = e(n_e\mu_e + n_h\mu_h)$, where $n_e$ and $\mu_e$ stands for the concentration and mobility of the electrons, and $n_h$ and $\mu_h$ for those of the holes.

In general, we can express the mobility of the charge carriers as

$$\mu = \frac{\sigma(V_{\mathrm{BG}})}{e\,n(V_{\mathrm{BG}})} \tag{2.61}$$

Here, the conductivity of graphene is a quantity which can be obtained by transport measurements, while the carrier density can be calculated as described in the previous section. Various models have been developed in order to take into account the residual carrier concentration $n_0$ [50, 51]. If $n_0$ is neglected, $\mu$ is infinite at the Dirac point according to Eq. 2.61, which makes no sense physically.

Therefore, we calculate the mobilities of our samples in two different ways. First, we use the standard formula 2.61. We then fit our data to a model [50], which delivers

the residual carrier concentration $n_0$. Obviously, we have to disregard all values below $n_0$, as demonstrated graphically in Fig. 5.2.
The model used for the fitting accounts for the effect of the finite intrinsic carrier concentration as well as the contact resistance $R_C$ [50]. The mobility is a constant fitting parameter within the model and the total resistance $R_{\text{tot}}$ of a device measured in 4 point configuration is given by

$$R_{\text{tot}} = R_C + \frac{1}{e\mu\sqrt{n_0^2 + n(V_{\text{BG}})^2}} \tag{2.62}$$

The constant mobilities extracted by the fitting correspond well with the values extracted by the standard formula close to $n_0$.

## 2.9. Spin Relaxation in Graphene

### 2.9.1. Introduction

The phenomenological model of spin injection and detection in metals, as described in section 2.5, is applicable to graphene with only minor modifications. These basically consist of substituting three-dimensional quantities by their two-dimensional counterparts. For example, the cross section of the non magnetic material $A_N$ is substituted by the width $W$ of the graphene flake in Eq. 2.34. The equation then reads $\Delta R_{\text{NL}} = ((P_J^2 \lambda_N)/(\sigma_N W)) \exp(-l/\lambda_N))$. Here, the quantity $\sigma_N$ is the two-dimensional conductivity of graphene and unlike for metals, $\sigma_N = \sigma_N(V_{\text{BG}})$. However, apart from these modifications, we can apply the model of spin injection and detection in non magnetic materials as developed in section 2.5.

Here, we instead focus on the features of graphene that make it a promising candidate for applications in spintronics.

To start with, graphene exhibits excellent electrical properties [20]. High mobilities and the ability to tune the charge carrier concentration allow for studies which are not possible in metals, where the carrier concentration can not be varied by an external gate. The fact that the conduction electrons behave as relativistic particles makes graphene an even more interesting physical system. Moreover, the band structure of graphene can be tuned by the introduction of adatams [52]. Finally, as a gapless semiconductor, graphene allows for fascinating experiments combining spin and charge, as we show in chapter 7.

In the context of spintronics, it is important to note that Carbon is a relatively light material (Z = 6) and the spin-orbit interaction is low. The most frequent isotope, $^{12}$C, has no nuclear spin an thus no hyperfine interaction. Therefore, long spin relaxation lengths of several $\mu$m can be expected. This is longer than in most metals, where $\lambda_{\text{sf}}$ is of the order of tens or hundreds of nm [53]. In fact, first successful experiments

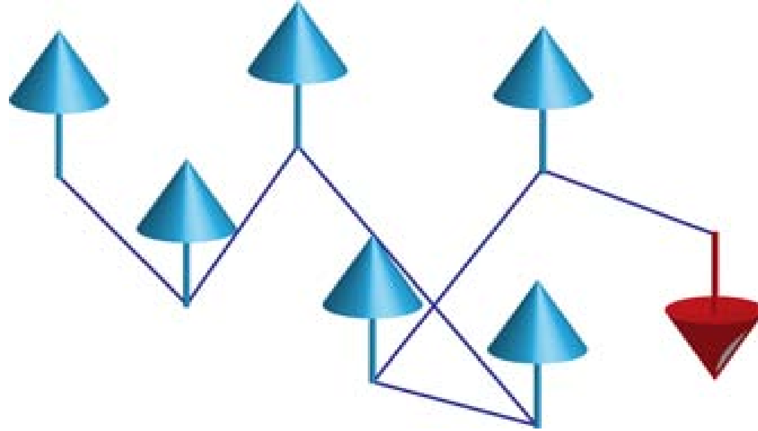

Figure 2.14.: Schematic representation of Elliot Yafet spin relaxation

on spin injection in graphene have demonstrated $\lambda_{\mathrm{sf}}$ of the order of a few microns [54, 55, 56, 57]. These experiments have been carried out in relatively dirty systems with low mobilities or in multilayer graphene. Fueled by the experimental results, theorist have predicted $\lambda_{\mathrm{sf}}$ of the order of tens or hundreds of $\mu$m in clean, high mobility systems [58, 59]. These predictions are based on extrapolations of the Elliot-Yafet (EY) as well as by the D'yakonov-Perel (DP) spin relaxation mechanism, which we introduce in the following.

### 2.9.2. Elliot-Yafet Spin Relaxation

The EY mechanism is schematically shown in Fig. 2.14. A conduction electron gets scattered several times while passing through a given material. There is a finite probability of a spin flip during scattering events, so the electron eventually changes its spin orientation.

EY spin relaxation is often the dominant spin relaxation mechanism in metals, as this type of relaxation appears in systems where spin orbit coupling is present together with an inversion symmetry of the crystal lattice.

The presence of the spin orbit interaction has an effect on the Bloch states of the material, which become linear combinations of up and down states, $|\uparrow\rangle$ and $|\downarrow\rangle$. If the system exhibits inversion symmetry, they can be written as [60]

$$\begin{aligned}\psi_{\vec{k}n\uparrow}(\vec{r}) &= [a_{\vec{k}n}(\vec{r})\,|\uparrow\rangle + b_{\vec{k}n}(\vec{r})\,|\downarrow\rangle]e^{i\vec{k}\cdot\vec{r}} \\ \psi_{\vec{k}n\downarrow}(\vec{r}) &= [a^*_{-\vec{k}n}(\vec{r})\,|\downarrow\rangle + b^*_{-\vec{k}n}(\vec{r})\,|\uparrow\rangle]e^{i\vec{k}\cdot\vec{r}} \end{aligned} \tag{2.63}$$

where $a$ and $b$ are lattice vectors, given by the periodicity of the crystal. For $|a| = 1$ and $|b| = 0$, these wavefunctions become simply $|\uparrow\rangle$ and $|\downarrow\rangle$, while for $|a|, |b| \neq 0$, the spin up and down states mix. In most cases however, $|a|$ is close to one and $|b| \ll 1$

[15]. Pertubation theory delivers $|b| \approx \Delta_{so}/\Delta E \ll 1$, where $\Delta E$ is the difference in energy between a given state in one energy band and the nearest state in another band with the same momentum, and $\Delta_{so}$ is the SO coupling between these two states.

At high temperature, elastic scattering is mainly caused by phonons, while at low temperature, scattering with impurities is the dominant cause. Direct coupling of phonons with the spin up and down states have been studied and introduced to the model by Yafet [61].
The Elliot relation contains the scattering time $\tau_e$, the spin flip time $\tau_{sf}$ and relates those to the shift of the electronic g-factor $\tau_e/\tau_{sf} \approx (\Delta g)^2$. In the Born approximation, this can be estimated to

$$\tau_e/\tau_{sf} \approx \langle b^2 \rangle = (\Delta_{so}/\Delta E)^2 \tag{2.64}$$

Therefore, if the EY spin relaxation mechanism is the dominant one in a given material, the mean free time $\tau_e$ is proportional to the spin flip time $\tau_{sf}$, $\tau_{el} \propto \tau_{sf}$. It becomes clear that $\tau_{sf}$ depends inversely on the strength of the spin orbit interaction.

In graphene, the SO interaction close to the Dirac point can be expressed as [58]

$$\Delta_{so} = \Delta_{curv} + \Delta_{ext} \tag{2.65}$$

Here, $\Delta_{curv}$ is the SO interaction due to curvature of the graphene sheet and $\Delta_{ext}$ the contribution due to external fields. The spins precess around the effective SO field with the the spin precession length $l_{prec} = 2\pi v_F/\Delta_{so}$ [59].

As the electrons traverse graphene, they weakly scatter off the ions. During these scattering events a certain amount of spin relaxes given by [59] $\Delta_{so}/v_F k_F$. After $N$ collisions, the amount equals $\sqrt{N}\Delta_{so}/v_F k_F$. Dephasing occurs when $\sqrt{N}\Delta_{so}/v_F k_F = 2\pi$.

Since $\tau_{sf} = N \cdot \tau_e$, we obtain

$$\tau_{sf}^{EY} = \tau_e \frac{4\pi^2 v_F^2 k_F^2}{\Delta_{so}^2} \tag{2.66}$$

and

$$\lambda_{sf}^{EY} \sim \lambda_e \frac{v_F k_F}{\Delta_{so}} \tag{2.67}$$

The last relation follows from the fact that $\lambda_{sf} = \sqrt{D \cdot \tau_{sf}}$ and $D = v_F^2 \tau/2$.

### 2.9.3. D‘yakonov-Perel Spin Relaxation

D´yakonov and Perel [62] have described a mechanism of spin relaxation in systems lacking inversion symmetry in their crystal lattice. There, states within the same band of the same momentum $\vec{k}$, but with opposite spins are not degenerate, $E_{\vec{k}\uparrow} \neq E_{\vec{k}\downarrow}$. Therefore, these states are spin split. The effect on the spin orbit coupling can be

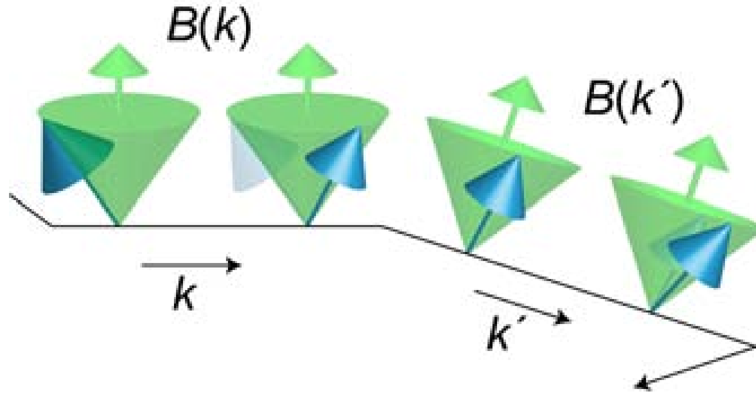


Figure 2.15.: Schematic representation of spin relaxation according to the D'yakonov-Perel mechanism

described as an effective magnetic field $\vec{B}(\vec{k})$ which depends in strength and direction on the wavevector $\vec{k}$ of the electrons.

The DP mechanism is schematically shown in Fig. 2.15. The spins precess around $B(\vec{k})$. As the field depends on $\vec{k}$, a distribution of electrons with different $\vec{k}$ would lose a prepared spin orientation fast. However, typically there are many scattering events changing rapidly the momentum and effective magnetic field (to $B(\vec{k'})$ in the figure), before a spin can precess only once. This results in a supression of the spin relaxation and is called motional narrowing.

In graphene, the corresponding spin relaxation time can be expressed as [59]

$$\tau_{\mathrm{sf}}^{\mathrm{DP}} \approx \frac{v_{\mathrm{F}}}{\lambda_e \Delta_{\mathrm{so}}^2} = \frac{1}{\tau_e \Delta_{\mathrm{so}}^2} \tag{2.68}$$

and

$$\lambda_{\mathrm{sf}}^{\mathrm{DP}} = \frac{v_{\mathrm{F}}}{\sqrt{2}\Delta_{\mathrm{so}}} \tag{2.69}$$

Therefore, if the spin relaxation in graphene is dominated by the DP mechanism, then $\tau_{\mathrm{sf}} \propto \tau_e^{-1}$.

## 2.9.4. Comparison between EY and DP Mechanism

Both the EY as well as the DP mechanism are due to SO interaction. However, in case of the EY mechanism, the spin relaxation takes place during the scattering events, while for the DP mechanism, it happens in between these events.

In both cases $\tau_{\mathrm{sf}} \propto \Delta_{\mathrm{so}}^{-2}$ and $\lambda_{\mathrm{sf}} \propto \Delta_{\mathrm{so}}^{-1}$. Therefore, in systems with low spin orbit interaction, the spin relaxation times and lengths are long. The smaller $\Delta_{\mathrm{so}}$, the larger the values of both $\tau_{\mathrm{sf}}$ and $\lambda_{\mathrm{sf}}$.

The relations 2.66 and 2.68 show how $\tau_{\mathrm{sf}}$ scales with the elastic mean free path of the electrons. From the nature of the the two spin relaxation mechanisms however, one should expect that the EY mechanisms dominates in samples of low mobility and DP in samples of high mobility, as the time between scattering events increases for cleaner samples. The DP mechanism should hence constitute an upper limit for the spin relaxation time and length in graphene.

The relation between scattering time $\tau_e$ and spin flip time $\tau_{\mathrm{sf}}$ is often used to distinguish between relaxation mechanisms. If the origin of spin relaxation in a given material is given by the EY mechanism, it is valid that $\tau_e \propto \tau_{\mathrm{sf}}$, while for the DP mechanism $\tau_e \propto \tau_{\mathrm{sf}}^{-1}$. This approach has been used to analyze a number of experiments in graphene.

### 2.9.5. Experimental Results

Several experimental studies have found the EY relaxation mechanism to be the dominant one in graphene [63, 64, 65], but examples exist where the DP mechanism dominates the spin relaxation [66]. Moreover, Han *et al.* have found the spin relaxation at low temperatures to be dominated by EY in SLG, but by the DP mechanism in bilayer graphene (BLG) [67].

Recently, studies of spin injection in high mobility samples have become available as well [68, 69]. Also here, $\lambda_{\mathrm{sf}}$ has been found to be of the order of a few $\mu$m. It is therefore obvious that the simple extrapolation based on the EY mechanism does not hold, leading to the conclusion that the initial theoretical predictions have overlooked limiting factors for the spin relaxation in graphene.

These findings underline the need to further investigate the spin relaxation in graphene, both theoretically and experimentally.

### 2.9.6. Further Mechanisms of Spin Relaxation in Graphene

Concluding the chapter, we discuss possible causes for spin relaxation in graphene apart from the EY and the DP mechanism.

Imperfections in the graphene crystal lattice can be taken into account by introducing a Gauge Field (GF) tensor $A(\vec{r})$, which is proportional to the strain tensor $u_{ij}(\vec{r})$. The GF leads to a pseudomagnetic field $B_\perp$, which is perpendicular to the plane of the graphene, and thus perpendicular of the polarization of the injected spins as well. The presence of $B_\perp$ leads to different spin relaxation times for spins in and out of plane [59].

At the same time, it is an intriguing possibility to obtain high pseudomagnetic fields by choosing the right strain applied to the graphene sheet. This approach has become known as strain engineering, and fields of tens of Tesla have been predicted by choosing the appropriate strain tensor $u_{ij}$ [70]. Experimentally, even higher pseudomagnetic fields have been demonstrated in the vicinity of nanobubbles on top of graphene [71].

Recently, it has been proposed that the spin relaxation in graphene is due to an entanglement between spin and pseudospin mediated by spin orbit interaction [72].

Another possible reason for spin relaxation in graphene are impurities in the graphene crystal or in the substrate. The substrate itself has been identified to affect the properties of graphene. It is therefore desireable to eliminate the substrate by suspending the graphene spin valves [68]. Measurements of such systems can be found in chapter 5.

# 3. Experimental Techniques and Methods

## 3.1. Introduction

Throughout this chapter, we describe the experimental techniques used for the fabrication of our nanoelectronic devices.

Firstly, in section 3.2, we describe the efforts we have taken in the context of this thesis in order to obtain and characterize single layer graphene.

Secondly, in section 3.3, the results obtained concerning the fabrication of crosslinked PMMA structures are summarized. The method presented here is is the first step in the fabrication of our graphene devices.

In section 3.4, we discuss techniques needed for the device fabrication. This includes electron-beam lithography as well as selection of the substrate for graphene exfoliation. Finally, we discuss the fabrication of freely suspended graphene spin valves.

As a concluding section, we discuss the experimental setup and basic electrical connections used for the measurements on our devices.

## 3.2. Fabrication and Characterization of Single Layer Graphene

### 3.2.1. Mechanical Exfoliation

There are several techniques in order to obtain single layer graphene (SLG) flakes, which include chemical vapor deposition (CVD) [73], molecular beam epitaxy (MBE) [74] and synthesis on a Silicon carbide substrate [75]. Throughout this thesis, we have exclusively used mechanically exfoliated graphene, as it is among the highest quality graphene in terms of mobility [19].

Mechanical exfoliation of graphene is commonly known as the Scotch tape method [18]. Since graphite consists of several layers of graphene only weakly bond to each other by van der Waals interaction, intact graphene sheets can be obtained by peeling off layers from the bulk. Hence, the quality of the graphite is a determining factor for the quality of the graphene flakes [21], which makes it mandatory to use high quality graphite as bulk material.

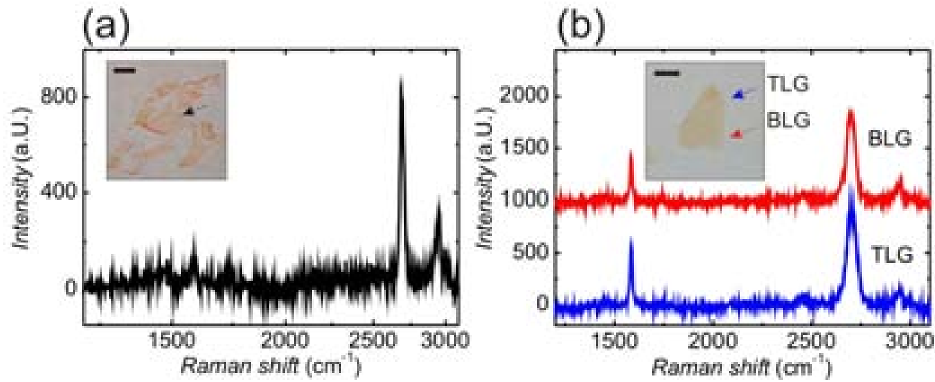


Figure 3.1.: Raman spectra of graphene: (a) Single layer graphene. (b) Bilayer and triple layer graphene. Spectrum of BLG shifted for clarity. Insets: Optical microscope images of the flakes. The scale bar equals 2 $\mu$m.

The graphite flakes or nuggets are applied to a piece of wafer tape or common Scotch tape. Pressing a flake between two adhesive layers of tape and carefully separating the tapes again results in increasingly thin layers of graphite. At a certain point, these layers start to become transparent to light, indicating that the graphite consists only of a few layers of graphene. Pressing the tape on a substrate, e.g. Si/$SiO_2$, it is likely that in some areas graphene flakes stick to the substrate when the tape is removed. Once deposited on the substrate, the graphene can be further processed by nanolithography methods such as electron beam lithography (see section 3.4) or local anodic oxidation with an atomic force microscope (AFM) [76].

### 3.2.2. Optical Characterization and Raman Spectroscopy

Despite being atomically thin, graphene can be visualized by an optical microscope if the thickness of the $SiO_2$ is appropriate [21, 77], due to an interference effect between the light backscattered from the empty wafer and the flake. An optical microscope image of exfoliated graphite can be seen in the inset of Fig. 3.1 (a). The flake is exfoliated on a Si/$SiO_2$ substrate, where the thickness of the $SiO_2$ is 440 nm.

It is indeed possible to determine the number of graphene layers of a flake by carefully examining its color and transparency. However, in order to verify that the determined number of layers in a given area is correct, it is necessary to quantify the number of layers of a reference sample beforehand. A fast and reliable method in order to achieve that is by measuring Raman spectra [78], which requires to center the monochromatic light of a laser on the material under examination. Inelastic scattering between between phonons with photons cause a shift in frequency of the photons, leading to a resonance spectrum of the scattered light characteristic for each material.

The Raman spectrum of SLG consists of a characteristic peak close to 2700 $cm^{-1}$,

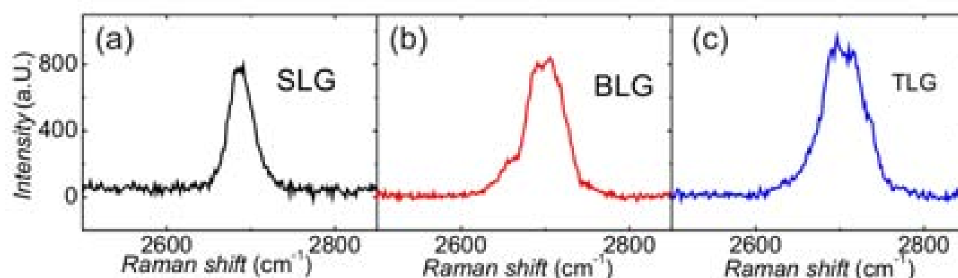


Figure 3.2.: The $2D$ peak for (a) SLG (b) BLG (c) TLG

the $2D$ peak of graphene [79]. For multi layer graphene (MLG), a second peak appears in the spectrum, the $G$ peak at $1600\,\mathrm{cm}^{-1}$. Moreover, the shape of the $2D$-peak serves as additional indication for the number of layers [79].

Raman spectra of SLG, bilayer graphene (BLG) and triple layer graphene (TLG) are shown in Fig. 3.1. These flakes are exfoliated on $SiSiO_2$ substrates (440 nm oxide thickness), optical microscope images are shown in the inset of the figure. The flake shown in Fig. 3.1 (b) consists of two areas of different thickness, where we have performed two independent Raman measurements.

It becomes clear that the spectrum shown in (a) is indeed a SLG Raman spectrum, as the $G$ peak is not visible. It is also clear that the flake shown in Fig. 3.1 (b) is an example of MLG, as the spectra, measured at the two different locations indicated by the arrows, exhibit the $G$ peak.

Figure 3.2 shows in detail $2D$ peaks of the same samples. In SLG, the $2D$ peak consist of a single component, while for higher number of layers, the peak evolves into multiple components. It is therefore possible to identify the Raman spectrum shown in Fig. 3.2 (b) as that of BLG, and the one in (c) as TLG.

Then, using the optical microscope images of these selected flakes as reference, one can thus reliably determine the number of layers of a graphene flake. We have repeated the Raman measurements for each type of substrate used for this thesis, obtaining consistent results.

### 3.2.3. AFM characterization

Another method commonly used to charcterize graphene is atomic force microscopy. It provides deep information about height, impurities, ripples and edges of the graphene flakes. Therefore, in order to ensure the highest possible quality of the graphene, one should perform AFM characterization measurements on flakes choosen for devices.

The working principle of an AFM is relatively straightforward [80]. An atomically small tip, a so-called cantilever is moved across the surface of a sample, driven by a set of piezo crystals controlling the lateral movement. As the tip moves across the surface,

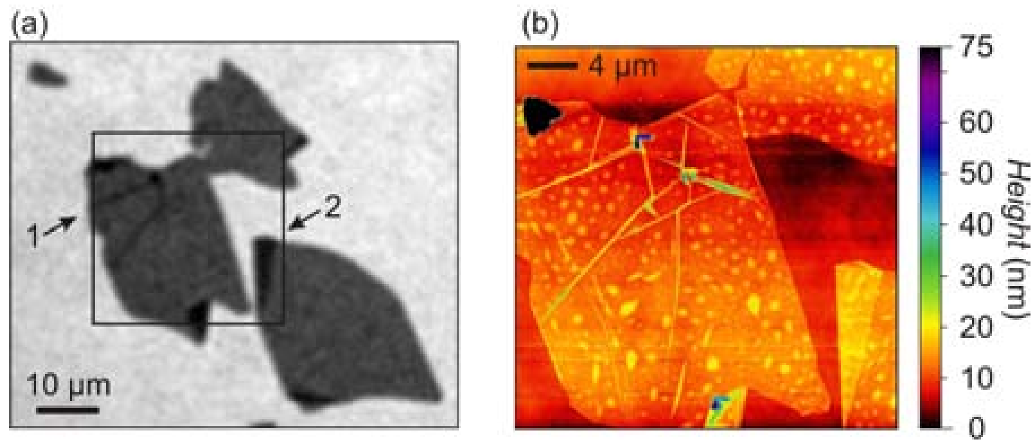


Figure 3.3.: Comparision between (a) optical microscope image and (b) AFM scan

the cantilever bends depending on the height of the substrate. A laser is focused on the back of the cantilever, so that the bending leads to an interference pattern, which can be translated into the height of the substrate. Thanks to the small radius of the tip (here $\sim 10\,\mathrm{nm}$) and the precision of the piezo crystals, a resolution well below the optical limit is achieved.

An optical microscope image of a multi layer graphene (MLG) flake is (a) as well as an AFM image (b) is shown in Fig. 3.3. Here, we have postprocessed the optical image in order to increase the visibility of the flake by displaying the image on a grey scale while increasing the contrast.

While most of the flake appears uniform in the optical microscope image, there are some lines visible in the upper half of the flake, as indicated by arrow 1. The AFM scan reveals these lines as ripples, i.e. areas where the flake contracted during deposition. These ripples perturb the crystal lattice of the graphene and might lead to a diminished mobility as well as to diminished spin relaxation times, as discussed in sections 2.8 and 2.9.

Moreover, it can be distinguished in Fig. 3.3 (a) that some of the edges of the flakes are folded, as indicated by arrow 2. This occurs frequently if the edges of exfoliated graphene do not stick well to the substrate. SLG also shows the tendency to roll up. The AFM scan confirms that the flake is folded in that area.

Furthermore, there are several dots on top of the flake, which might be due to contamination, hinting to a further degradation of the quality of the graphene.

A second example is shown in Fig. 3.4. Here, the dimensions of the graphene are so small that the optical microscope image does not provide any conclusion concerning the quality of the graphene.

Nevertheless, the AFM scan shown in Fig. 3.4 (b) reveals that in this case the surface does not present any of the defects discussed in the previous sample (Fig. 3.3). The flake is free of ripples, folded edges or contamination and would be an ideal

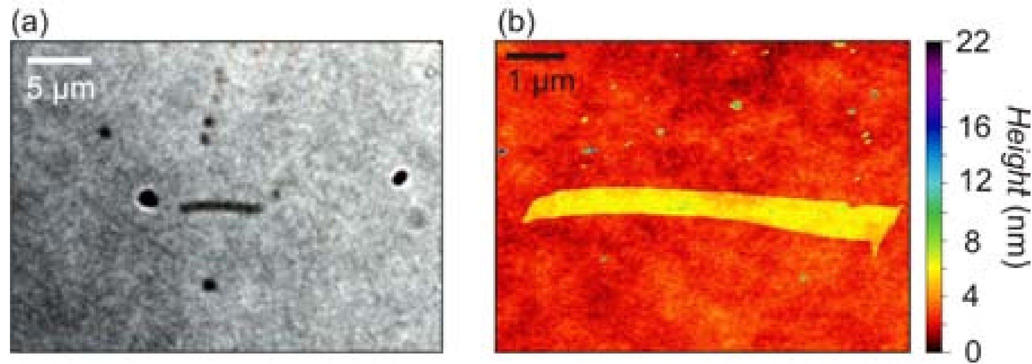


Figure 3.4.: Comparision between (a) optical microscope image and (b) AFM scan

candidate for further processing.

## 3.3. Properties of Crosslinked PMMA

### 3.3.1. Crosslinking PMMA

Throughout this thesis, we present spin injection measurements on graphene spin valves on different substrates. We have fabricated freely suspended graphene spin valves as well as spin valves on poly(methyl methacrylate) (PMMA) substrates. Both types require the use of crosslinked PMMA, which we discuss in the following, while the complete fabrication process of each type of sample is given in section 3.4.

PMMA is one of the most common polymers used in the fabrication of nanodevices [81]. It is often used as positive resist in electron beam lithography, which we describe in section 3.4. Here, we focus on the properties of crosslinked PMMA and present the results of extensive tests. These test have been performed in order to use crosslinked PMMA in combination with more established EBL techniques [82], as described in section 3.4.4 and 3.4.5.

PMMA can also be used as a negative resist by exposing the polymer to a dose approx. 20 times higher than that required in the regular process. The overexposure results in a crosslinking of the PMMA molecules, which perform a so-called glass transition. Although the technique is well-known [83], considerable efforts have been taken in the context of this thesis in order to apply it to the fabrication of freely suspended graphene spin valves.

These efforts have been necessary for two reasons:

1. Reports in the literature on crosslinked PMMA in combination with conventional EBL are rather scarce. If any, there are reports on using crosslinked PMMA as a substrate for graphene [84], or as insulating layer in order to fabricate a topgate over an otherwise completed device [63, 85, 86, 87]. In these cases, it is sufficient

to crosslink a rectangular area of dimensions considerably larger than the device itself.

However, in order to suspend graphene using crosslinked PMMA structures, a high precision of the process is required. In the following we demonstrate that it is indeed possible to obtain a precision similar to that of the regular EBL processes and how to use crosslinking as a high definition tool. The complete process of suspending graphene spin valves is described in section 3.4.5.

2. We argue that the method to fabricate our samples has a beneficial effect on their spin injection properties, as we demonstrate in chapter 6. There, we argue that the overexposure of the PMMA leads to the deposition of a layer of amorphous carbon on top of the graphene sheets, which greatly enhances the spin injection due to a larger contact resistance between cobalt and graphene. It is thus important to gain insight into the detailed nature of our fabrication process.

We performed our preliminary tests as follows: Similar to a dose test in conventional

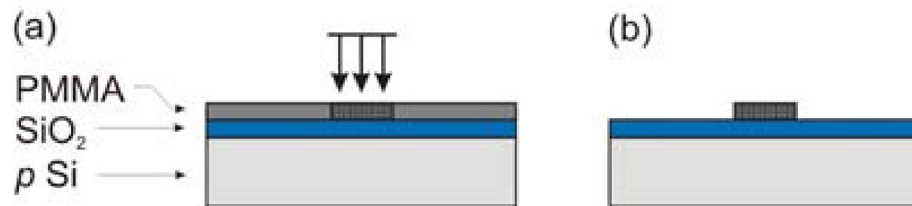


Figure 3.5.: Schematical representation of the fabrication process of crosslinked PMMA structures (a) Overexposure of a layer of PMMA on top of a $Si/SiO_2$-substrate by electron beam (b) Substrate after removal of the remaining PMMA

EBL [82], we overexpose an area of PMMA with a high dose of electron beam radiation first. (Fig. 3.5 (a)). As shown in Fig. 3.5 (b), this results in an area of crosslinked PMMA, while the remaining polymer is removed in acetone. In order to investigate the surface properties of the overexposed PMMA, we performed AFM scans on the test samples. All structures shown here have been written at an acceleration voltage of 30 keV, using an aperture of 20 $\mu$m. However, we have performed the same tests using an aperture of 120 $\mu$m, obtaining consistent results. Like in regular EBL, the differerence between the two apertures is the sharpness of the edges of the defined structures.

## 3.3.2. Choosing the Stepsize

An important property of the writing process by EBL is the stepsize of the scanning electron microscope (SEM). While exposing the polymer, the electron beam (e-beam)

moves across the surface of the substrate in discrete steps. The exposure takes place in square areas, whose sides correspond to the stepsize of the system: The e-beam is moved to the first square, exposes the polymer with the specified dose, and is then moved to the next square. If the stepsize is too large, the crosslinking process does not result in an uniform surface, as shown in Fig. 3.6.

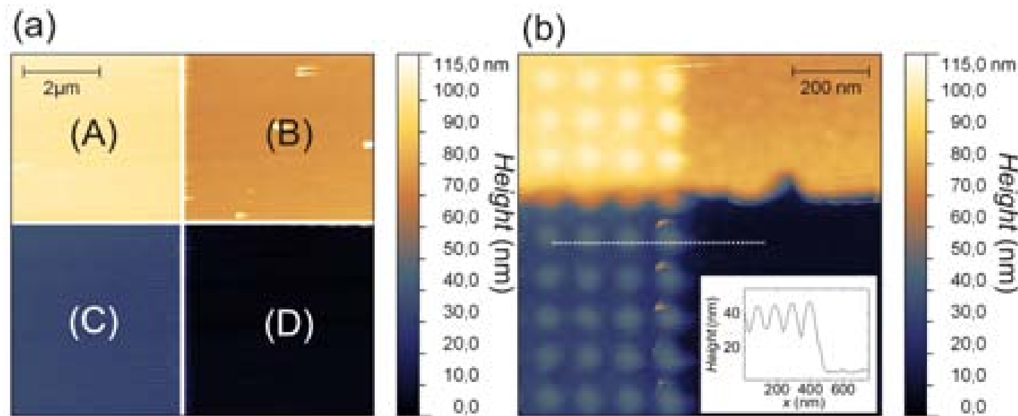


Figure 3.6.: AFM images of a preliminary test sample, consisting of a layer of crosslinked PMMA on top of a $Si/SiO_2$-substrate as well as on top of a metal substrate (a) The areas are (A) crosslinked PMMA on top of metal (B) metal surface without PMMA (C) crosslinked PMMA on top of $Si/SiO_2$ substrate (D) $Si/SiO_2$ substrate (b) AFM scan of the central square of (a) Inset of (b): Height profile along the dashed line in (b) The height of the dots equals ∼45 nm, while in between, the height drops to ∼30 nm

In the figure, we show an AFM scan of a test sample. The horizontal line in the image separates areas of a $Si/SiO_2$ substrate (bottom)from the same substrate covered by metal (top). Likewise, the vertical line separates areas covered by overexposed PMMA (left) as well as without it (right). It can be seen that the PMMA is sticking well on both the Si and the metal substrate.

In Fig. 3.6 (b) we show a second AFM scan of the central cross section in (a). The surface of the crosslinked PMMA exhibits a periodic structure. It consists of dots separated by 100 nm, corresponding to the stepsize used during the EBL of this test sample. A larger amount of PMMA is thus crosslinked in the center of each writing field. In the inset of Fig. 3.6 (b), we show the height profile of the AFM scan along the dashed line in the image. The height of the dots within the PMMA is approx. 45 nm, while the valleys in between exhibit a height of 30 nm.

These results demonstrate that a small stepsize has to be chosen during the EBL in order to obtain an uniform surface of the crosslinked PMMA. For the following work we have used a stepsize of 15 nm, for which the roughness is no longer visible.

### 3.3.3. Choosing the Electron Beam Dose

In order to determine the appropriate dose required to crosslink PMMA, one has to keep in mind that on the one hand, the dose has to be as low as possible in order to minimize the exposure of the graphene flakes during the fabrication process. On the other hand, the dose has to be high enough in order to reliably crosslink the polymer.

Therefore, we have fabricated structures that consist of stripes of $2\,\mu$m width of gradually varying dose. It is convenient to discuss our results in terms of the dose factor instead of the total dose ($dose = area\ dose \times dose\ factor$). The area dose equals $300\,\mu\mathrm{C/cm}^2$ for all structures shown, which is roughly the dose required to expose PMMA as positive resist. Therefore, a dosefactor 30 means that we use 30 times the dose needed for conventional EBL.

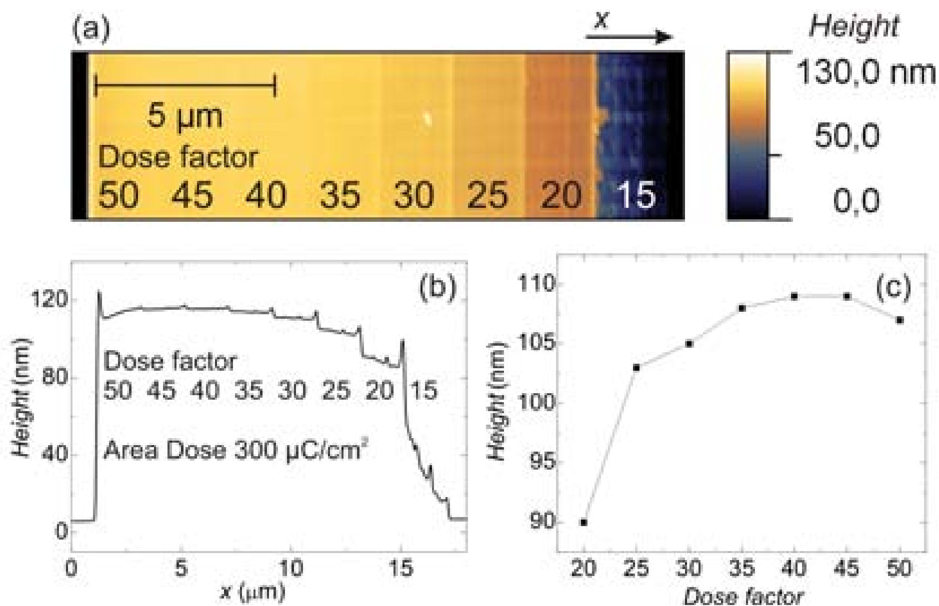


Figure 3.7.: (a) AFM scan of an area of two layers of crosslinked PMMA, with the dose factor varying in steps of five (b) Height profile along the $x$-axis (c) Thickness of the crosslinked polymer as a function of dose factor

In Fig. 3.7 (a), we show an AFM scan of such a structure. An averaged height profile along the $x$-axis is shown in (b).

The height of the profile as a function of dose factor is shown in (c). We can draw the following conclusions from this analysis:

1. **Height as function of dose** The height profile as well as the height of the PMMA as a function of the dose factor (Fig. 3.7 (b) and (c)) indicate that PMMA starts to crosslink at dose factor 15. For higher doses, the height starts to saturate to a value around 110 nm. This result is in good agreement with the

nominal height of the PMMA before overexposure, which is approx. 120 nm [81] for the parameters used here (2 layers of PMMA 950 spincoated at 2500 rpm).

2. **Reduced proximity effect** The height of the crosslinked PMMA drops at a dose factor of 50, as shown in Fig. 3.7 (b) and (c). This is due to the geometry of the structure. All areas receive a certain amount of radiation when the adjacent area is exposed, however for the two outer areas (dose factor 5, not visible, and 50), this effect is reduced, as there is only one adjacent area. The last data point of (c) should hence be disregarded.

3. **Structure of the surface** A rectangular pattern can be distinguished in the AFM image shown in Fig. 3.7 (a). As opposed to the structure discussed in section 3.3.2, the pattern shown here is not due to the stepsize of the SEM, which equals 10 nm for this test, while the pattern here repeats in steps of 0.67 $\mu$m in the $x$-direction.

   The structure is most likely due to the internal processing of the area within the memory of the EBL system. However, the resulting differences in height of the polymer are negligible and the surface is sufficiently even for our purposes.

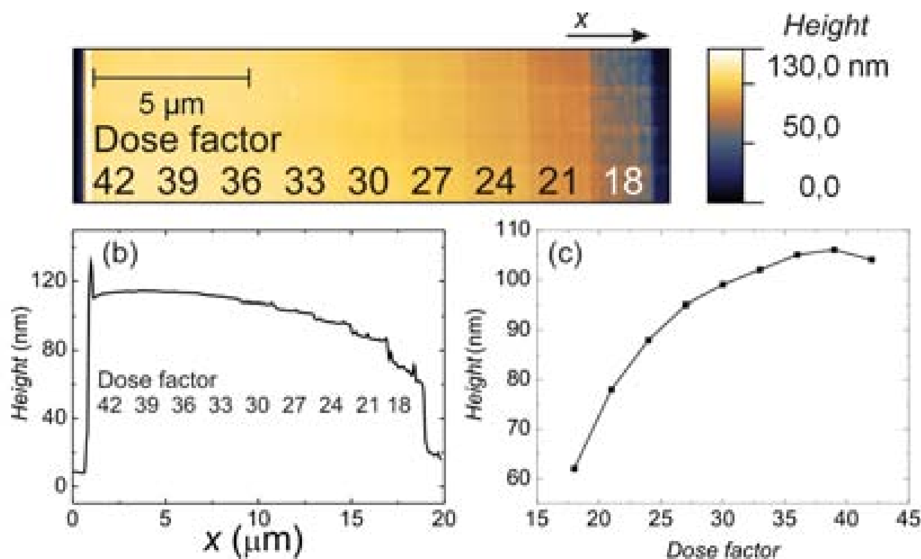


Figure 3.8.: (a) AFM scan of an area of two layers of crosslinked PMMA, with the dose factor varying in steps of three (b) Height profile along the $x$-axis (c) Thickness of the crosslinked polymer as a function of dose factor

These conclusions are confirmed by several test samples. We show a second example in Fig. 3.8. As before, we show an AFM image of the PMMA in Fig. 3.8 (a), a height profile in (b) and the height as a function of the dose factor in (c). In case of the

sample presented here, we increase the dose factor in steps of three. Again, we find that the PMMA starts to crosslink at dose factor 15. At dose factor 18, the PMMA is completely covering the surface of the chip, with a height of approx. 65 nm. At dose factor 30, the height is approx. 100 nm and the surface of the polymer is sufficiently uniform for our purposes.

Based on these results, we choose a dose factor 30 for crosslinking the PMMA, which corresponds to a total dose of 9000 $\mu$C/cm$^2$. We also exploit the dependence of the height of the PMMA in an way which is essential for the fabrication of our thin metallic electrodes, as we show in section 3.3.5.

### 3.3.4. Creating trenches in overexposed PMMA

In order to suspend graphene using crosslinked PMMA, it is necessary to be able to create trenches within the crosslinked areas. Because of the high doses used during the exposure of the polymer, it is natural to assume that the proximity effect plays a major role for the fabrication process, especially for narrow trenches of a few hundreds of nanometers in width. Again, we have fabricated several samples in order to verify the feasibility of our method.

In Fig. 3.9, we show an AFM scan of such an structure. It consists of an area of crosslinked PMMA, where certain areas are not exposed to the e-beam. The width of the these trenches are 2/1/0.8/0.5 $\mu$m. It becomes visible that these areas are free of PMMA after lift-off in acetone.

The height profile, shown in Fig. 3.9 (b), confirms this observation. There are artefacts of the scan visible at the edges of the trenches. However, it is clearly visible that the PMMA is completely removed during lift-off and no polymer remains on the bottom of the trench.

We have found that for smaller widths of the trench, this is not always the case. The proximity effect is more pronounced for trenches smaller than 200 nm, when using two layers of PMMA and for trenches smaller than 300 nm for four layers of PMMA. In these cases, few tens of nanometers remain at the bottom of the trench after lift-off. We can conclude that the proximity effect is more pronounced for multiple layers of PMMA. For less numbers of layers, narrower trenches can be defined.

### 3.3.5. Controlling the Height Profile of the Polymer Substrate

As demonstrated in section 3.3.3, the height of the crosslinked PMMA depends on the dose used during the overexposure. Here, we show that this feature can be used to create smooth edges of the PMMA rectangles, which serve as substrate for graphene. This is important for the fabrication process described in section 3.4 in order to obtain continous FM films. Typically, we use 26 nm thin electrodes, while the height of the crosslinked PMMA is 200 nm. Therefore, it is required that the edges of the PMMA exhibits a smoothly varying height profile.

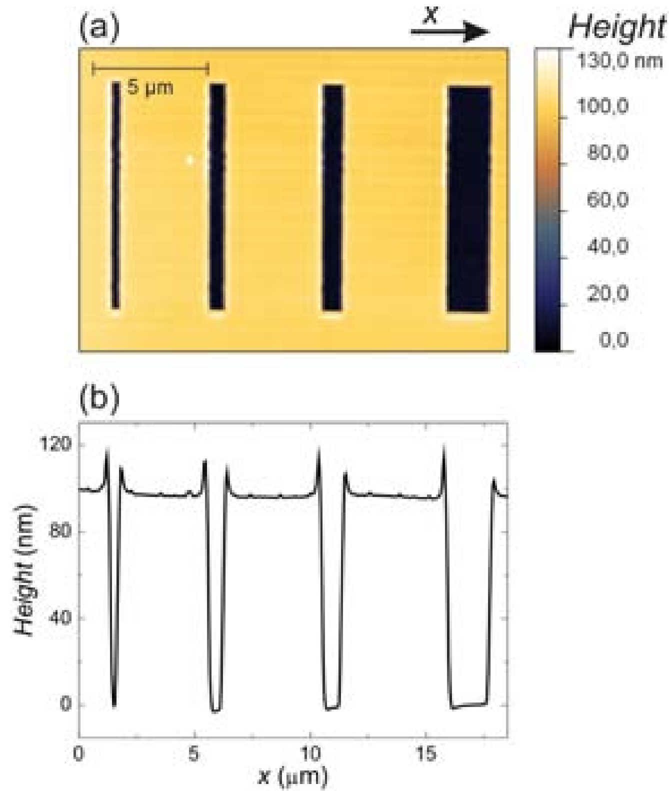


Figure 3.9.: Preliminary test sample for the creation of trenches within crosslinked PMMA (a) AFM scan. Rectangular areas are not exposed during EBL, resulting in trenches after lift-off. (b) Height profile along the dashed line in (a). It can be seen that the trenches created in the PMMA are completely free of polymer

We show a test sample in Fig. 3.10. It consists of a rectangular area of crosslinked PMMA of $10 \times 15\,\mu\text{m}^2$, which are typical dimensions for our devices. An AFM scan is shown in Fig. 3.10 (a). The PMMA in the center of the structure is overexposed with dose factor 30. A height profile along the $x$-direction is shown in 3.10 (b). The height of this structure is 200 nm, as we use 4 layers of PMMA during the fabrication.

In Fig. 3.10 (c), we show a magnified height profile of one of the edges. On this scale it can be seen that the slope of the PMMA is sufficiently low in order to deposit continous metallic electrodes of 26 nm thickness without breaking the contact on the edges. We achieve this by gradually increasing the dose factor in the outer regions of the structure, as shown in Fig. 3.10 (d). Over 50 nm lateral distance we increase the dose factor from 15 to 20 in steps of 1. From dose factor 20 to 30, we increase the dose factor in steps of 2, 3 and 5. As shown in Fig. 3.10 (c), this results in a slope of approx. 200 nm / 500 nm, which is sufficiently low for the deposition of 26 nm of

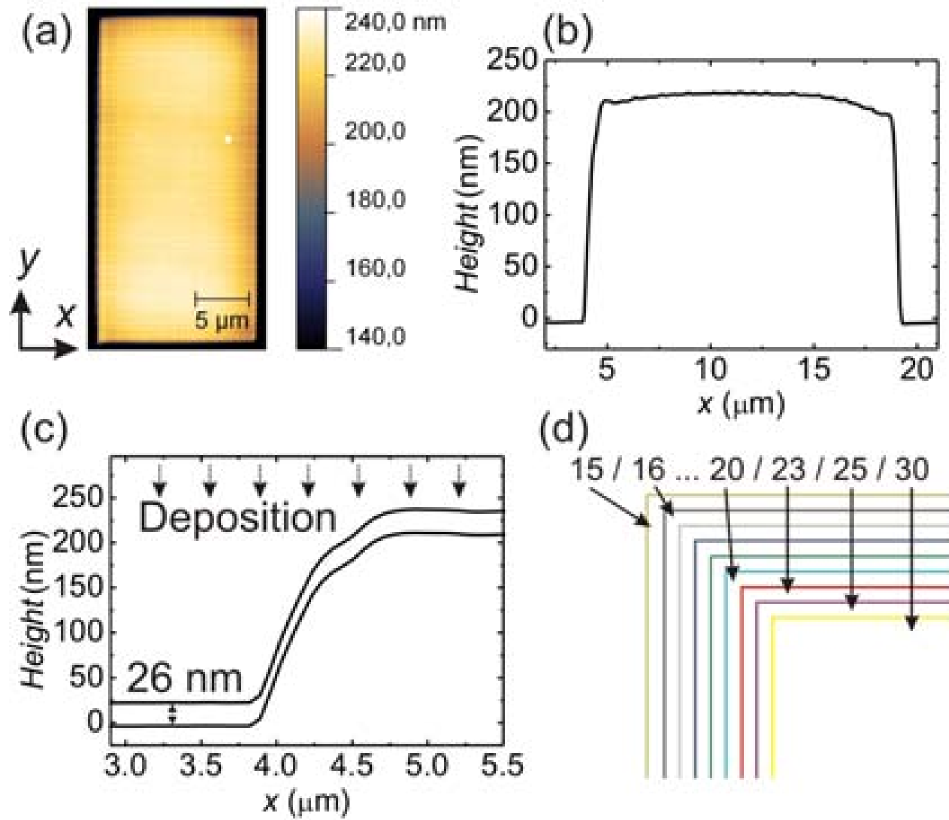


Figure 3.10.: Test for using PMMA as a substrate (a) AFM scan of an $10 \times 15\,\mu$m-area of crosslinked PMMA (b) Height profile along the $x$-axis (c) Graphical representation of deposition process of 26 nm of material on the slopes of the structure (d) Section of the design used for the overexposure indicating the dose factors for an area dose of $300\,\mu\text{C/cm}^2$

metal on top of the 200 nm high polymer.

## 3.4. Fabrication and Engineering of Nanodevices

### 3.4.1. Advantages of Electron Beam Lithography

When exfoliating graphene, the flakes typically exhibit dimensions ranging from the nano- to micrometers. In order to perform electrical transport measurements on these flakes, contacts of similar dimensions have to be fabricated with sufficient precision. The technology used to achieve that is Electron Beam Lithography [82].

EBL is a well established technique since the 1960s. It consists of patterning of a polymer, most commonly PMMA, by a focused beam of electrons. Developing

the polymer leads to the creation of a mask for subsequent deposition of metallic or semiconducting materials. After the removal of the mask, only the material in the previously defined areas remains on the chip.

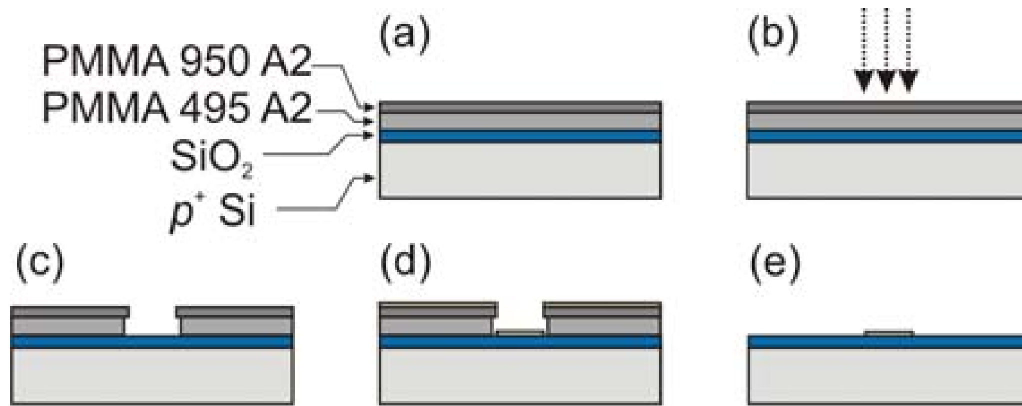


Figure 3.11.: Schematic representation of the standard EBL process (a) $Si/SiO_2$-substrate covered by layers of PMMA 495 and PMMA 950 (b) Exposure of the polymer by e-beam (c) Developing of the chip, resulting in removal of polymer in exposed areas (d) Metal deposition (e) Chip after lift-off

The advantage of EBL over optical lithography methods such as UV-lithograppy are manifold. The use of electrons instead of photons allows for circumventing the diffraction limit of light. Also, while in optical lithography methods structures are created by using predefined mask, in EBL the patterns can be designed and defined easily, making it a very flexible tool.

The limit of EBL is given by the so-called proximity effect: Areas adjacent to the designed ones are exposed by secondary electrons originating from the substrate. This imposes a lower limit for the resolution of EBL defined structures of approx. 20 nm [88].

There are many examples of advances in solid state physics research which have been possible thanks to the use of EBL. One active area is the research on Quantum dots [89], but there are several other fields of nanotechnology which have emerged thanks to the possibilities of EBL.

The development of non local spin valve devices in the nanometer range is another example of how progress in nanolithography methods can lead to progress in research. The original spin valve experiment by Johnson and Silsbee in 1985 was conducted using devices whose dimensions ranked in the micrometer range. The spin injection and detection in a nonmagnetic material had been possible only due to the use of a monocrystalline bulk of aluminium [8].

Downscaling of the non local spin valve devices leads to an increase in the detected voltage, as it is inversily proportional to the volume and thus the width of the ferromagnet. This can be seen from eq. 2.34, $\Delta R_{\mathrm{NL}} \sim 1/A_N = 1/w_N d_N$. For the

experiment performed by Jedema *et al.* in 2001 [11], EBL-defined nanostructures a factor three orders of magnitude smaller than in the Johnson-Silsbee experiment have been utilized, leading to an increase of the signal of three orders of magnitude. This paved the way for electrical spin injection and detection in polycrystalline materials and at room temperature, reviving the interest of the scientific community for the topic.

### 3.4.2. Standard Electron Beam Lithography

In the following, we descibe a common fabrication processes using EBL, schematically shown in Fig. 3.11. It can be divided in the following stages:

1. **Preparation of the chip for EBL** *(Fig. 3.11 (a))* We cut (Si/$SiO_2$) substrates from a wafer into smaller chips and cover it with the photoresist, here PMMA.
2. **Exposure of the polymer by e-beam** *(Fig. 3.11 (b),(c))* In this stage, the polymer is exposed by e-beam in the EBL system, defining the geometry and the structure of the devices to be fabricated. After exposure, we develop the chip in methyl-isobutyl-ketone:isopropanol (MIBK:IPA), removing the exposed PMMA, creating the mask required for the deposition of the material.
3. **Deposition of material** *(Fig. 3.11 (d))* Throughout this stage, the chip is mounted in a system for the deposition of the contact material. There are several possibilities for this, e.g. chemical vapor deposition (CVD), physical vapor deposition (PVD), molecular beam epitaxy (MBE), or thermal or electron beam deposition. Throughout this thesis, we have fabricated all samples by the latter option.
4. **Preparing the samples for measurement** *(Fig. 3.11 (e))* After the deposition of the contact material, we remove the remaining PMMA by acetone and isopropanol.

The basic process described above can be modified in several ways to fabricate more sophisticated devices. An example is shadow evaporation [90, 91], where during step 2, a mask is created exhibiting an undercut. During step 3, material is deposited from different angles, which in combination with the undercut of the mask allows for the fabrication of nanojunction without breaking the vacuum of the deposition system.

### 3.4.3. Graphene spin valve devices

The fabrication process of graphene spin valve devices is shown schematically in Fig. 3.12. We use an EBL process similar to the one described in section 3.4.1, which can be divided into four stages:

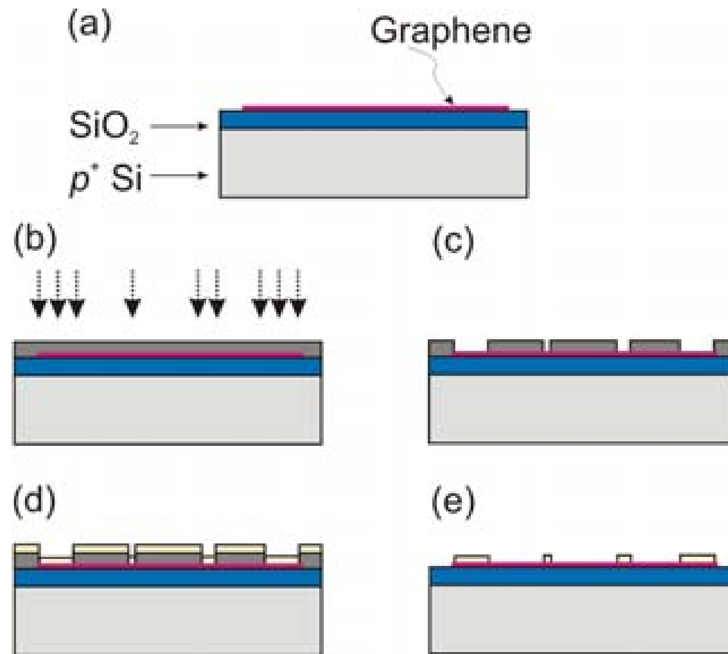


Figure 3.12.: Schematic representaion of the standard EBL proccess for the fabrication of graphene spin valves (a) Graphene is deposited on substrate with markers and localized using an optical microscope (b) Chip covered in PMMA, exposure by e-beam (c) Chip after developing (d) Chip after deposition of (ferromagnetic) contacts (e) Device after lift-off

1. **Exfoliation of graphene on a substrate** *(Fig. 3.12 (a))* Most of the additional work in respect to the standard process, described in section 3.4, falls into this stage. After cutting the substrate ($p^+$ doped Si/*sio*, 440 nm oxide), we define markers in a first EBL step. Afterwards, we exfoliate the graphene onto the substrate and localise suitable flakes with an optical microscope in respect to the markers. Then we design the contacts and cover the chip with PMMA for the next step.

2. **EBL** *(Fig. 3.12 (b),(c))* After carefully aligning the write field of the EBL system, we define the contacts and develop the polymer in MIBK afterwards.

3. **Deposition of material** *(Fig. 3.12 (d))* We deposit 26 nm of Cobalt (Co) for the contacts.

4. **Contacting the device** *(Fig. 3.12 (e))* We carry out the lift-off process.

An example for a device fabricated in this way can be found in Fig. 3.13, showing an optical microscope image (a) and the design of the mask used for EBL (b).

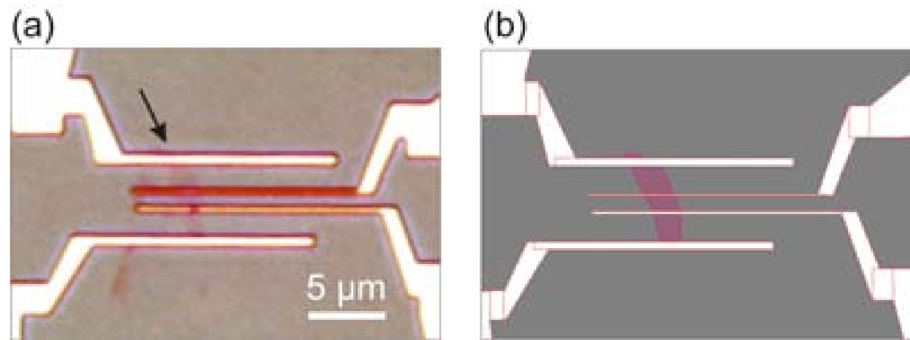


Figure 3.13.: Spin valve device on $SiO_2$ (a) Optical microscope image (b) Design of the sample used for EBL

### 3.4.4. Using Crosslinked PMMA as a substrate

In the following section, we describe the fabrication process for the non local spin valve devices using crosslinked PMMA as a substrate. In respect to the graphene spin valves on Si/$SiO_2$, described in section 3.4.3, we introduce an additional EBL step. The process can thus be divided into the following stages:

1. **Preparation** First, we cut substrates of a wafer of $p^+$ doped Si/$SiO_2$ (oxide thickness 285 nm) and pattern the chips with markers in a preliminary EBL step. Then, we cover the chips with 200 nm of PMMA, exfoliate graphene on top of it and localize the flakes in respect to the markers. As described in section 3.2.2, the optical microscope images are suited to identify SLG.

2. **Crosslinking** In a first EBL step, the PMMA surrounding the graphene is crosslinked in a sufficiently big region. No developing or removal of the remaining PMMA of the first layer is required. We then cover the substrate with a second layer of PMMA.

3. **Second EBL step** During this stage, we define the contacts using a regular dose and develop afterwards.

4. **Deposition of contacts** We deposit 26 nm of Co as contact material.

5. **Contacting the sample** Except for the overexposed polymer, all remaining PMMA is removed during lift-off. Below the graphene however, it remains, constituting an effective substrate for the flake.

PMMA is a hydrophobic material. This is beneficial for the exfoliation of graphene, which is hydrophobic as well. In fact, in order to obtain satisfactory results using the Scotch tape method, it is important to remove water from the ($SiO_2$) substrate, e.g. by oxygen plasma immediately, prior to exfoliation. This is not required for graphene on PMMA. The flakes stick to the PMMA substrate in a notably improved manner.

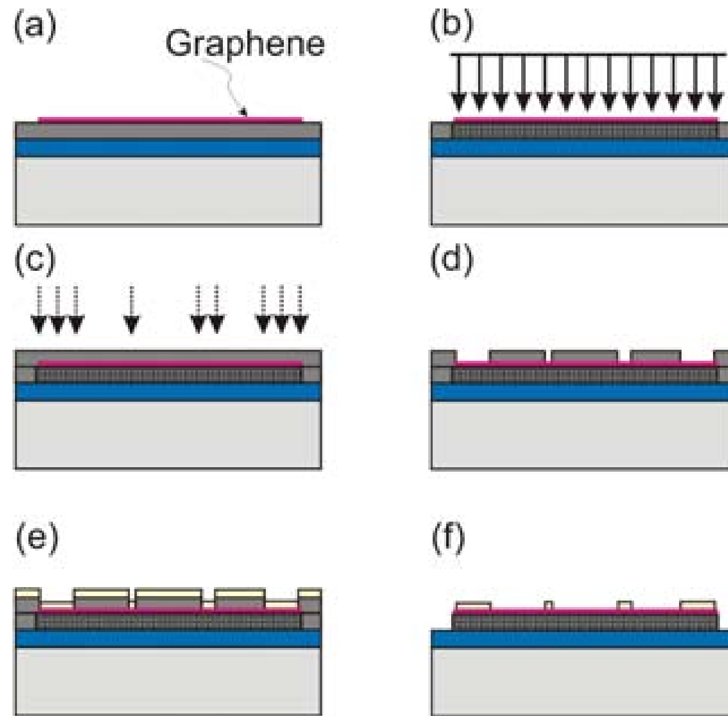


Figure 3.14.: Schematic representation of the EBL process for the fabrication of graphene spin valves using crosslinked PMMA as a substrate. (a) Mechanical exfoliation of graphene on top of a Si/$SiO_2$ substrate covered by a layer of PMMA. (b) Crosslinking of the PMMA layer by overexposure in EBL system (c) Regular exposure of a second layer of PMMA in order to define the contacts (d) Developing of the chip, resulting in removal of PMMA in the contact area (e) Metal deposition (f) Device after lift-off

Measurements and additional material regarding the fabrication process is discussed in chapter 6. Images of a sample are shown in Fig. 3.15.

### 3.4.5. Suspended Graphene Spin Valves

The fabrication process described in section 3.4.4 can be used in a slightly modified way to produce freely suspended graphene samples. Suspending graphene samples has been beneficial for many charge transport studies. Furthermore, it enables cleaning methods such as Argon/Hydrogen cleaning [92] or current annealing [93]. These cleaning methods are essential when trying to obtain ultra-high mobility graphene, and spin relaxation lenghts of several tens of microns have been predicted in such systems [59].

The commonly adapted method for fabricating suspended graphene devices however requires the use of aggresive chemicals. There, devices are fabricated following a common EBL method, as the one described in section 3.4.3, while choosing e.g.

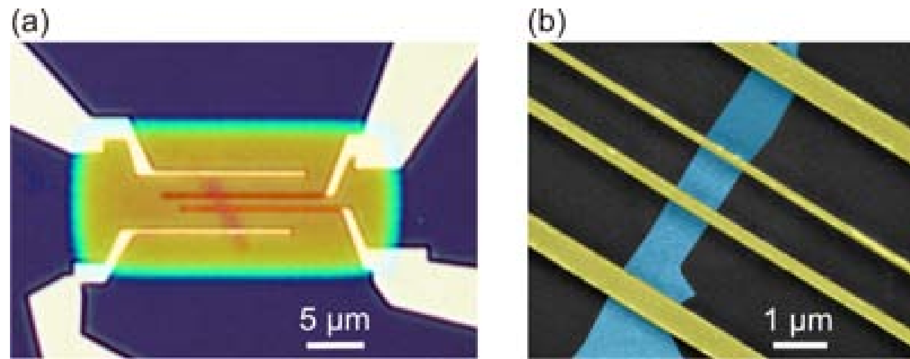


Figure 3.15.: Graphene Spin Valve using PMMA as substrate (a) Optical microscope image of the device. The yellow square is the overexposed substrate, the blue to violet surroundings $SiO_2$. (b) SEM image of the central part of the device. The scale bar is 1 $\mu$m.

chromium and gold as material for the contacts. Then, the $SiO_2$ is etched away using hydrofluoric (HF) acid, except for the areas below the contacts, leaving the graphene sheet suspended. The drawback is that hydrofluoric (HF) acid attacks most materials, including the ferromagnets needed for electrical spin injection. On top of that, as-processed devices often exhibit poor mobilities, making the application of additional cleaning method mandatory.

By using PMMA as additional layer in between the chip and the substrate, we are able to circumvent these limitations. The fabrication process is very similar to to the proces decribed in section 3.4.4 and only differs in step 2:

1. **Preparation** Exfoliation of the graphene on 200 nm of PMMA on top of 285 nm of $SiO_2$. We localize the flakes in respect to the markers and design the contacts as well as the overexposed areas.

2. **First EBL step** We crosslink the PMMA in the area where the contacts are defined during the following step. In contrast to the process described in section 3.4.4, the area in between is not exposed.

3. **Second EBL step** After spinning a second layer of PMMA, we define the contacts using a regular EBL dose. Afterwards, we develop the chip in MIBK.

4. **Deposition of contact material** We deposit 26 nm of Co as contact material.

5. **Lift-off** Lift-off in acetone leads to the suspension of the graphene, as the non-exposed PMMA is removed from below the flake.

Measurements on these kind of samples are presented in chapter 5. SEM images are shown in Fig. 3.17. These images have been taken at an angle between the incident e-

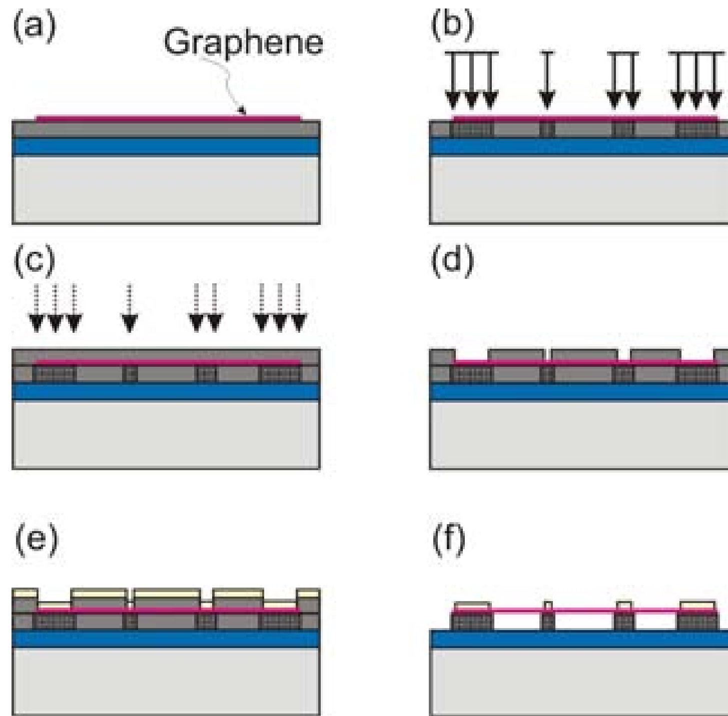


Figure 3.16.: Schematic representaion of the EBL process for the fabrication of suspended graphene spin valves. (a) Exfoliation of graphene on top of a Si/$SiO_2$ substrate covered by a PMMA. (b) Crosslinking of PMMA in areas where contacts are going to be defined (c) Second EBL step to define the contacts within a second layer of PMMA (d) Developing (e) Metal deposition (f) The flake is suspended during lift-off, when the non-exposed PMMA is removed by acetone

beam and the plane of the substrate in order to verify that the graphene is completely suspended, as illustrated clearly in Fig. 3.17 (c) and (d).

## 3.5. Measurement setup

### 3.5.1. Experimental Techniques

In the following, we introduce the experimental techniques used for the measurement of our devices. While electrical connections are equal for all devices, the possibility to tune the carrier concentration of graphene allows for a variety of different measurements. Here, we describe in detail four point measurements, non local spin valve and Hanle measurements.

We conclude the chapter with a summary of the equipment used throughout this

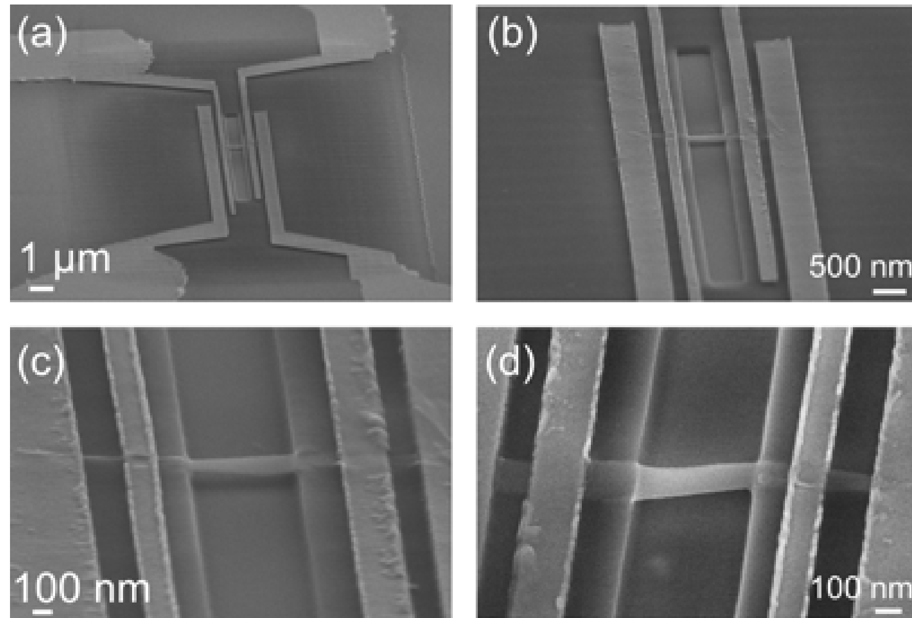


Figure 3.17.: SEM images of a suspended graphene sample (a) - (c): Images of a particular sample taken under an angle of 70° between e-beam and substrate. In (a), the entire area of overexposed PMMA on top of the Si substrate is visible as well as the four electrodes and the suspended graphene flake. In (c), a shadow is visible at the bottom of the trench below the flake, confirming that the flake is completely suspended. (d) Same sample imaged under an angle of 45°

thesis.

### 3.5.2. Four Point Measurements and the Electric Field Effect

The electrical resistance of a device is determined by applying a voltage over it and measuring the current flowing via the device, or vice versa. Throughout this thesis, we have generally used the second option, i.e. applying a bias current and measuring the voltage drop along the device.

A straightforward method in order to achieve that is the two point configuration, where only two contacts are required for the measurement. In this way, not only the resistance of the device under test is measured but the resistance of the wires as well. Since the wires in this case partially consist of small junctions, the wire resistance can be hundreds of Ohm.

The device resistance can be measured directly in four point configuration, as shown in Fig. 3.5.2 (a). Here, the bias current $I$ is applied to the outer two contacts, while the voltage is measured between the inner two contacts.

In order to measure the electric field effect, a voltage is applied between the $p^+$ Si substrate and the ground. As discussed in section 2.8.3, the graphene and the Si act as two plates of a capacitor, with one or several dielectric materials in between them. Sweeping the backgate voltage results in a variation of the numbers of carriers in graphene, as $n = \alpha V_{\mathrm{BG}}$.

Experimentally, this can be demonstrated by fixing a source drain current $I$ and measuring the voltage $V$ across the sample while sweeping $V_{\mathrm{BG}}$. By using $R = V/I$ as well as $\rho = R \times (W/L)$, where $W$ is the width and $L$ the length of the flake between the voltage contacts, it is possible to obtain the resistivity $\rho$ as a function of $V_{\mathrm{BG}}$. we can therefore plot the field effect as shown in Fig. 3.5.2 (b).

These measurements allow for a determination of the mobility of our samples. In case of the example in the figure, the mobility is approx. $4500\,\mathrm{cm}^2\mathrm{V}^{-1}\mathrm{s}^{-1}$ at room temperature.

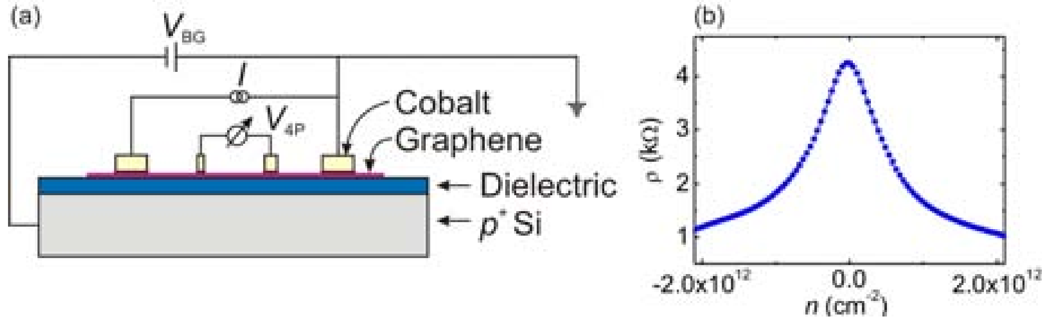


Figure 3.18.: (a) Experimental setup for four point measurement of field effect of graphene (b) Resistivity $\rho_{4P}$ as function of carrier density $n$

### 3.5.3. Non Local Spin Valve Measurements

We have introduced Non Local Spin Valve measurements in section 2.5 from a theoretical point of view. There, we have discussed a system consisting of two ferromagnetic electrodes on top of a non magnetic material.

However, in case of our graphene spin valves at least four electrodes are required in order to perform non local measurements, as shown in Fig. 3.19. Ideally, the outer two contacts of the devices consist of non magnetic materials. This way, we can neglect those contacts and focus only on the spin injection properties of the inner two ferromagnets. However, an additional lithography step is required for that, detrimental to the qualtity of graphene. Therefore, we fabricate our devices with four ferromagnetic electrodes, as shown in section 3.4.

We connect the voltage and the current circuit as shown in Fig. 3.19. Here, the voltage is measured on the left hand side of the device, while the current is applied on

the right hand side. Any detected voltage $V_{\mathrm{NL}}$ is due to spin (or heat currents). Since the charge current does not flow in the voltage circuit, it is called a non local voltage.

Sweeping an in plane magnetic field $B$, parallel to the easy axis of the ferromagnets, results in a subsequent switching of the magnetization of the electrodes and a change in the detected voltage $V_{\mathrm{NL}}$. Conventionally, this type of measurement is graphically displayed in terms of transresistance $R_{\mathrm{NL}} = V_{\mathrm{NL}}/I$ as a function of the magnetic field, as shown in Fig. 2.8.

In graphene, unlike metals, the backgate voltage $V_{\mathrm{BG}}$ allows for the measurement of NLSV at different mobilities respectively carriers densities of the graphene. This allows for a variety of measurements, which are not possible in all metallic spin valve.

It is possible to prepare the parallel as well as the anti parallel alignment of the electrodes at zero field. This is due to the hysteresis of the ferromagnets [94]. Therefore, one can measure the non local voltage for the parallel configuration as a function of $V_{\mathrm{NL}}$ and then repeat the same for the antiparallel configuration. The difference between these measurements is $\Delta V_{\mathrm{NL}}$ as a function of the backgate voltage $V_{\mathrm{BG}}$.

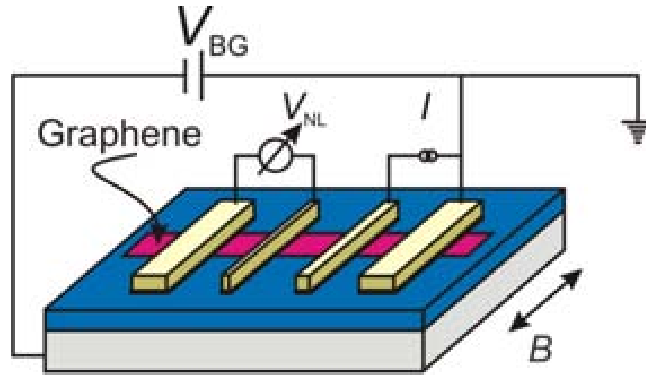


Figure 3.19.: Schematical representation of the electrical connections for non local spin valve measurements

We also use this technique to measure non local $IV$ curves of our devices as a function of the gate voltage $V_{\mathrm{BG}}$. We prepare the parallel alignment of the magnetizations of the ferromagnets, then we measure the non local voltage as a function of $I$. Repeating the measurement for the anti parallel alignment and for varying values of $V_{\mathrm{BG}}$ allows us to obtain the bias dependence of the non local signal at any given gate voltage, or the dependence of the non local voltage as a function of $V_{\mathrm{BG}}$ at any given current. We confirmed the validity of this approach by performing conventional spin valve measurements for different values of $I$ and $V_{\mathrm{BG}}$. The results are discussed in chapter 7.

### 3.5.4. Hanle Measurements

In contrast to NLSV, Hanle spin precession is measured in a perpendicular magnetic field, as shown in Fig 3.20. Prior to the measurement, we prepare the P or AP alignments of the ferromagnets using an in plane magnetic field, as in Fig. 3.20. Afterwards, either the plane of the substrate is rotated 90 degrees in repect to the magnetic field. Then, $V_{\mathrm{NL}}$ is measured as a function of the magnetic field.

As described in section 2.6, these measurements allow for the extraction of the spin relaxation length in a single device. Repeating the Hanle measurements as a function of the backgate voltage hence delivers the spin relaxation length as a function of the carrier density of the graphene.

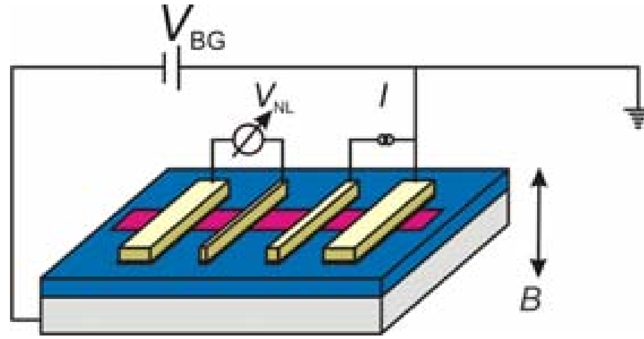


Figure 3.20.: Schematical representation of the electrical connections for Hanle spin precession measurements

### 3.5.5. Equipment

The equipment and material used for the fabrication of samples as well as for measuring them is summarized in the following.
The HOPG we use for the fabrication of flakes originates from two different providers, NGS Naturgraphit and Covalent Materials Corporation. The main difference between the two types of graphite is the ease of handling, while we find no notable difference in the electronic properties of the final devices.
The optical microscope images are taken with a Nikon Eclipse LV100 under normal incidence with a 100x objective (numerical aperture 0.9) in combination with a digital camera, a Nikon Digital sight DS-Fi1. The absorption profile are read out on the image processing software, NIS Elements F 3.0.
The Raman spectra are recorded at room temperature with the generous help of Dr. Françesc Alzina, using a Horiba T64000 spectrometer operated in single mode configuration with a spectral resolution of $4\,\mathrm{cm}^{-1}$.
All AFM scans are carried out using a Nanoscope IIIa by digital instruments in tapping mode using tips of a diameter of 10 nm or less.

The EBL system used for the fabrication of the samples consists of an SEM module by Carl Zeiss together with a EBL module by Raith GmbH, a Raith 150-Two. The accelerating voltage for all EBL processes is 30 keV, using apertures of either 20 or 120 $\mu$m. The background pressure of the chamber is approx. $1 \times 10^{-6}$ mbar. The SEM images are taken at lower acceleration voltages between 2 and 10 keV either with the Raith or in a Quanta FEI.
We carry out the deposition of the metal contacts in a electron beam evaporator by *AJA International* at a base pressure of approx. $1 \times 10^{-7}$ Torr. At an accelerating voltage of 8 keV, it requires approx. 50 mA in order to evaporate cobalt, used as material for the contacts.
The electrical connections to the sample are achieved by wirebonding 25 $\mu$m thin aluminium wires to the contact pads of the devices, using a wirebonder by Westbond.
Electrical measurement are carried out in a continous flow cryostat by Janis systems. The magnetic field is applied using either a Lakeshore magnet with a maximum field of 1 T, or a GMW magnet with a maximum field of 180 mT. The current applied to the sample is given by a current source K6221 by Keithley instruments. The voltages are read out by a nanovoltmeter by Keithley, a K2182, which operates together with the current source in delta mode. Alternatively, DC measurement were carried out using the K6221 as current source, while reading out the voltage using an Agilent 34410 multimeter.
Finally, the backgate voltages are applied by using either a Keithley 2400 Current/Voltage source or a Keithley 230 voltage source.

# 4. On the Theory of Spin Dependent Tunneling

## 4.1. Introduction

Throughout this chapter, we analyze in detail the tunneling process of electrons between ferromagnetic and nonmagnetic electrodes based on an elementary model system. Especially, we discuss the bias dependence of this system, introducing basic concepts which are important for the understanding of spin dependent transport.

The tunneling process of particles via a barrier, whose energy is larger than that of the particle itself, is one of the textbook examples of quantum mechanics (see e.g. [95, 96]). As such, it has repeatedly attracted the attention of the scientific community. For instance, the transmission of conduction electrons from one metal into another via an insulating layer can be understood as a resonant tunneling process and has attracted considerable attention in the 1960s [97, 98, 99, 100].

If additionally one of the electrodes in such a junction is ferromagnetic, then the tunneling process is spin dependent and the tunneling current spin polarized. Given the elementary nature of the process, it is surprising to find that important properties of spin-dependent tunneling (SDT) are not understood to the current day.

Interest in the topic of SDT was raised by a series of seminal experiments by Meservey and Tedrow [1, 2]. They studied tunneling in FM/I/SC junctions, where I stands for an insulator and SC for an superconductor. In a large magnetic field, the density of states of the SC is Zeeman splitted. This allowed for a determination of the spin polarization of a variety of $3d$ ferromagnets for I = $Al_2O_3$ by measuring the bias dependence of such a junction. It became immediately obvious that the experimental results did not agree with theoretical predictions of the process, which were solely based on the DOS of the FMs at the Fermi level. These predictions did not provide neither the correct magnitude of the spin polarization nor its sign.

As a solution, Stearns proposed that only itinerant electrons contribute to the tunneling process, requiring to take into account the specific band structure of the $3d$-transition metals: Dispersive $s$-bands are hybridized with more localized $d$-bands [101]. Although these $d$-bands have a strong weight at the Fermi energy, Stearns argumented that due to the different effective masses, the transport will be dominated by the nearly free $s$-electrons.

As soon as a fabrication technique for pinhole free $Al_2O_3$ tunnel barriers became

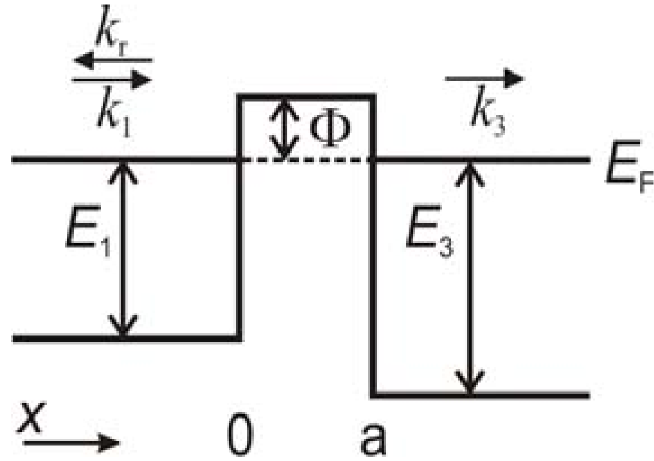


Figure 4.1.: Schematic energy diagram of the simple model

available [102], a plethora of experiments followed in magnetic tunnel junctions (MTJs), which consist of FM/I/FM trilayers. Here, the Zeeman split SC is replaced as a detector by a second, exchange split FM, allowing for spin polarization experiments in a much more ample range of parameters. Especially, the maximum voltage bias in the Meservey/Tedrow experiments is of the order of the superconducting gap of approx. 1 mV. In case of MTJ it is only limited by the break through voltage of the tunnel barrier, which can surpass values of 1 V.

Many experiments in MTJs focussed on the search of FM/I combinations, which provide large values of TMR, valuable for magnetic field sensors. However, different signs of TMR can be demonstrated in systems using the same ferromagnetic materials as electrodes, but tunneling barriers of different materials [103]. This demonstrates in a most evident way that a comprehensive theory of the subject requires not only to take into account the band structure of the electrodes, but also the electronic structure of the insulator together with the symmetry of all the bands involved. Consequently, it is associated with a considerable amount of numerical computations [104, 105]. While first-principle calculations are applicable to epitaxial systems [106, 107, 108] it is an extremely sophisticated task to calculate the electronic structure of an amorphous barrier such as $Al_2O_3$.

Thus, while significant progress has been made in the investigation of spin resolved tunneling, many open questions remain. For instance, there is no consensus on the explanation of the usually strong bias voltage dependence of TMR (see e.g. [109]). TMR is systematically observed to decrease at large bias voltages, dropping to about half its zero bias value or less, when the bias is approx. half a volt. Not only does this affect possible applications of TMR, but it is also intriguing from a fundamental point of view.

Measurements based on MTJs are intrinsically difficult to interpret, as they involve

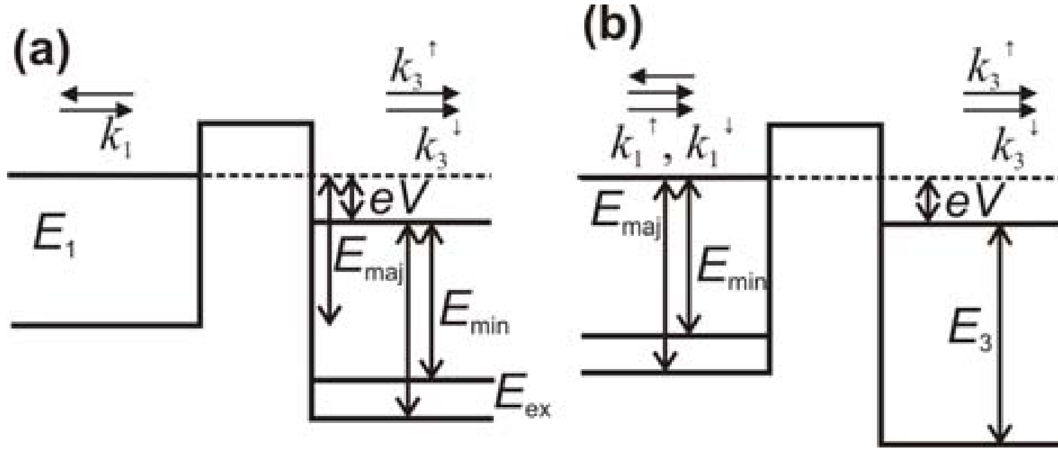


Figure 4.2.: (a) Tunneling from NM into FM and (b) from FM into NM

electrons tunneling out of one ferrromagnetic electrode into another one, and spin polarizations of both electrode participate in a non trivial way. As a consequence, alternative experimental and theoretical methods are required in order to study the effects of the ferromagnetic electrodes separately. This possibility is given in non local spin valve structures (see section 2.5). Here, SDT can be studied by directly measuring the polarization of the single FM/I interface, as in the Meservey/Tedrow technique, while avoiding the experimental limitations imposed by the superconducting detector.

The data obtained with such devices show a strong asymmetry about zero bias [94], which we analyze with a theoretical approach based on an analytical free-electron model. The model uses a minimum of elements that should be present in any coherent tunneling event. Despite its simplicity, our model qualitatively explains the experimental observations.

## 4.2. Free Electron Tunneling

In order to describe the process, we make on the following assumptions:

1. Our model is based on an analytical solution of the stationary, one-dimensional Schrödinger equation using a rectangular shaped potential. The potential characterizes the insulating layer, while the electrons in the metal electrodes are seen as free particles. Our simple one electron picture can be extended by using the density of states for free electrons and by including a bias dependence of the barrier shape.

2. The magnetic materials are supposed to act as perfect Stoner FMs, which means that there are different bands for majority and minority spin that are characterized by different wave numbers.

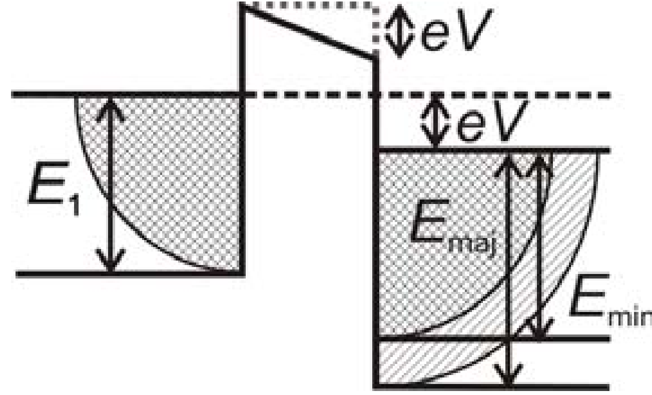


Figure 4.3.: Schematic representation of the extended model

3. We use the two-current model of Mott [37], stating that the electric conductivity of a magnetic material consist of a sum of the conductivities of spin up respectively spin down electrons, $\sigma^{\mathrm{NM}} = \sigma_\uparrow + \sigma_\downarrow$. This implies that spin flips during the tunneling process are neglected.

The Stoner model of ferromagnetism and the two-current model are discussed in more detail in chapter 2.

It is convenient to first derive a general expression for the tunneling probability of a single electron without regarding spin, only depending on the energy before and after tunneling as well as on the work function of the barrier. A more detailed derivation of this exercise can be found in [96]. Then, it is straightforward to obtain the different probabilities for spin up and spin down by considering the specific $E_{\mathrm{maj}}$ and $E_{\mathrm{min}}$ and the overall current by summing up the two independent spin contributions.

The potential landscape is depicted in Fig. 4.1. The electrons in regions 1 and 3 are characterized solely by their energies $E_1$ respectively $E_3$, the potential barrier by its width $a$ and its work function $\Phi = V - E_1$. The transmission probability $T$ is defined as the ratio of the incident to transmitted current density and is obtained by solving the 1D, time independent Schrödinger equation. The solutions have the general form $\psi_j = a_j e^{-ik_j x} + b_j e^{ik_j x}$ for $j = 1, 3$ and $\psi_2 = a_2 e^{-k_2 x} + b_2 e^{k_2 x}$ in region two. Here, the wave vectors $k_j$ are defined by $E_{1,3} = \hbar^2 k_{1,3}^2/2m$ in region 1 and 3 and by $\Phi = \hbar^2 k_2^2/2m$ in region two.

Now, we use the boundary conditions at the interfaces between metal and insulator at $x = 0$ and $x = a$. Additionaly, we take into account that $b_3 = 0$, since we consider particles coming in from the left, thus only transmitted waves exist in region 3, on the right hand side of the barrier. Solving the resulting linear system of equations we obtain for the transmission probability $T$

$$T = \frac{4k_1 k_2}{(k_1^2 + k_2^2)} \frac{4k_2 k_3}{(k_3^2 + k_2^2)} e^{-2k_2 a} \tag{4.1}$$

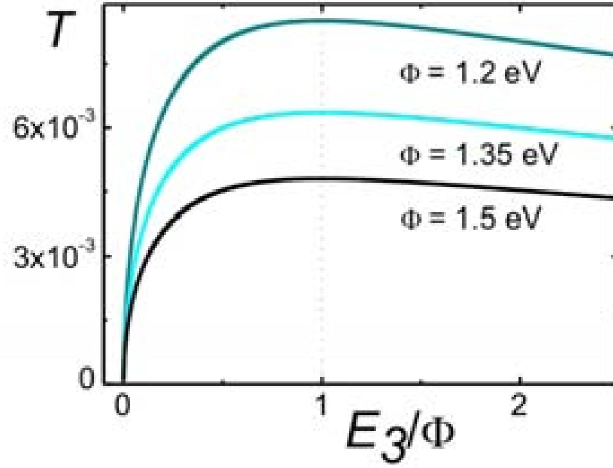


Figure 4.4.: Transmission probability as a function of $E_3/\phi$, exhibiting a peak at $E_3/\phi = 1$

Here, we have used $e^{-2k_2 a} \ll 1$, as we treat the weak transmission limit, which is reasonable for $\Phi$ of the order of an electronvolt and a barrier thickness $a$ in the nanometer range.

It is straightforward to extend our results to a system where one of the electrodes is ferromagnetic by using assumptions 2 and 3. Tunneling from NM to FM is shown schematically in Fig. 4.2 (a), and tunneling from a FM into NM in Fig. 4.2 (b). Here, an additional bias voltage $V$ is introduced. The bottom of the bands of the FMs are shifted by the exchange interaction $E_{\text{ex}}$ for majority (up) and minority (down) spin.

For tunneling of electrons from NM to FM, the energies read $E_1^{\uparrow,\downarrow} = E_{\text{maj,min}} + eV$ and $E_3^{\uparrow,\downarrow} = E_3$ while for tunneling from FM to NM, $E_1^{\uparrow,\downarrow} = E_{\text{maj,min}}$ and $E_3^{\uparrow,\downarrow} = E_3 + eV$. With the corresponding wave number $k$, the transmission probabilities for spin up and spin down in each case can be obtained from eq. 4.1. The total transmission is given by $T = T^{\uparrow} + T^{\downarrow}$.

Now, we can study the bias dependence of the polarization of the transmitted tunneling current. It is defined as

$$P = \frac{j_3^{\uparrow} - j_3^{\downarrow}}{j_3^{\uparrow} + j_3^{\downarrow}} \tag{4.2}$$

Here, $j_3^{\uparrow,\downarrow}$ are the current densities on the right hand side of the barrier. With the transmission coefficient $t$ of the barrier, these current densities are given by

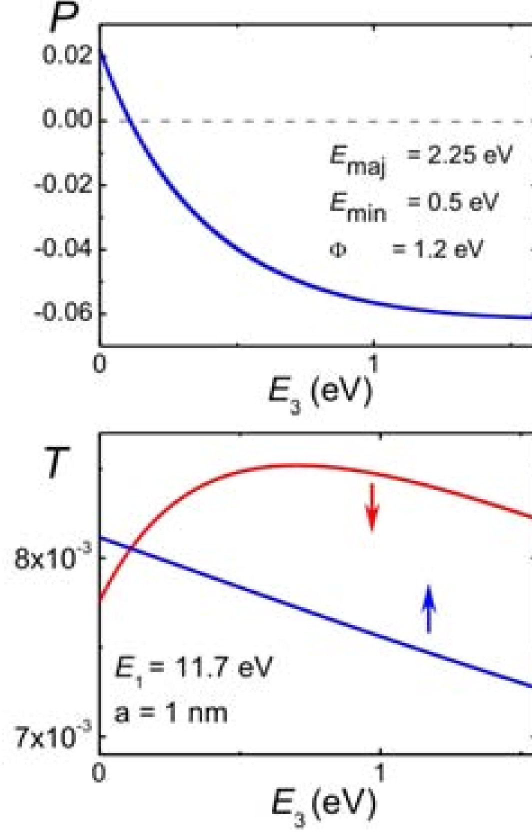


Figure 4.5.: (a) Polarization of the Current and (b) $T^{\uparrow}$ and $T^{\downarrow}$ as a function of $E_3$

$j_3^{\uparrow,\downarrow} = -(e\hbar k_3^{\uparrow,\downarrow}/m)\ \left|t^{\uparrow,\downarrow}\right|^2$. Therefore, the polarization $P$ can be written as

$$
\begin{aligned}
P &= \left(\frac{k^{\uparrow}}{{k^{\uparrow}}^2+k_2^2}-\frac{k^{\downarrow}}{{k^{\downarrow}}^2+k_2^2}\right)\Big/\left(\frac{k^{\uparrow}}{{k^{\uparrow}}^2+k_2^2}+\frac{k^{\downarrow}}{{k^{\downarrow}}^2+k_2^2}\right)\\
&= \left(\frac{\sqrt{E^{\uparrow}}}{E^{\uparrow}+\Phi}-\frac{\sqrt{E^{\downarrow}}}{E^{\downarrow}+\Phi}\right)\Big/\left(\frac{\sqrt{E^{\uparrow}}}{E^{\uparrow}+\Phi}+\frac{\sqrt{E^{\downarrow}}}{E^{\downarrow}+\Phi}\right)
\end{aligned}
\tag{4.3}
$$

where we distinguish between two different cases: When tunneling out of NM into FM, $k^{\uparrow,\downarrow} = k_3^{\uparrow,\downarrow}$, while in the case of tunneling from FM to NM, $k^{\uparrow,\downarrow} = k_1^{\uparrow,\downarrow}$. In the former case, $k^{\uparrow,\downarrow}$ depends on the bias $V$, but not in the latter one. Moreover, the polarization of the tunneling of electrons is different from the polarization of the electrons of the Fermi level of the FM, which in a free electron model is given by $P_{\mathrm{FM}} = (k^{\uparrow} - k^{\downarrow})/(k^{\uparrow} + k^{\downarrow})$.

Finally, we extend our model by taking into account two additional features. First, we include the DOS of free electrons in eq. 4.3, which consists of a factor $D(E_i) = k_i$ in equation $P$. Second, it is known that applying a bias voltage across a tunneling

barrier alters the shape of its potential. Here, we follow a method developed by Holm [97] and Simmons [98], which consist of approximating the tunneling barrier by its average height. Assuming a uniform voltage drop, the shape of the barrier is trapezoidal, meaning that it can be approximated by a rectangular barrier lowered by a factor $-\frac{e}{2}V$ with respect to the undisturbed height. In our derivation we therefore substitute $\Phi \mapsto \Phi_0 - \frac{e}{2}V$. Since $k_2 \propto \sqrt{\Phi}$, this means that the polarization $P$, given by eq. 4.3, is affected by the substitution as well. Both extensions of the model are schematically shown in Fig. 4.3.

## 4.3. Discussion

In the following, we discuss the polarization of the current as predicted by our simple model. Furthermore, we compare this prediction with those obtained from more elaborated models.

First, we focus on the change of sign of $P$ that has been observed experimentally [94]. It can be understood by considering the transmission probability $T$ given by Eq. 4.1 in the case of electrons tunneling out of NM into FM. In Fig. 4.4, we plot $T$ as a function of $E_3/\Phi$. It becomes visible that the transmission reaches a peak whenever the wavevector of the transmitted wave matches that of the evanescent one [94], $E_3 = \Phi$. Here, $E_3^{\uparrow,\downarrow} = E_{maj,min} + eV$. This means that the transmission for the spin up and down channel, respectively, peaks at $V_{\mathrm{maj,min}}^{\mathrm{max}} = (\Phi - E_{\mathrm{maj,min}})/e$.

Together with the exchange splitting of the spin subbands, this leads to the change of sign in the polarization $P$. As the bottom of the two spin subbands are shifted by $E_{\mathrm{ex}}$, the transmission probability for spin up and down reaches its maximum at different bias voltages.

An example is shown in Fig. 4.5, where we have simulated the tunneling of electrons from Aluminium into Permalloy via a tunneling barrier of 1 nm thickness and 1.2 eV potential height. The polarization $P$ of the current as given by eq. 4.3 is shown in Fig. 4.5 (a), while the transmission probabilities $T^{\uparrow,\downarrow}$ for the majority and minority bands are shown as a function of $E_3$ in Fig. 4.5 (b). For majority spin, $E_3^{\uparrow} = 2.25\,\mathrm{eV} + eV$, while for minority spin, $E_3^{\downarrow} = 0.5\,\mathrm{eV} + eV$.

At zero bias voltage, the transmission probability for the majority spin type is higher than that of the minority. For spin up, it is given by $T^{\uparrow} = T(2.25\,\mathrm{eV})$, while for spin down $T^{\downarrow} = T(0.5\,\mathrm{eV})$. However, with increasing bias, $T^{\uparrow}$ continually decreases, while $T^{\downarrow}$ increases with increasing bias (until it peaks at 0.7 eV, so that $E_3^{\downarrow} = \Phi$). At approximately 0.11 eV, the transmission probabilities for both channels are equal and for higher bias voltages, $T^{\uparrow} < T^{\downarrow}$, leading to the change in sign in $P$.

Despite the simplicity of our approach, we are thus able to qualitatively explain this feature with our model, which is only based on elementary concepts of quantum mechanics. This shows that the bias dependence of the polarization of the current in these systems cannot be understood in a straightforward way, as it exhibits a rather

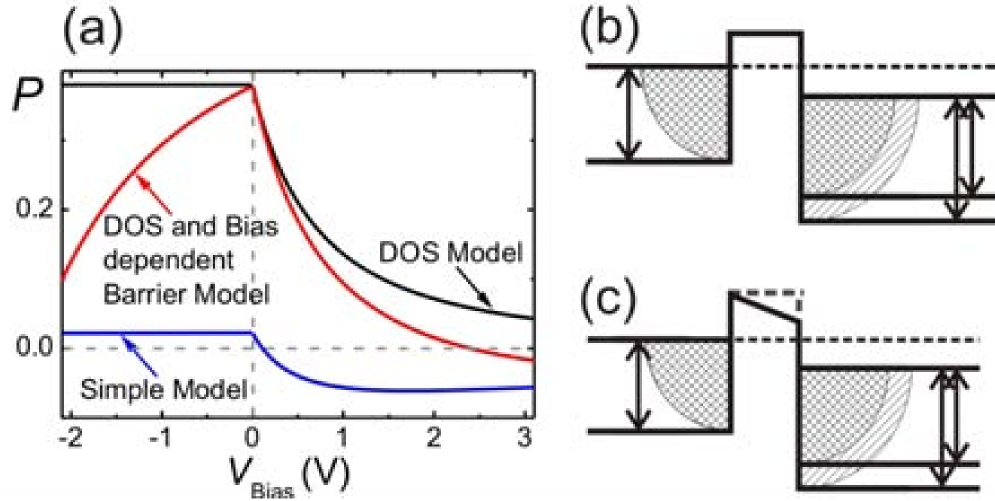


Figure 4.6.: (a) Comparision of $P$ as predicted by the different model (b) Schematic representation of the model including DOS and (c) including DOS and bias dependent potential barrier

unintuitive behavior.

However, the simple model fails to capture the dependence of $P$ on the bias voltage $V$ for electrons tunneling from FM into NM.

In the following, we show that the extended versions of the model deliver a more accurate prediction of $P$. In Fig. 4.6 we compare the different versions of $P$, where we use the same values for $E_{maj}$, $E_{min}$ and $\Phi_0$ as above. It can be seen that taking into account the DOS of the electrons leads to a value of approx. 38 % at zero bias for the calculated polarization, which is close to the experimentally observed one [94]. However, a decaying spin polarization for negative values of $V$, i.e. for tunneling of electrons from NM into FM, can only be predicted by considering the deformation of the shape of the barrier due to the applied bias voltage. The same conclusion has been drawn in case of SDT between FMs and semiconductors across a Schottky barrier [110].

Thus, by extending our model with a modulated shape of the potential barrier, we qualitatively explain the tunneling process from ferro- into nonmagnetic electrode as well. One might assume that the only missing ingredient to a full description of the system would be finding the appropriate shape of the potential barrier. Unfortunately, the realistic shape of such potential barriers is poorly known and it has been pointed out[111] that such a model is very sensitive to the shape of the potential barrier.

## 4.4. Conclusion

Throughout this chapter, we have developed a simple one electron model of spin dependent tunneling in FM/I/NM junctions, based on an analytical solution of the Schrödinger equation. We have focussed on the bias dependence of the polarization of the current passing through these junctions. The predictions are in agreement with experimental data, exhibiting a change of sign when tunneling takes place from nonmagnetic into ferromagnetic material. Our approach may serve as a first approximation of the process, although it is clear that a comprehensive description has to incorporate a variety of data, such as the band structure of both the electrodes and the insulator.

Our simple model is thus unable to render all of the complexity inherent to non-ideal interfaces, scattering or complex band structures. However, it qualitatively explains the experimental observations and shows that complex behavior of the polarization as a function of the bias voltage is intrinsic to tunneling and is highly sensitive to the ratio between the electron wave numbers inside and outside of the barrier region.

# 5. Electrical Detection of Spin Precession in freely-suspended Graphene Spin Valves

## 5.1. Introduction

In this chapter, we present measurements on freely-suspended graphene spin valves [68]. We achieve electrical spin injection and detection using cobalt electrodes and a non local spin valve geometry. The devies are fabricated with a single electron beam resist process, minimizing both the fabrication steps and the number of aggressive chemicals used, greatly reducing contamination and increasing the yield of high-quality, mechanically stable devices. As-grown devices can present mobilities exceeding $10^4\,\mathrm{cm}^2\,\mathrm{V}^{-1}\mathrm{s}^{-1}$ at room temperature and, because the contacts deposited on graphene are only exposed to acetone and isopropanol, the method is compatible with almost any contacting material. We study spin accumulation and spin precession in our non local spin valves. Fitting of Hanle spin precession data in bilayer and multilayer graphene yields a spin relaxation time of 125-250 ps and a spin diffusion length of $1.7 - 1.9\,\mu$m at room temperature.

## 5.2. Spin Injection in Graphene

Graphene and few layer graphene (FLG) and related materials are very promising for nanoelectronics [21, 112, 113] and are considered ideal candidates to transport spin information in future spintronic devices [58, 59, 114]. Long spin lifetimes $\tau_{\mathrm{sf}}$ and relaxation lengths $\lambda_{\mathrm{sf}}$ can be expected due to small intrinsic spin-orbit coupling and the lack of hyperfine interaction with the predominant carbon nuclei $^{12}$C, which has no spin [58, 59, 114]. However, although predictions indicate that $\lambda_{\mathrm{sf}}$ should exceed tenths or even hundredths of micrometers [58, 59], the largest reported value to date is $\lambda_{\mathrm{sf}} \sim 5\,\mu$m for bilayer graphene (BLG) [67]. These results are observed using tunneling contacts at low temperatures (20 K), where relatively long $\tau_{\mathrm{sf}} \sim 6$ ns have been measured. At room temperatures, $\tau_{\mathrm{sf}}$ usually drops to a few hundred picoseconds and is in the nanosecond range only in samples with very low mobility ($\mu = 300\,\mathrm{cm}^2\mathrm{V}^{-1}\mathrm{s}^{-1}$ in Ref. [115]). For single layer graphene (SLG), the results are

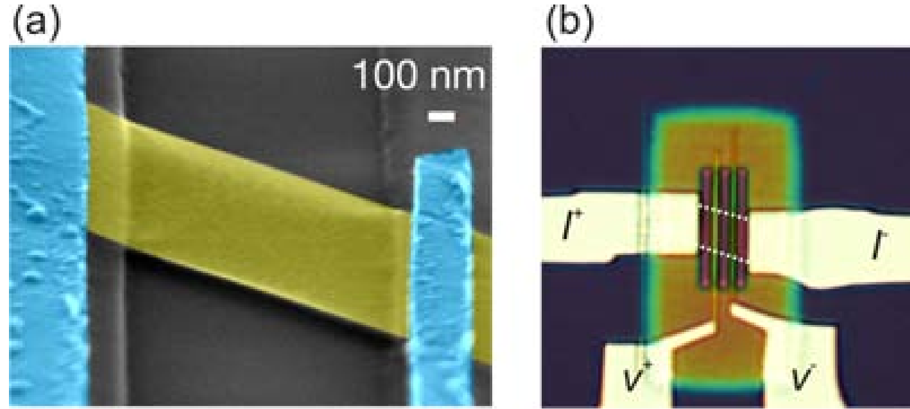


Figure 5.1.: (a) SEM image of the a suspended graphene flake between two ferromagnetic electrodes (b) Optical microscope image of SLG, indicated by dashed lines, over three trenches in the PMMA, with electrical connections for four point measurements

even more discouraging and state-of-the art devices show $\lambda_{sf} < 3\,\mu$m and $\tau_{sf} < 1$ ns at 10 K [55, 67, 116].

The reasons for the discrepancy between theory and experiment have yet to be clarified. Most experiments are carried out in graphene with relatively low $\mu$ in the range of $500 - 2000\,\mathrm{cm^2V^{-1}s^{-1}}$, where the spin relaxation process has been ascribed to the Elliot-Yafet mechanism [65]. A simple extrapolation to $\mu = 2 \times 10^5\,\mathrm{cm^2\,V^{-1}s^{-1}}$, assuming that the Elliot-Yafet mechanism is still valid, results in $\lambda_{sf} \sim 100\,\mu$m [65], which is very promising for applications and close to the predictions. However, reports [66] on graphene decorated with gold are at odds with this notion. Therefore, it has been suggested that the spin relaxation could result from a combination of Elliot-Yafet and Dyakonov-Perel processes [58, 59, 117], a point we discuss further in section 2.9.

The interaction between graphene and the substrate, usually $SiO_2$, has been identified as one of the reasons for the low mobilities of spintronic graphene devices [118]. The substrate contributes charged impurities that increase the scattering of carriers and creates puddles of holes and electrons that reduce the mobility [119]. It could also result in small locally-strained regions where spin-orbit interaction is enhanced [58, 59]. The effects of the substrate have been recognized in early charge transport studies, leading to the fabrication of freely-suspended graphene devices [118, 120], which, combined with the development of cleaning methods [92, 93, 121], resulted in mobilities well beyond $10^5\,\mathrm{cm^2\,V^{-1}s^{-1}}$ [118, 120].

In order to gather knowledge on spin relaxation processes and possibly enhance spin lifetimes, it is important to fabricate suspended graphene spintronic devices. Unfortunately, the accepted fabrication technique for suspended structures cannot be used for this purpose. Suspended structures are usually created in three steps that consist of depositing graphene onto a sacrificial $SiO_2$ layer, contacting graphene

with Cr/Au electrodes and then etching $SiO_2$ away using a hydrofluoric acid (HF) solution [118, 120]. Here, HF is an extremely aggressive acid that attacks most metals [122, 123], including the ferromagnets (Co, Ni, Fe, etc) that are essential for electrical spin injection and detection. As a consequence, it is mandatory to eliminate the HF etching step to fabricate suspended graphene spintronic devices. Additionally, it is desirable to minimize the fabrication steps and the chemicals to which graphene is exposed in order to achieve the largest possible carrier mobility.

Here, we demonstrate spin transport in suspended graphene devices using a unique method that overcomes the drawbacks mentioned above. The fabrication process of these devices is described in detail in chapter 3.4.5. The advantages of the process become clear when comparing it with the fabrication method for conventional graphene spin valves on a $Si/SiO_2$ substrate (see section 3.4.3). The conventional method requires the use of PMMA as a positive resist, a developer such as MIBK and acetone and isopropanol during lift-off. Therefore, the ultimately optimized method to fabricate suspended graphene devices should add one lithography step to define where graphene should be suspended, use only PMMA as a resist and avoid adding any solvents other than the previously listed. The process presented here fulfills these specifications.

Our fabrication method is highly versatile allowing us to easily introduce modifications in the device design, including the number of contacts, the separation between them and the height of the dielectric. Because it is an acid-free method with a minimal number of steps, it is compatible with any contact material and capable of producing very high quality devices, even without any further processing.

Alternative approaches have been demonstrated which enable acid free fabrication of suspended graphene samples as well [69, 124, 125]. These methods however require the use of polymers other than PMMA, namely positive lift-off resists such as LOR, and a variety of chemicals.

## 5.3. Results and Discussion

A typical device is shown in Fig. 5.1 (b), and measurements of the same device are presented in Fig. 5.2. The device consists of a graphene monolayer with four contacts and three suspended graphene regions between them. The resistivity and mobility of the device, without any post fabrication processing, is plotted as a function of carrier density $n$. A sharp resistivity peak (Fig. 5.2 (a)) close to backgate voltage $V_{BG} = 0\,V$ with a soft $p$ doping ($n \sim 10^{11}\,cm^{-2}$) is observed. The mobility is well above $5 \times 10^3\,cm^2\,V^{-1}s^{-1}$ and exceeds $2 \times 10^4\,cm^2\,V^{-1}s^{-1}$ for $n = 10^{11}\,cm^{-2}$ at room temperature (Fig. 5.2 (b)). This is an excellent starting point when compared with other fabrication methods and implies that argon/hydrogen annealing [92, 121] or current annealing [93] can likely be used to obtain ultrahigh mobility samples.

We also extract the residual carrier density $n_0$ of our devices. Charged impurities in the vicinity of graphene induce a non-zero value of $n$ and the total carrier concentra-

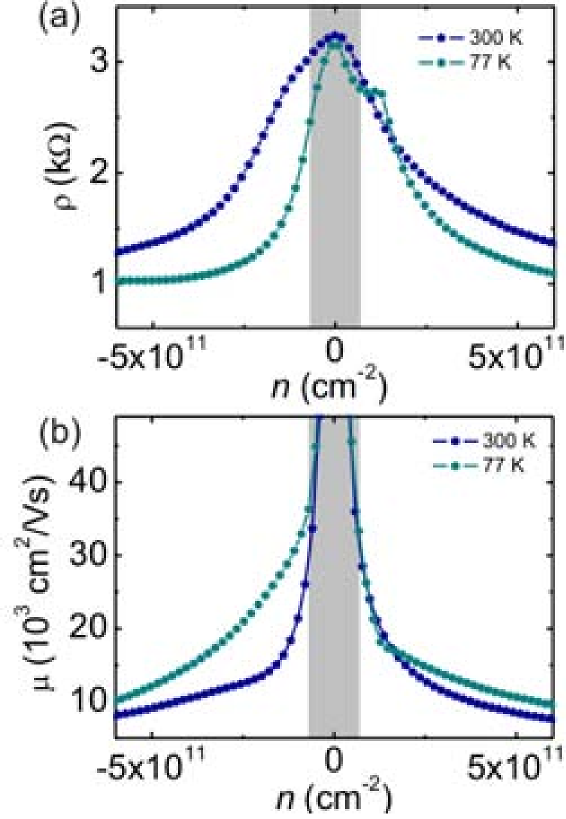


Figure 5.2.: (a) Resistivity of a suspended graphene monolayer over a 1 $\mu$m trench at room temperature and 77 K. The Dirac-point of the sample is close to $V_{\mathrm{BG}} = 0\,\mathrm{V}$ with a soft $p$ doping ($n_0 \sim 10^{11}\mathrm{cm}^{-2}$). An optical microscope image of the device is shown in Fig. 5.1. (b) Mobility of the sample.

tion can be approximated as [50] $n_{\mathrm{tot}} = (n_0^2 + n(V_{\mathrm{BG}})^2)^{1/2}$. Fitting the curves in Fig. 5.2 delivers $n_0 = 1.4 \times 10^{11}\,\mathrm{cm}^{-2}$ at room temperature and $n_0 = 8.7 \times 10^{10}\,\mathrm{cm}^{-2}$ at 77 K, indicating the high quality of our as-processed devices. The room temperature residual carrier concentration is indicated by gray areas in Fig. 5.2. For $n < n_0$, the mobilities given by formula 2.61 have to be disregarded.

Figure 5.3 (b) shows a device based on FLG with eight Co contacts (100-200 nm wide) and suspended regions between them. By using the four inner contacts we performed non local spin injection/detection measurements [8, 16, 55]. The non local resistance $R_{\mathrm{NL}} = (V^+ - V^-)/I$ presents clear spin signatures (Fig. 5.3 (a)) as an in plane magnetic field B along the ferromagnetic electrodes is swept up (green circles) and down (blue circles). The various values of $R_{\mathrm{NL}}$ are associated to different magnetization alignments of the contacts as represented with arrows [126]. A change

$\Delta R_{\mathrm{NL}} = 12.5\,\Omega$ is observed when the central electrodes switch from parallel to antiparallel states. As in Ref. [126], the switching sequence is determined by the width of the electrodes, which leads to distinct switching fields that we have characterized in prior experiments.

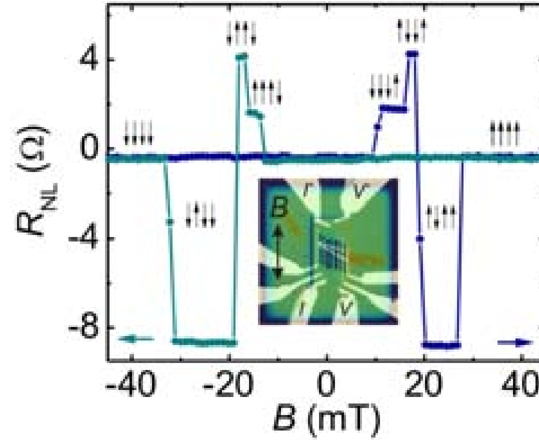


Figure 5.3.: (a) Non local spin resistance $R_{\mathrm{NL}}$ in a multiterminal device as the magnetic field $B$ is swept up (green symbols) or down (blue symbols) along the ferromagnetic electrodes (Co). Measurements are performed at $V_{\mathrm{BG}} = 0\,\mathrm{V}$ and room temperature. Inset: Optical microscope image of the device and the configuration of the electrodes. The flake is indicated by the dashed lines.

For SLG and BLG, we observe a similar behavior as the one shown in Fig. 5.3, although the magnitude of the spin signal tends to be somewhat smaller for devices with similar dimensions. An example is shown in Fig. 5.4, where data of a BLG device is presented. Spin valve measurements exhibit a non local resistance of $\Delta R_{\mathrm{NL}} = 6\,\Omega$ (Fig. 5.4 (a)), while the observation of Hanle spin precession under a perpendicular B (Fig. 5.4 (b)) confirms the presence of a spin signal and provides a direct way to obtain $\tau_{\mathrm{sf}}$ [8]. Quantitatively, the response to the perpendicular B resulting from spin precession can be described with a one dimensional model which combines spin diffusion, precession and relaxation [8, 16, 55]. The fit indicates $\tau_{\mathrm{sf}} \approx 1.9\,\mu\mathrm{m}$ and $\tau_{\mathrm{sf}} \approx 125\,\mathrm{ps}$. These values are similar to those found in SLG with transparent contacts [127] and in BLG spintronic devices with the highest mobility reported [115].

Additionally, we note that the height of the spin signal is three orders of magnitude larger when comparing our devices to graphene spin valves using transparent contacts [127]. As we show in chapter 6, we attribute this increase to the deposition of an amorphous carbon layer at the interface between graphene and Co. This is due to the overexposure required for the crosslinking of the PMMA below graphene [128]. How-

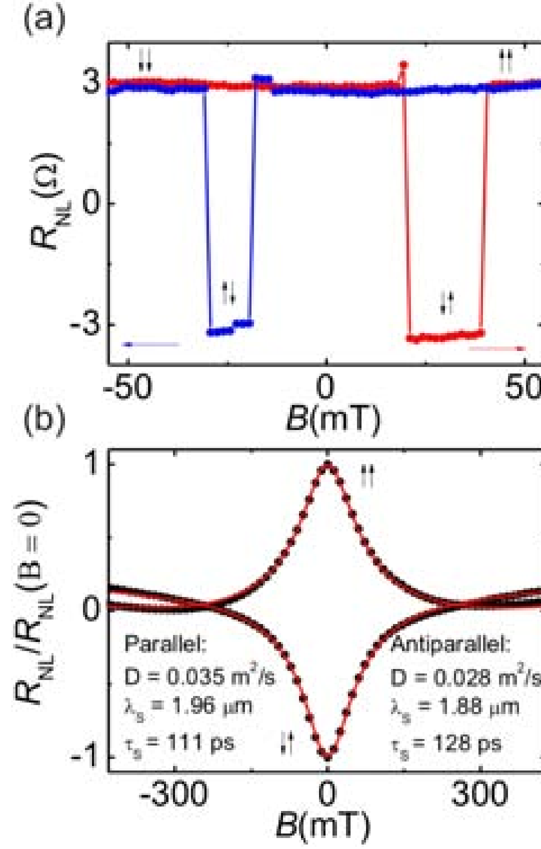


Figure 5.4.: (a) Non local spin valve measurement in BLG at room temperature and $V_{\mathrm{BG}} = 0\,\mathrm{V}$ (b) Spin precession in a perpendicular magnetic field of the same device. The center to center distance of the inner contacts is $1.15\,\mu\mathrm{m}$, arrows represent their configuration. The fit (red line) to a one-dimensional model delivers a spin relaxation length of $1.9\,\mu\mathrm{m}$.

ever, here we only expose the contact area of our devices to the high dose of e-beam, in contrast to the devices presented in chapter 6. This has important consequences.

While the high dose of e-beam radiation could damage graphene [129], the formation of the amorphous carbon layer results in an increased contact resistance $R_{\mathrm{C}}$. This increase leads to the increased values of $\Delta R_{\mathrm{NL}}$ due to the improved spin injection characteristics of our contacts.

We thus find the exposure of the contact area by a high dose of e-beam beneficial for spin injection experiments. However, this is not the case for the rest of the graphene sheet. In particular, a recent report [130] based on transmission electron microscope (TEM) imaging shows that amorphous carbon deposited on graphene during electron beam exposure cannot easily be removed by current annealing. It instead induces the crystallization of the amorphous carbon and the formation of (multilayer) graphene

patches due to the high temperatures involved.

During the fabrication of our devices, we do not expose the graphene in between the contacts. Therefore, we expect that we deposit amorphous carbon only in the contact areas, and higher mobilities than those presented here can likely be obtained by current annealing of the unexposed graphene.

## 5.4. Conclusion

In summary, we have performed electrical detection of spin accumulation and of spin precession in freely-suspended graphene flakes from which we can estimate spin relaxation lengths and times. We observe non local spin signals as high as $\Delta R_{\mathrm{NL}} \sim 10\,\Omega$.

The device fabrication involves a minimal number of steps and chemicals and, because it is acid-free, it can be adapted to any contacting material. Mobilities as high as $2 \times 10^4\,\mathrm{cm^2\,V^{-1}s^{-1}}$ for $n = 10^{11}\,\mathrm{cm^{-2}}$ are observed at room temperature without any post fabrication processing. Argon/hydrogen and current annealing can be used to obtain ultrahigh mobility samples that will open the way for a detailed understanding of the spin relaxation mechanisms in graphene.

We expect that the demonstration of clean suspended graphene devices in few steps with minimal number of chemicals is not only important for the spintronics community, but also for those interested in graphene nanomechanics [131] and future research in pseudomagnetic fields and the modification of the graphene transport properties due to strain [70, 132].

# 6. Enhanced Spin Accumulation in Graphene Spin Valves

## 6.1. Introduction

We demonstrate a large enhancement of the spin accumulation in monolayer graphene following electron-beam induced deposition of an amorphous carbon layer at the ferromagnet-graphene interface. The enhancement is $10^4$-fold when graphene is deposited onto PMMA and exposed with sufficient e-beam dose to crosslink the PMMA, and $10^3$-fold when graphene is deposited directly onto $SiO_2$ and exposed with identical dose. We attribute the difference to a more efficient carbon deposition in the former case due to an increase in the presence of compounds containing carbon, which are released by the PMMA. The amorphous carbon interface can sustain large current densities without degrading, which leads to very large spin accumulations close to 1 mV at room temperature.

## 6.2. Motivation

Graphene has attracted the attention of the spintronics community due to the long spin lifetimes and long relaxation lengths expected from its small intrinsic spin orbit interaction and the lack of hyperfine interaction with the most abundant carbon nuclei $^{12}$C [20, 133], which we discuss in section 2.9 and chapter 5. Here, we instead focus on the interface and spin injection properties of our graphene non local spin valve devices. If large spin accumulation and large pure spin currents are achieved, NLSVs can be used to study spin torque switching [13] or spin Hall effects [134]. We demonstrate spin accumulations $\Delta V_{\mathrm{NL}} \sim 1\,\mathrm{mV}$, which are among the largest values reported in any material.

Depending on the interface characteristics between the FM and graphene, graphene NLSVs have been classified into three types: those having Ohmic, pinhole or tunneling contacts [135]. As shown in chapter 2.5, the spin dependent voltage measured at the detector depends on the ratio between the contact resistances and the spin resistances of the materials.

In case of the tunnel junctions, the spin accumulation in the graphene is given by Eq. 2.34. Although the magnitude of $\Delta R_{\mathrm{NL}}$ is much higher ($\sim 100\,\Omega$) than in the other cases [135], the maximum spin current density is limited by two factors. Firstly,

the bias may not exceed the breakdown voltage of the tunnel barrier, typically of the order of a few mV. Secondly, the magnitude of the spin valve signal in these devices is strongly bias dependent, with the signal deteriorating for increasing bias currents [94], as discussed in chapter 4.

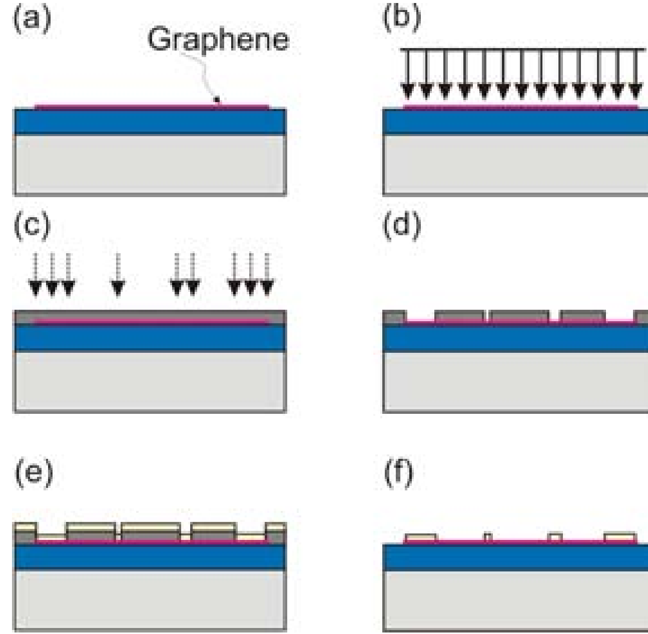


Figure 6.1.: Fabrication process for type B samples. (a) Deposition of graphene on $SiO_2$/Si substrate (b) EBID of aC (c) EBL contacts (d) Substrate after development (e) Metal deposition (f) Completed device

Also for pinhole barriers, the bias current is limited to a few $\mu$A [55]. Although the spin signal is smaller than in case of tunnel barriers, pinhole barriers are easier to fabricate than pinhole free tunnel barriers. The reported values of $\Delta R_{\mathrm{NL}}$ are of the order of a few Ohms to tens of Ohms [55, 135].

For both tunnel as well as pinhole barriers, the used insulators are typically $Al_2O_3$ or MgO, because of their succes for tunnel magnetoresistance [102, 136, 137, 138].

For transparent contacts, typical reported values of $\Delta R_{\mathrm{NL}}$ are in the range of a few mOhms to a few tenths of mOhms [127]. The spin injection efficiency, i.e. the effective spin polarization, is strongly supressed because of the resistance mismatch and the spin absorption at both injector and detector FMs. However, the bias current is not limited by the interface properties and currents of hundreds of $\mu$A can be applied to these devices, which constitues an advantage when trying to obtain high values of spin accumulation $\Delta V_{\mathrm{NL}}$.

Alternative approaches to increase $\Delta R_{\mathrm{NL}}$ and the spin accumulation $\Delta V_{\mathrm{NL}}$ have been proposed in metallic systems, by adding a native oxide layer at an $Ni_{80}Fe_{20}$/Ag

interface [139] or by increasing confinement [140] and in graphene by adding a thin Cu layer at the FM/graphene interface [141].

## 6.3. Amorphous Carbon as Interface Material

In the present work, we investigate FM/aC/graphene junctions as a spin polarizer, where aC stands for amorphous carbon. Amorphous carbon is deposited with high resolution using a focused electron-beam that decomposes molecules, such as hydrocarbons, that are then adsorbed on graphene. This process, known as electron-beam induced deposition (EBID), is well established [142] and has been used, for example, to fabricate complex carbon structures [143], conducting bridges [144], and low resistance contacts with nanotubes [145]. Carbon precursors can either be introduced externally using a gas source or simply be present as residual hydrocarbons at the background pressure of a scanning electron microscope (SEM) chamber [142]. Carbon deposition from residual hydrocarbons in graphene was recently demonstrated by direct visualization in a transmission electron microscope [130].

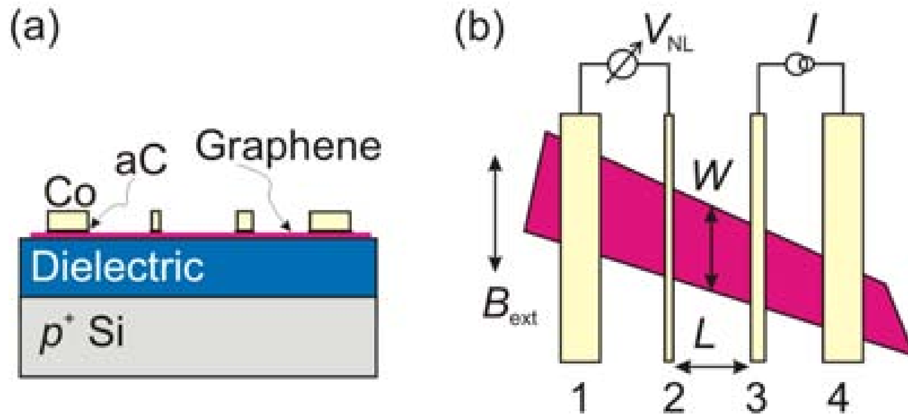


Figure 6.2.: Device layout, lateral (a) and top (b) views. Four ferromagnetic electrodes are in contact with graphene. The dielectric consists of 440 nm of $SiO_2$ for type A and B devices, and 285 nm of $SiO_2$ plus 200 nm of PMMA for type C devices (see text). A layer of amorphous carbon is deposited with EBID at the interface between graphene and Co for type B and C devices.

In short, exposing graphene to e-beam radiation leads to the deposition of aC in the exposed area. Keeping this in mind, we consider the fabrication process of our suspended graphene devices, as described in chapter 3.4.5. While crosslinking the PMMA, we expose the graphene to a dose more than 20 times higher than the dose required for regular electron beam lithography. We can therefore assume that during this step an aC layer is deposited on graphene, which then acts as intermediate layer, once the ferromagnetic material is deposited.

In order to test this assumption, we have fabricated three different types of samples, in the following referred to as type A, B and C. Type A devices are reference samples with transparent, Ohmic contacts, as described in chapter 3.4.3 and reported in previous studies [146, 147]. The fabrication process of type B devices is schematically shown in Fig. 6.1. It differs from the type A fabrication process in step (b), exposure of graphene with a dose of 9000 $\mu$C/cm$^2$. This dose is large enough to deposit a thin layer of aC at the residual pressure of our system [142, 143, 144, 145], which is in the $10^{-6}$ Torr range. It is also the dose needed to crosslink PMMA. Type C devices are samples fabricated using crosslinked PMMA as substrate, as described in section 3.4.4. Therefore, type A devices are standard graphene spin valves on a Si/SiO$_2$-substrate, for type B samples we introduce an additional aC deposition step and type C samples are fabricated using the additional step as well as being fabricated on crosslinked PMMA as a substrate. This is schematicallly shown in Fig. 6.2 (a), where the dielectric consists of 440 nm of SiO$_2$ for type A and B samples, and of 285 nm of SiO$_2$ and 200 nm of PMMA for type C samples. Moreover, the aC layer between FM and graphene is only present for type B and C samples.

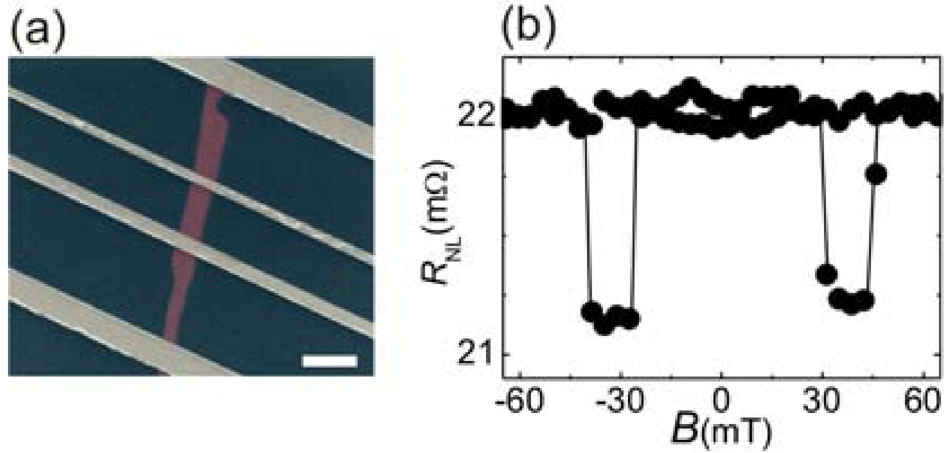


Figure 6.3.: (a) SEM image of a device, the scale bar equals 1 $\mu$m (b) NLSV measurement for a reference device with transparent contact (type A)

The use of PMMA as high-$\kappa$ dielectric substrate for graphene has been reported previously [84], but it can also be used for the fabrication of insulating [63, 85] of hydrophobic layers [148]. More important, it increases the presence of carbon rich molecules in the EBL system during EBID, changing the dynamics of the aC deposition process.

## 6.4. Experimental Results and Discussion

The device design is shown in Fig. 6.2 (b). The distance $L$ between the inner contacts is kept constant at 1.15 $\mu$m for all devices, while the width of the graphene $W$ varies between 500 nm and 1 $\mu$m. The widths of the ferromagnetic electrodes determine their coercive fields, the thinner electrodes having the largest coercive fields. The inner electrodes, 2 and 3, are 100 nm and 200 nm wide, respectively, while the outer ones, 1 and 4, are both 500 nm wide. A current $I$ is injected between two of the ferromagnetic electrodes (3 and 4) resulting in a nonlocal voltage $V_{\mathrm{NL}}$ over the detector electrodes (1 and 2). Application of an in-plane, external magnetic field $B$ along the axis of the ferromagnets allows us to switch their magnetizations sequentially. As we sweep $B$, a change in the nonlocal spin resistance $R_{\mathrm{NL}} = V_{\mathrm{NL}}/I$ occurs when the relative orientation of the magnetizations of the inner ferromagnets switches from parallel to anti-parallel.

An SEM image of a sample is shown in Fig. 6.3 (a), as well as a NLSV measurement of a type A, reference sample (b). Here, $\Delta R_{\mathrm{NL}}$ is about 1 mOhm, in agreement with previously reported values for transparent contacts [127, 146, 147]. All measurements presented in this chapter were carried out at room temperature.

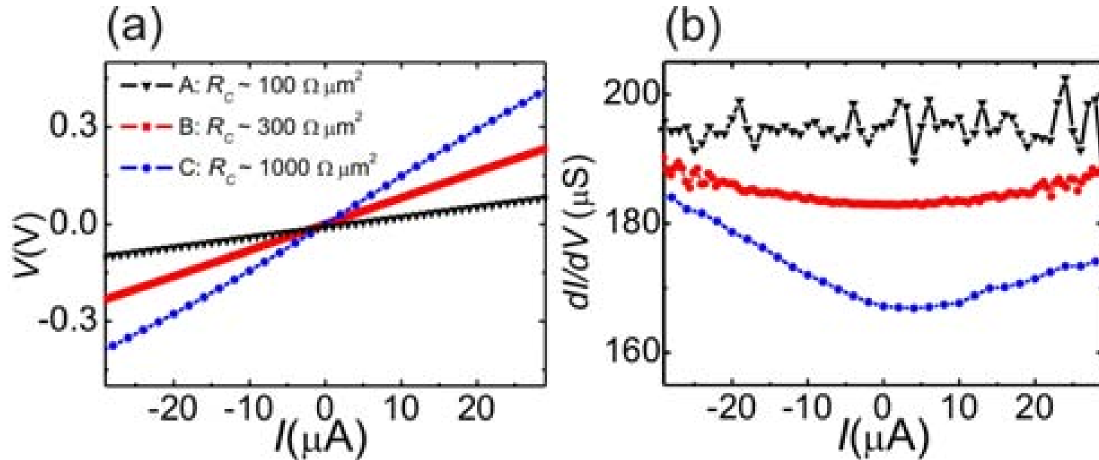


Figure 6.4.: (a) Typical IV-curves for the three types of devices: type A (black triangles), type B (red squares) and type C (blue circles). (b) Corresponding $dI/dV$-curves, offset for clarity (+50 $\mu$S for type B, +85 $\mu$S for type C).

Our main results are shown in Figs. 6.4 to 6.6, where we compare data of three specific devices. Amorphous carbon deposition by EBID leads to an increase in the contact resistance per unit area, $R_{\mathrm{C}}$, between the ferromagnet and graphene [Fig. 6.4 (a)] and dramatically enhances the nonlocal spin signal [Fig. 6.5]. We performed IV-measurements in 2-point configuration between pairs of ferromagnetic electrodes [Fig. 6.4 (a)]. Even though it is not straightforward to accurately determine the contact

resistance between graphene and a metallic electrode [149], our measurements demonstrate that $R_C$ systematically increases from A to B to C devices. After subtracting the resistance from the leads and graphene (measured in four point configuration) [150], we roughly estimate that $R_C$ is $< 100\,\Omega\mu\text{m}^2$ for type A devices, as observed previously [127]. For type B and C devices, $R_C$ increases significantly to about 300 and $1000\,\Omega\mu\text{m}^2$, respectively. Numerical differentiation of the IV-measurements [Fig. 6.4 (b)] reveals nonlinearities in these devices that are not observed in the type A ones, which is an indication of the different nature of the interfaces. Previous studies in metal-carbon nanotube contacts fabricated by EBID presented similar features, which were associated to a combination of tunneling and Ohmic resistances [145].

The thickness of the aC layer can be roughly estimated by assuming Ohmic behavior and using typical resistivity values of EBID-grown aC films [144], $\rho^{\text{aC}} \approx 2 \times 10^5\,\Omega\mu\text{m}$. Considering an increase of $\sim 100\,\Omega\mu\text{m}^2$ and $\sim 800\,\Omega\mu\text{m}^2$ in the contact resistance (after subtracting $100\,\Omega\mu\text{m}^2$ per interface), we calculate that the aC thickness for type B and type C devices is about 0.5 nm and 4 nm respectively. These values represent an upper limit for the thickness because roughness in the aC films and tunneling transport would effectively increase the contact resistance. It is also plausible that a small amount of carbon on graphene changes the deposition dynamics of the cobalt that follows, leading to a different structure at the interface, and perhaps, to different characteristic resistance and polarization [151]. The coexistence of two structures with similar energy was recently observed in graphene on Ni(111) [152].

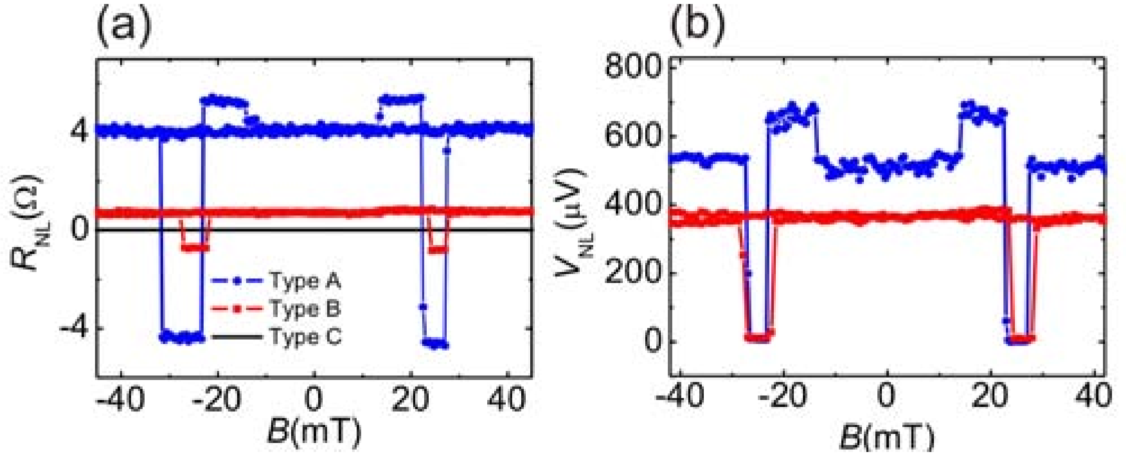


Figure 6.5.: (a) NLSV measurements for the devices in 6.4. $\Delta R_{\text{NL}}$ for type C devices is roughly four orders of magnitude larger than for type A devices. (b) NLSV measurements for $I = 400\,\mu\text{A}$ (type B) and $I = 46\,\mu\text{A}$ (type C). The data was displaced vertically to stress the overall change of $V_{\text{NL}}$, $\Delta V_{\text{NL}}$.

NLSV measurements for typical A, B and C devices are shown in Fig. 6.5 in the same scale. We have found that $\Delta R_{\text{NL}}$ for type B devices varies from hundreds of mOhms

to the lower Ohms range, which is three orders of magnitude larger than the values for our type A devices. The enhancement is so large that the features of the measurements shown in Fig. 6.3 (b) cannot be resolved in Fig. 6.5 (a) and appear as a straight line. For type C devices, $\Delta R_{\mathrm{NL}}$ is even larger, typically about ten Ohms ($\approx 8$ Ohms for the device in Fig. 6.5). This represents an additional order of magnitude increase and, therefore, up to a $10^4$-fold overall enhancement when comparing with type A devices. $\Delta R_{\mathrm{NL}}$ in type B and C devices compares well with the reported values for pinhole contacts using conventional insulators such as MgO or $Al_2O_3$ [55, 115, 135]. As opposed to the case of MgO or $Al_2O_3$ interfaces, high-current densities can be applied to our contacts without deteriorating them. As shown in Fig. 6.5 (b), we are able to achieve very large absolute nonlocal spin voltages of about $500\,\mu$V, which surpasses the largest value previously reported in any material by more than a factor 2 [94, 153]. In more recent measurements, presented in chapter 7, we demonstrate even higher values of $\Delta V_{\mathrm{NL}}$ close to 1 mV. Taking into account the polarization $P$ of the current, this corresponds to a difference in electrochemical potential of spin up and spin down carriers of 20 meV.

We performed Hanle spin precession measurements to determine the spin relaxation length $\lambda_{\mathrm{sf}}$ of these devices. Such measurements, shown in Fig. 6.6 were only possible for type B and C devices because of the small signal and the large spin absorption by the contacts occurring for the type A ones. By fitting the measurements to a one-dimensional model [8, 55], we obtain $\lambda_{\mathrm{sf}} \approx 1.3\,\mu$m. The distance between the contacts is thus smaller than $\lambda_{\mathrm{sf}}$ and minor changes in $\lambda_{\mathrm{sf}}$ cannot change the magnitude of $R_{\mathrm{NL}}$ significantly.

The fits in Fig. 6.6 also deliver the spin lifetime $\tau_{\mathrm{sf}}$. For the presented devices, the spin lifetime is smaller for device C (85 ps) as for device B (146 ps). However, $\tau_{\mathrm{sf}}$ is in the 100 to 200 ps range for most devices and we do not find a clear correlation between the spin lifetime and the type of substrate (PMMA or $SiO_2$).

Having extracted these parameters, we can obtain the effective polarization $P$ of the ferromagnetic electrodes using Eq. 2.34. $P$ is approx. 5 % for device B and approx. 10 % for device C. It is interesting to compare these values to those obtained in devices with the conventional interface types. For transparent contacts, polarizations as low as 1 % have been reported [127], for pinhole contacts 2-18 % [55, 154, 155] and values as high as 30 % for tunneling (pinhole-free MgO) barriers [135].

We thus argue that the increase in $R_{\mathrm{C}}$ is solely due to EBID. In the case of type B devices, the aC originates from the hydrocarbons present in the chamber of the electron-beam lithography system, as previously observed [142, 143, 144, 145]. The additional increase in $R_{\mathrm{C}}$ for type C devices is associated to the release of carbon-rich molecules from the PMMA layer, which act as precursors and decompose in the electron-beam irradiated area, resulting in a larger aC-deposition rate than at the residual chamber pressure [142].

The introduction of disorder in graphene by the electron-beam is unlikely at an acceleration voltage of 30 keV, which is below the knock-on damage threshold of carbon

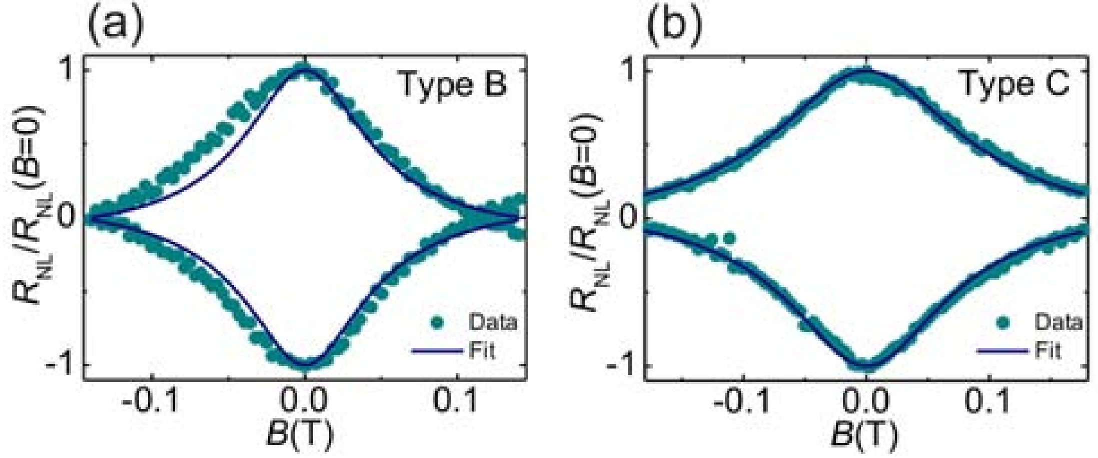


Figure 6.6.: Hanle precession measurements of the overexposed devices in Fig. 6.5: type B (a) and type C (b). In both cases, we extract $\lambda_{sf} \approx 1.3\,\mu$m.

nanostructures [130, 156]. This agrees with the fact that we found no correlation between the carrier mobility of the graphene sheet and the exposure to the e-beam dose, even when graphene is fully exposed. Indeed, graphene on crosslinked PMMA frequently exhibits higher mobility and lower residual doping than graphene on $SiO_2$. The mobilities of the discussed devices were of about 2000 to 3000 $cm^2/Vs$ but in some cases it can exceed 20000 $cm^2/Vs$ for fully exposed graphene. Examples are shown in Fig. 6.7, where we compare resistivities $\rho$ and mobilities $\mu$ of a type B and a type C device.

Despite the fact that no signs of degradation of the graphene sheet are observed after EBID, if possible, one should perform the EBID step in the contact region only, which leaves the graphene between the contacts completely unaffected. This could be relevant for efficient cleaning of the graphene sheet because, as recently pointed out [130], it might not be possible to easily remove amorphous carbon by current annealing after EBID.

Finally, an additional step in $R_{\mathrm{NL}}$ as a function of $B$, which is due to the switching of the outer electrodes, becomes apparent in the NLSV measurements of our type C devices [Fig. 6.5; $B \sim 15\,\mathrm{mT}$]. This feature is well-known [126] and, for wide contacts, we argue that is only present when a sufficiently large contact resistance prevents the spin-absorption effect. In Fig. 6.8, we qualitatively show the variation of the electrochemical potential $\mu_{\mathrm{HR,T}}(x)$ for spin-up and spin-down electrons for transparent (T) and highly resistive (HR) contacts at the detector electrodes, corresponding to type A and type C devices. If the contact resistance is high [Fig. 6.8 (a)], no contact induced spin relaxation occurs and, therefore, when the magnetization of the outer detector switches, $V_{\mathrm{NL}}$ changes by $\Delta V_{\mathrm{NL}} \propto \Delta\mu_{\mathrm{HR}}(x = x_2)$. In the case of transparent contacts [Fig. 6.8 (b)], the effect of the spin absorption by the ferromagnet is two-fold.

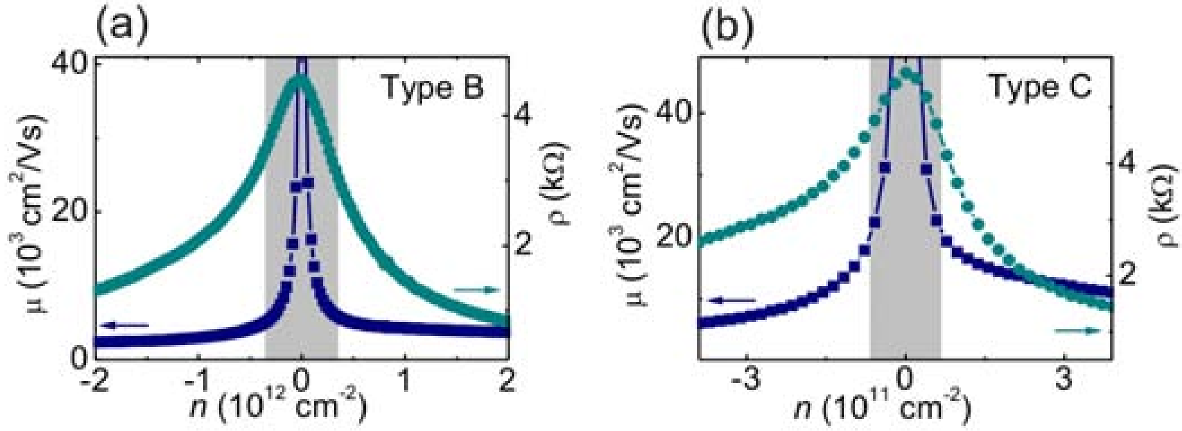


Figure 6.7.: Mobilities of (a) type B and (c) type C devices. The overexposure required during fabrication of these devices (as shown in Fig. 6.1 (b)) does not lead to a notable degradation of the graphene, as the extracted mobilities can exceed 20000 $cm^2$/Vs at room temperature.

The overall spin accumulation is smaller and, for wide enough contacts, it is completely suppressed below the contact. In this situation, the switching of the outer detector electrode does not affect the measurements because $\Delta V_{\mathrm{NL}} \propto \Delta\mu_{\mathrm{T}}(x = x_2) = 0$. An analogous argument can be made in relation to the second injector. Thus, the fact that this feature occurs most notably for type C devices further corroborates our hypothesis of the formation of an aC interface layer that increases the contact resistance between Co and graphene and leaves graphene unaffected.

## 6.5. Conclusion

In summary, we have implemented graphene based non local spin valves on $SiO_2$ and on PMMA. Non local measurements show that an amorphous carbon layer at the FM/graphene interface deposited by electron-beam induced deposition can result in a large enhancement in the spin injection/detection efficiency, even at large applied injection currents for which we find the contacts to be stable. Our results show a $10^4$-fold enhancement in comparison to Ohmic contacts, but further improvements can be expected after optimizing the deposition of carbon by choosing the appropriate carbon precursor and by controlling its quantity in a suitable electron beam lithography system. Nevertheless, further studies are required to precisely determine the nature of the interface, which can have Ohmic or tunneling character or a combination of both.

In order to test the transferability of our methods, we have repeated the amorphous carbon deposition procedure in a second EBL system from a different vendor and have found essentially the same results. This underscore the importance of amor-

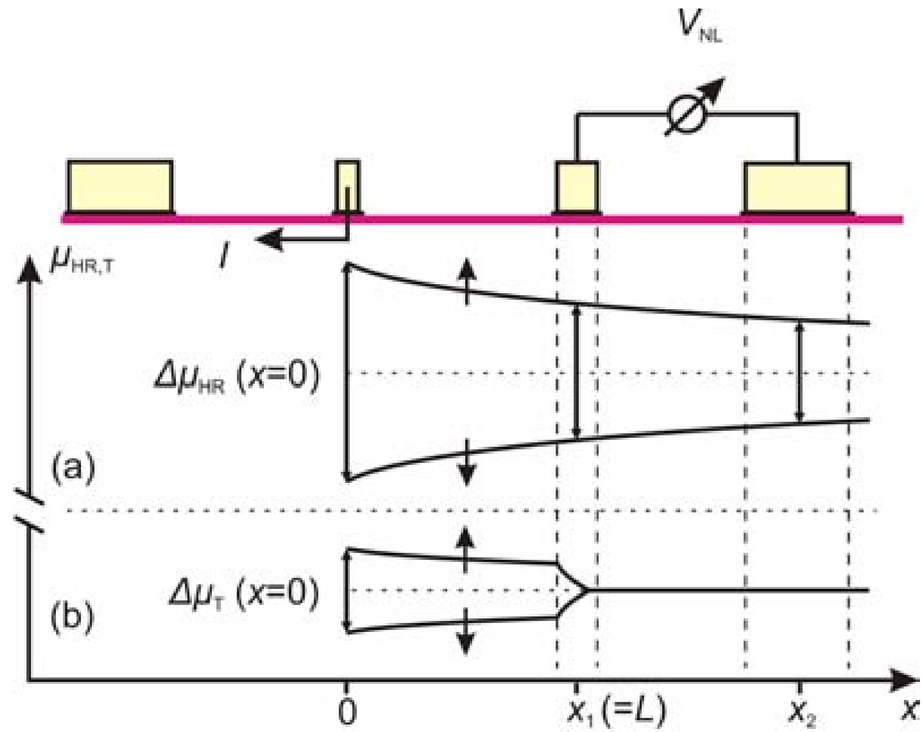


Figure 6.8.: Schematics of the spin-up and spin-down electrochemical potentials in graphene for highly resistive (a) and transparent (b) contacts.

phous carbon for future spintronic research, especially because of the simplicity and the transferabillity of the deposition method and the low reactivity of carbon. Amorphous carbon can be used as an alternative material to conventional insulators used in spintronics, such as MgO or $Al_2O_3$. In particular, it might open the path for reproducible spin transport measurements in carbon allotropes other than graphene, such as carbon nanotubes, which have eluded researchers for more than a decade.

# 7. Spin Thermocouple and Giant Spin Accumulation in Single Layer Graphene

## 7.1. Introduction

The interaction between charge, spin and heat currents in solid state media can lead to novel phenomena, which are treated in the field of Spin Caloritronics. We introduce the field, which recently obtained renewed attention, in section 2.7 from a theoretical point of view. Here, we present experimental results underlining the potential of graphene for spin caloritronics. In particular, we demonstrate how spin up and spin down carriers in graphene non local spin valves form the two arms of a thermocouple. We therefore refer to this device as a spin thermocouple. Graphene, with its energy dependent density of states and Seebeck coefficient $S$, has the properties required for the experimental realization of such a device.

In our devices, we observe values of the spin accumulation $V_{\mathrm{NL}}$ as large as 1 mV. This corresponds to a spin splitting of approx. 20 meV, which to our knowledge is the largest value observed to date in any material. Because of the large splitting, it is possible to observe considerable quantities of carriers with opposite spin and charge at the Dirac point, where the spin up carriers are electrons and the spin down carriers holes. The non local voltage detected in such a device is therefore significantly enhanced close to the charge neutrality point when a sizeable Joule heating is present. This is due to the spin polarization of the heat current caused by the energy dependent Seebeck coefficient of graphene leading to a supralinear behavior of the spin accumulation $V_{\mathrm{NL}}$ as a function of the bias current.

Our observations hint at the possibility of a novel way to control and sustain spin transport.

## 7.2. General Concept

### 7.2.1. Context

The interaction of heat currents and the electronic spin has been a topic of research since the 1980s [157]. In recent years, new spin dependent thermal effects have been

discovered in ferromagnets and the topic is receiving renewed interest [23, 24, 25, 45, 158]. One of the most intriguing phenomena is the spin Seebeck effect (SSE) in which a thermal gradient in a ferromagnet gives rise to spin currents that are detected via the inverse spin Hall effect in a metallic strip transverse to the temperature gradient [23]. However, even though the SSE is experimentally established in metals, insulators and semiconductors, the underlying mechanism has been proven far more complex than originally envisioned, involving both magnons and phonons in the ferromagnet and the substrate.

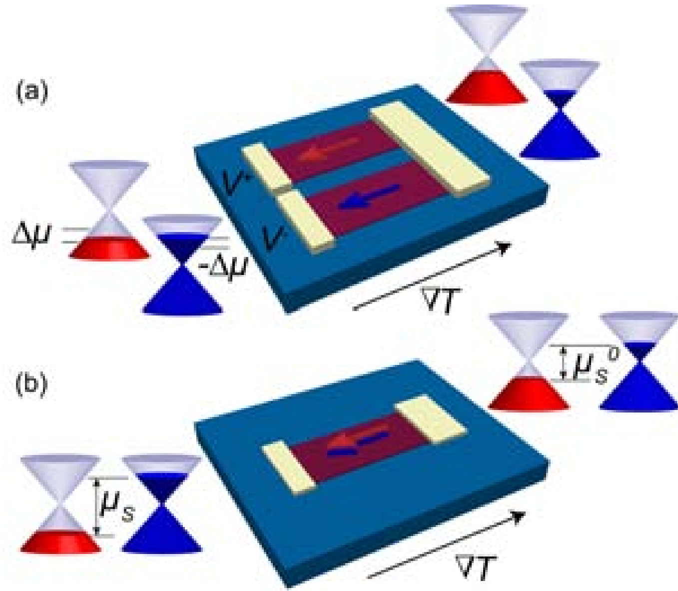


Figure 7.1.: Charge and spin thermocouple in graphene. (a) Charge thermocouple formed by two graphene flakes. A thermoelectric voltage is built up due to the temperature gradient $\nabla T$. The sign of the voltage is determined by the character of the carriers. (b) Spin thermocouple. If carriers with opposite spin orientation can be approximately described as belonging to two independent transport channels, the thermolelectric effect in (a) leads to an anomalous increase of the spin accumulation due to the effective spin dependence of the Seebeck coefficient $S$ of graphene.

In this chapter, we describe a new phenomenom in which spin accumulation in graphene under a thermal gradient presents an anomalous enhancement away from the injection point. The spin accumulation is generated by electrical spin injection in a graphene NLSV and the enhancement is due to an effective spin dependent Seebeck coefficient $S$.

This can be understood by examining the working principle of a conventional, charge thermocouple. In graphene, such a device can be fabricated using two strips of dissimilar carrier density. In Fig. 7.1 (a), an ideal device is shown in which the majority

of carriers in one arm are electrons and in the other arm holes. A thermoelectric voltage builds up in both arms due to the Seebeck effect, introduced in section 2.2. The sign of the Seebeck coefficient $S$ changes across the charge neutrality point as the majority carriers switch from electrons to holes. If the Fermi levels of the sheets in Fig. 7.1 (a) are tuned to be equidistant from the Dirac point, the induced voltage in the thermocouple is $V = 2S^*\Delta T$, where $S^* = |S^e| = |S^h|$ is equal to the magnitude of the electron and the hole Seebeck coefficients, $S^e$ and $S^h$ respectively, and $\Delta T$ is the temperature difference between the electrodes.

For length scales smaller than the spin relaxation length, carriers with opposite spin orientation in a non magnetic material can be approximately described by two independent transport channels. as schematically shown in Fig. 7.1 (b). This is the two-current model, introduced in section 2.3. In graphene, the spin relaxation length can exceed several micrometers [115] and spin injection from a FM can result in very large spin splitting [55, 159]. If the carriers of spin up and spin down sub bands have electron or hole character, repectively, the scenario represented in Fig. 7.1 (a) is intrinsically present in a single graphene sheet, where electron and holes are constrained to different spin sub bands instead of the two graphene sheets that form the thermocouple junction in Fig. 7.1 (a). Because of the symmetry of electrons and holes, the overall thermoelectric voltage between hot and cold ends of the graphene cancels out. However, the spin accumulation $\mu_{\mathrm{S}}$ increases by $\Delta\mu_{\mathrm{S}} = e\Delta S\Delta T^c$, where $\Delta S = S^{\uparrow} - S^{\downarrow}$ is the difference between the Seebeck coefficients for spin up and spin down, $S^{\uparrow}$ and $S^{\downarrow}$, and $T^c$ is the effective temperature of the carriers that, in general, can differ from the lattice temperature $T^l$.

### 7.2.2. Graphene NLSV as Spin Thermocouple

A spin thermocouple, as described above, is formed at the Dirac point of any conventional graphene NLSV, if the injector current is large enough to create a sizeable Joule heating. A graphical representation of the device layout is shown in Fig. 7.2: Spin accumulation is generated by electrical spin injection, as the charge current density $j_c$ results in a spin current density $j_s$ in the graphene. For sufficiently large bias currents $I$, Joule heating of the injector circuit leads to a temperature gradient $\nabla T$ in the graphene and the substrate. The resulting heat current in the graphene sheet contributes to the spin accumulation due to the effective spin dependence of $S$.

Graphene is an ideal candidate to investigate the interplay between spin and heat current related effects. $\Delta V_{\mathrm{NL}} = V^{\uparrow} - V^{\downarrow}$, which is the difference of the non local voltage between the P and AP alignment of the FMs $V^{\uparrow}$ and $V^{\downarrow}$, is a measure of the spin accumulation, while the thermoelectric voltage in the device is given by $V_{\mathrm{th}} = (V^{\uparrow} + V^{\downarrow})/2$. We further discuss this point in appendix B.2. $V_{\mathrm{th}}$ corresponds to a heat current density $j_q$, which is proportional to the conductivity of graphene, while the spin signal $\Delta R_{\mathrm{NL}}$ is proportional to $\sigma^{-1}$. Tuning the conductivity $\sigma(V_{\mathrm{BG}})$ therefore constitutes a tool to investigate the relation between spin and heat currents

in graphene NLSV.

Our study is further facilitated by the fact that in case of our graphene NLSV, the spin signal $\Delta R_{\mathrm{NL}}$ is of the order of a few Ohms, while our interfaces allow for high current densities [159], as discussed in chapter 6.

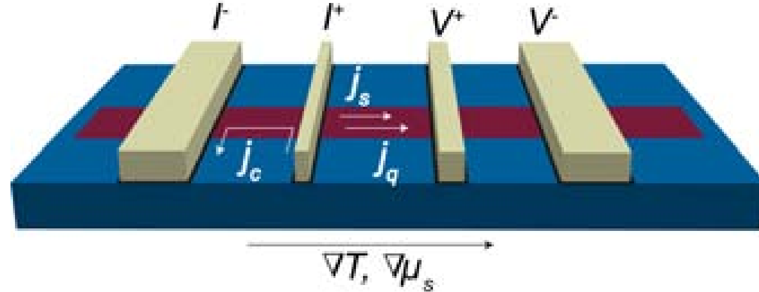


Figure 7.2.: Schematical representation of a graphene non local spin valve. Four Co electrodes (yellow) on top of a single layer graphene sheet (magenta). Electrical connections for NLSV measurements are indicated, the relative magnetization can be switched by the application of an in-plane, external magnetic field (not shown). The charge current density $j_c$ via the Co/graphene interface results in a pure spin current $j_s$ in the graphene. Additionally, a temperature gradient $\nabla T$ builds up, leading to a heat current $j_q$ in the graphene, which can be non negligible when a sizeable Joule heating is generated. Since the Seebeck coefficient of graphene is spin dependent, the heat current is spin polarized as well.

Traditionally, non local spin voltages in NLSVs have been attributed to spin accumulation due to pure spin currents in the non magnetic material. These have been studied extensively over the last decade [11, 15, 16, 44] and can be understood within the widely accepted phenomenological model of non local spin injection [41], which we discuss in detail in section 2.5. Pure spin currents are often quantified in terms of the transresistance $\Delta R_{\mathrm{NL}} = \Delta V_{\mathrm{NL}}/I$. In graphene NLSV with highly resistive contacts, $\Delta R_{\mathrm{NL}}$ can be expressed as [55] $\Delta R_{\mathrm{NL}} = (P_J^2 \lambda_{\mathrm{sf}}/\sigma W)\exp(-L/\lambda_{\mathrm{sf}})$. Here, $P_J$ is the interfacial current polarization, $\lambda_{\mathrm{sf}}$ the spin relaxation length of graphene, $\sigma$ its conductivity, $W$ the width of the flake and $L$ center to center distance of the electrodes.

In contrast to the spin current, the heat current is due to Joule heating associated with the bias current $I$ and thus proportional to $R_i I^2$, where $R_i$ is the resistance of the injector circuit. Joule heating in graphene-metal contacts has been quantified in a recent study [160]. It creates a temperature gradient along graphene, which leads to the diffusion of hot charge carriers into colder regions of the conductor. As we show in section 2.7, this temperature gradient acts as a generalized force which drives the thermal transport of carriers. Due to the effective spin dependent Seebeck coefficient

in graphene, also $j_q$ contributes to the spin accumulation.

In order to quantify the thermoelectric effects, we calculate the temperature distribution in our devices numerically. We find that the temperature difference between the detectors, $\Delta T_{\mathrm{DD'}}$, depends quadratically on the bias current $I$. The results are summarized in section B.

Focussing on the bias dependence of our devices, we observe an anomalous enhacement of $V_{\mathrm{NL}}$, corresponding to a supralinear behavior of the electrochemical potentials of spin up and spin down carriers in graphene. This is opposed to the sublinear dependence which can be expected by the monotonous increase in the carrier density away from the Dirac point.

## 7.3. Experimental Results

### 7.3.1. Device Characteristics

In the following, we present data on a particular, representative sample. The fabrication of our devices is described in section 3.4.4. We perform non local spin valve measurements as described in section 5.3 and chapter 6.

Figure 7.3 (a) shows a scanning electron microscope image of the device. It consists of four Co electrodes (yellow) in contact with single layer graphene (blue). The width of the inner two FMs is 100 nm and 200 nm, respectively, while the width $W$ of graphene is approx. 900 nm.

A typical NLSV measurement is shown in Fig. 7.3 (b). The switching of the relative magnetizations of the FM electrodes is reflected in the non local voltage $V_{\mathrm{NL}}$. In terms of transresistance, $\Delta R_{\mathrm{NL}} \approx 7\,\Omega$. The measurement is carried out at room temperature, with a current of $I = 50\,\mu\mathrm{A}$ and a backgate voltage of $V_{\mathrm{BG}} - V_{\mathrm{D}} = +3\,\mathrm{V}$.

We measure the field effect of graphene in four point configuration. Applying the bias current $I$ (typically $I = 1\,\mu\mathrm{A}$) to the outer electrodes, we measure the voltage drop between the inner two contacts in order to obtain the four point resistivity $\rho_{4\mathrm{P}}$ of the device. Comparing $\rho_{4\mathrm{P}}$ with $R_{\mathrm{NL}}$, as shown in Fig. 7.3 (c), it becomes obvious that $R_{\mathrm{NL}}$ exhibits a peak at the Dirac point, hinting to a tunneling-like behavior of the injected carriers [135]. Moreover, we extract the mobility of the sample from $\rho_{4\mathrm{P}}$, which can be as high as 20 000 $\mathrm{cm}^{-2}$, while the residual carrier concentration $n_i \approx 1.5 \cdot 10^{11}\,\mathrm{cm}^{-2}$.

The Seebeck coefficient $S$ can be calculated from $\rho_{4\mathrm{P}}$ using the semiclassical Mott relation [27, 161, 162]. This is shown in Fig. 7.3 (d) for room temperature and 77 K measurements. The magnitude of $S$ is nominally linear in temperature $T$ from 10 K to 300 K [27, 162]. For temperatures above $\sim 200$ K however, $S_{\mathrm{Mott}}$ is known to overestimate the actual value of $S$.

Finally, we have determined the spin relaxation length of the device by performing Hanle measurements and fitting these to a 1D-model [44]. We obtain values of $\lambda_{\mathrm{sf}} \approx$

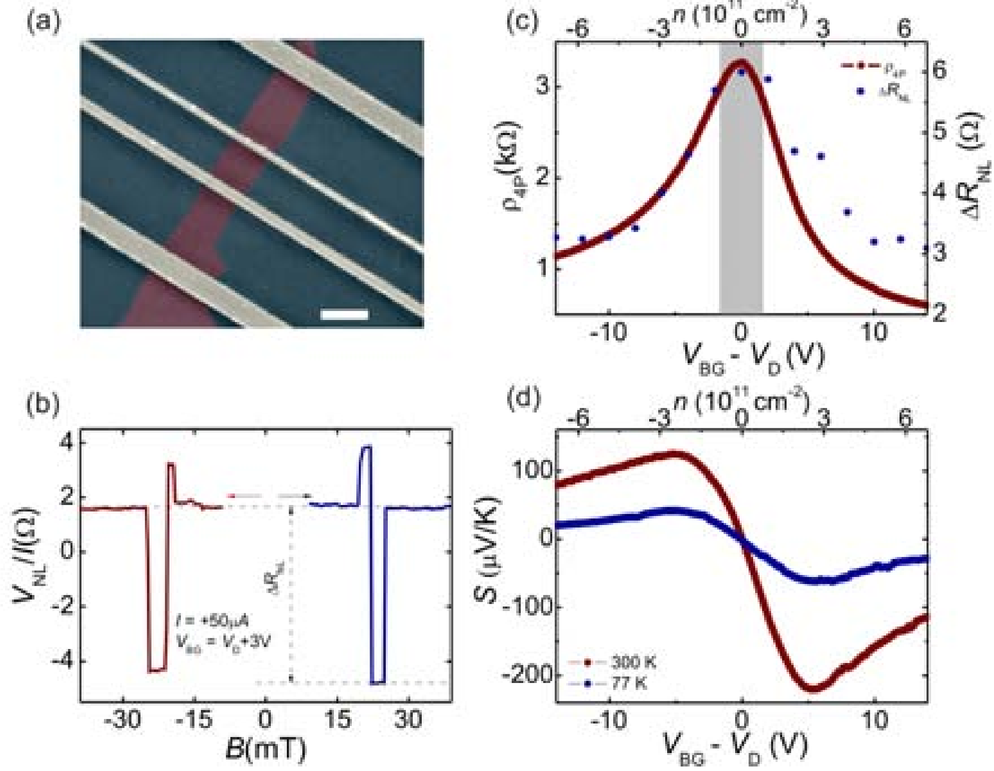


Figure 7.3.: Characteristics of sample Q1 (a) SEM image of the device. The scale bar equals 1 $\mu$m. Graphene is exfoliated on a PMMA substrate and four Co electrodes are deposited on top (b) NLSV measurement for $I = 50\,\mu$A, $\Delta R_{\mathrm{NL}} \approx 7\,\Omega$ (c) Four point resistivity $\rho_{4\mathrm{P}}$ (left vertical axis) and transresistance $\Delta R_{\mathrm{NL}}$ for $I = 10\,\mu$A (right vertical axis) as function of $V_{\mathrm{BG}}$. The grey area represents the residual carrier concentration of the device. (d) Seebeck coefficient $S$ at room temperature and 77 K according to the Mott formula

1.2 $\mu$m at the Dirac point, while for other backgate voltages, $\lambda_{\mathrm{sf}}$ can be as high as 2 $\mu$m, as shown in Fig. 7.4. With this, we are able to extract the interfacial current polarization $P_J$, finding that $P_J \approx 5\,\%$.

### 7.3.2. Non Local IV Measurements

We present the main results throughout the following section. Studying the bias dependence of our devices, we observe a supralinear dependence of the electrochemical potentials of the spin sub bands on the applied bias current $I$. Moreover, we demonstrate that close to the Dirac point, the carriers in the spin up band are electrons, while the spin down carriers are holes, which corresponds to the idealized spin thermocouple described in section 7.2.

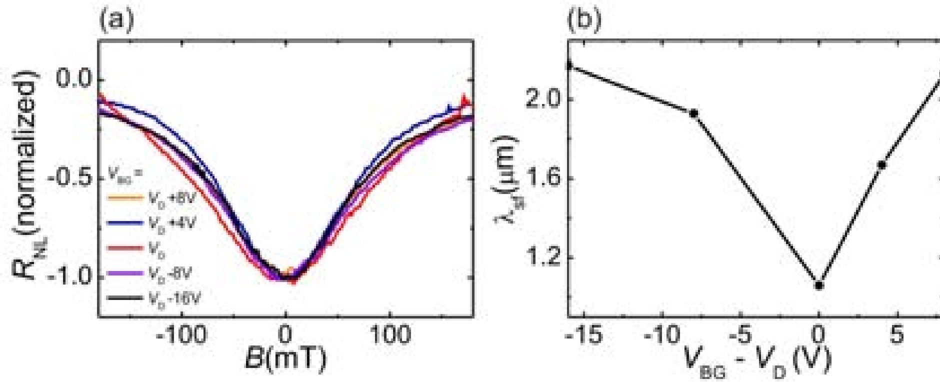


Figure 7.4.: (a) Hanle spin precession in the anti parallel alignment of the FMs for different backgate voltages (b) Fitting the curves in (a) to a two dimensional model delivers $\lambda_{\mathrm{sf}}$, which shows a minimum at the Dirac point of graphene of $\lambda_{\mathrm{sf}} \approx 1.2\,\mu\mathrm{m}$.

The experimental data is shown in Fig. 7.5. It consists of the non local voltage $V_{\mathrm{NL}}$ as function of the bias current for P and AP alignment of the FMs for three different backgate voltages. These voltages correspond to the Dirac point of graphene as well as one point above and one below it, $V_{\mathrm{BG}} - V_{\mathrm{D}} = 0, \pm 4\,\mathrm{V}$. The dashed line indicates the mean non local voltage $V_{\mathrm{th}}$, which exhibits a parabolic behavior as a function of the current, as expected of a thermoelectric voltage.

We perform the measurements as follows: First, we prepare the P or AP configuration of the injector/detetector FMs in a NLSV measurement by exploiting the memory effect of our devices [94], then we sweep the magnetic field back to zero. Second, in these two states we subsequently measure the non local voltage $V_{\mathrm{NL}}$ as a function of the injected current. In principle, this constitutes a conventional $IV$ measurement, but in the non local configuration shown in Fig. 7.2. We therefore refer to this technique as non local $IV$ (NLIV) measurements. Finally, we repeat the NLIVs for different voltages applied to the backgate, thus varying the carrier concentration, the type of carriers and the conductivity of graphene. We have confirmed the validity of our approach by performing several single NLSV measurements for varying currents and gate voltages.

The NLIVs shown in 7.5 (a) are measured at a backgate voltage of $V_{\mathrm{BG}} - V_{\mathrm{D}} = -4\,\mathrm{V}$. The splitting between $V_{\mathrm{P}}$ and $V_{\mathrm{AP}}$ increases with the bias current, as the splitting of spin up and down band increases. The backgate voltage $V_{\mathrm{BG}}$ shifts the position of the Fermi energy $E_{\mathrm{F}}$ relative to the charge neutrality point. The density of states for both spin sub bands is schematically shown by the Dirac cones in the inset. Here, the carriers in both spin sub bands are holes and the sign of the parabolic coefficient of the NLIVs is negative for both relative alignments of the FMs.

Close to the Dirac point of graphene, as shown in Fig. 7.5 (b), the Fermi level of the spin up band lies above the Dirac point, while the Fermi level of the spin down band lies

below it. Therefore, the carriers in the spin up band are electrons, while the carriers in the spin down band are holes. The detected non local voltages for P and AP alignment of the FMs $V_P$ and $V_{AP}$ have different signs and parabolic coefficients for each case. The thermoelectric voltage $V_{th}$ is close to zero, as the sign of the carriers is opposite for the P and AP alignment and both contributions cancel each other out, in agreement with our expectations.

In Fig. 7.5 (c), the voltage applied to the backgate is $V_{BG} - V_D = +4\,V$, meaning that the carriers in both sub bands are electrons and the sign of the parabolic coefficient is positive.

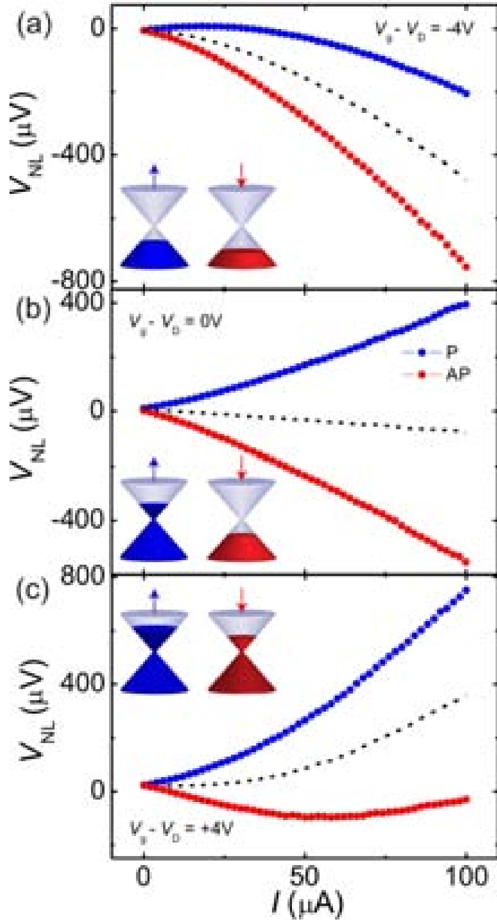


Figure 7.5.: Non local voltage $V_{NL}$ for different gate voltages as function of the bias. The carriers in the spin sub bands are (a) holes (b) electrons for spin up, holes for spin down (c) electrons.

It becomes clear that the device corresponds to the spin thermocouple we describe in section 7.2. At the Dirac point, spin up and spin down currents consist of opposite type of carriers. Consequently, the thermal enhancement of $\mu_S$ is largest close to the Dirac point. Moreover, a correlation between the type of carrier and the type of spin exists in this situation, which is not only intriguing from a physics point of view, but also important for possible spin caloritronical applications.

To further investigate this point, we study $\Delta V_{NL}$ and $\Delta R_{NL}$ as a function of the bias current, as shown in Fig. 7.6. The largest spin accumulation is detected at the Dirac point, $V_{BG} = V_D$, with absolute values of $V_{NL}$ close to 1 mV for a bias current of 100 $\mu$A. Taking into account the interfacial current polarization of approx. 5 %, in terms of electrochemical potentials this corresponds to $\mu_s = 20\,\text{meV}$. In all three cases, $\Delta V_{NL}$ shows a supralinear behavior as a function of the current, as shown in Fig. 7.6 (a). This is especially remarkable, because $\Delta V_{NL}$ typically decays for increasing bias currents [94]. Here, it increases due to the thermal enhancement of the signal, which gains weight as the

bias, and thus the temperature gradient along the sample, increases.

At the Dirac Point, $\Delta R_{\mathrm{NL}}$ is close to $5\,\Omega$ at low currents, but increases up to $\sim 10\,\Omega$ at $I = 100\,\mu$A, as shown in Fig. 7.6 (b). It can also be seen that $\Delta R_{\mathrm{NL}}$ has roughly the same dependence on the bias current $I$, if the carriers in the two spin sub bands are either both electrons or holes, for $V_{\mathrm{BG}} - V_{\mathrm{D}} = \pm 4\,$V. $\Delta R_{\mathrm{NL}}$ increases almost linearly for currents above approx. $50\,\mu$A, and $d\Delta R_{\mathrm{NL}}/dI \approx 10\,\mathrm{mV/mA^2}$ for $V_{\mathrm{BG}} - V_{\mathrm{D}} = \pm 4\,$V. At the Dirac point, $d\Delta R_{\mathrm{NL}}/dI \approx 25\,\mathrm{mV/mA^2}$.

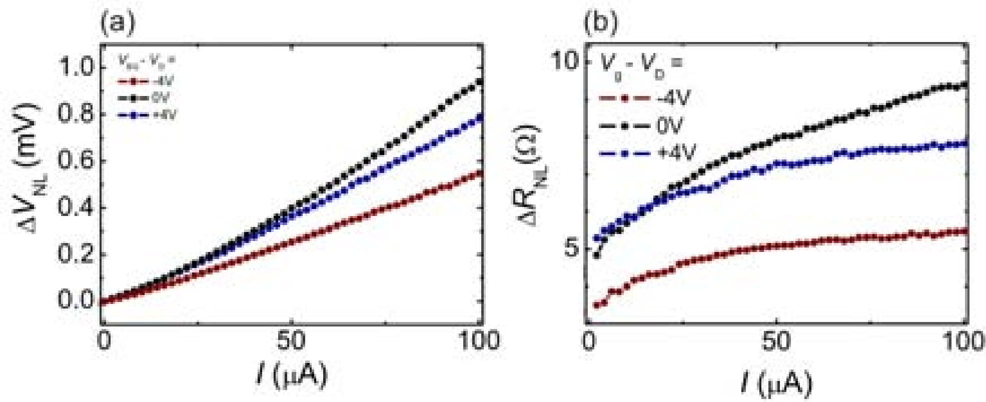


Figure 7.6.: The spin signal $\Delta R_{\mathrm{NL}}$ for the curves presented in Fig. 7.5. The transresistance increases with increasing bias in all cases. The highest values of $\Delta R_{\mathrm{NL}}$ are reached at the Dirac point of graphene.

An increase in $R_{\mathrm{NL}}$ with increasing bias is a feature which cannot be explained within the phenomenological model of spin injection. In systems using transparent contact, $\Delta R_{\mathrm{NL}}$ is independent of the bias current, according to eq. 2.32. Also in systems using tunneling barriers, $\Delta R_{\mathrm{NL}}$ is independent of the current, as given by eq. 2.34. However, these equations are only valid in the low current regime, as a bias dependence is not considered within the model.

Experimentally, a decrease is observed in most systems [94]. Moreover, as we discuss in detail in chapter 4, the spin polarization in magnetic tunnel junctions quickly deteriorates as a function of the bias current. As shown there, this is due to intrinsic properties of the tunneling process of the carriers, therefore limiting the highest absolute values of $V_{\mathrm{NL}}$.

Additionally, in graphene, due to monotonous increase in the density of states away from the Dirac point, a decaying spin signal $R_{\mathrm{NL}}$ can be expected, regardless of the type of contact.

Nevertheless, examples of linear or even supralinear behavior of the spin signal as a function of the bias can be found in the literature. In transparent contact graphene spin valves, Shiraishi *et al.* have reported a linear relationship between non local voltage and bias current, which holds up to $I = 1\,$mA [147]. Again in transparent contact devices, Han *et al.* report on an electron hole asymmetry of spin injection,

observing a supralinear increase when the carriers in their devices are holes [163]. In that case, $\Delta R_{\mathrm{NL}}$ increases for a factor 1.25 from $\sim 40\,\mathrm{m}\Omega$ at currents close to zero to $\sim 50\,\mathrm{m}\Omega$ at $I = 200\,\mu\mathrm{A}$. In our case, the increase at the Dirac point is close to a factor two for currents between 0 and $100\,\mu\mathrm{A}$.

### 7.3.3. Analysis of the Data

#### The Polynomial model

In order to investigate the response of our devices to varying types of carriers and conductivities, we have measured several NLIVs, such as the ones shown in Fig. 7.5 for different backgate voltages. We analyze the data with a polynomial model, which allows for a better understanding of the different contributions to the spin signal. In a first approach, the pure spin current is a first order and the heat current a second order effect in respect to the bias current.

We describe the NLIVs for P and AP configuration by

$$V_{\mathrm{NL}} = V_0 + r_{\mathrm{NL}} I + \Sigma I^{\gamma} \tag{7.1}$$

For $\gamma = 2$, this corresponds to a simple polynomial model up to the second order, which is in good agreement with the data ($\chi^2 \geq 99\,\%$). A previous study has focused on the role of the second order parameter [164]. However, a recent result [165] suggests that a complete analysis of the process requires values of $\gamma$ deviating from 2.

The parameters of the different orders within eq. 7.1 are spin dependent. For instance in case of P alignment of the FM, the equation reads $V_{\mathrm{NL}}^{\uparrow} = V_0^{\uparrow} + r_{\mathrm{NL}}^{\uparrow} I + \Sigma^{\uparrow} I^{\gamma}$. We further consider $\Delta V_{\mathrm{NL}} = V^{\uparrow} - V^{\downarrow}$, which is the conventional definition of $\Delta V_{\mathrm{NL}}$, and $V_{\mathrm{NL}} = (V^{\uparrow} + V^{\downarrow})/2$. These definitions are equal for all parameters, e.g. $\Sigma = (\Sigma^{\uparrow} + \Sigma^{\downarrow})/2$ and so on.

The contribution to the spin signal of the different orders of eq. 7.1 can be understood as follows:

- The parameter $V_0$ is a constant offset, which is typically of the order of $1\,\mu\mathrm{V}$ and which we neglect in the following.
- The first order parameter $r_{\mathrm{NL}}$ corresponds to the conventional definition of the transresistance, if $V_0 = \Sigma = 0$. This means that in the absence of an offset voltage $V_0$ and higher order effects, $\Delta r_{\mathrm{NL}} = \Delta R_{\mathrm{NL}}$.
- The higher order contribution $\Sigma I^{\gamma}$ can be understood in the following way. Consider heat transport in a non magnetic system, where no spin current and no linear contribution to the non local signal is present, $r_{\mathrm{NL}} = 0$. However, due to Joule heating of the injector contact, a Seebeck voltage can be measured at the detector, which is given by $V_{\mathrm{NL}} = V_{\mathrm{Seebeck}} = -S\Delta T^{c}$, if the Seebeck coefficient $S$ is not

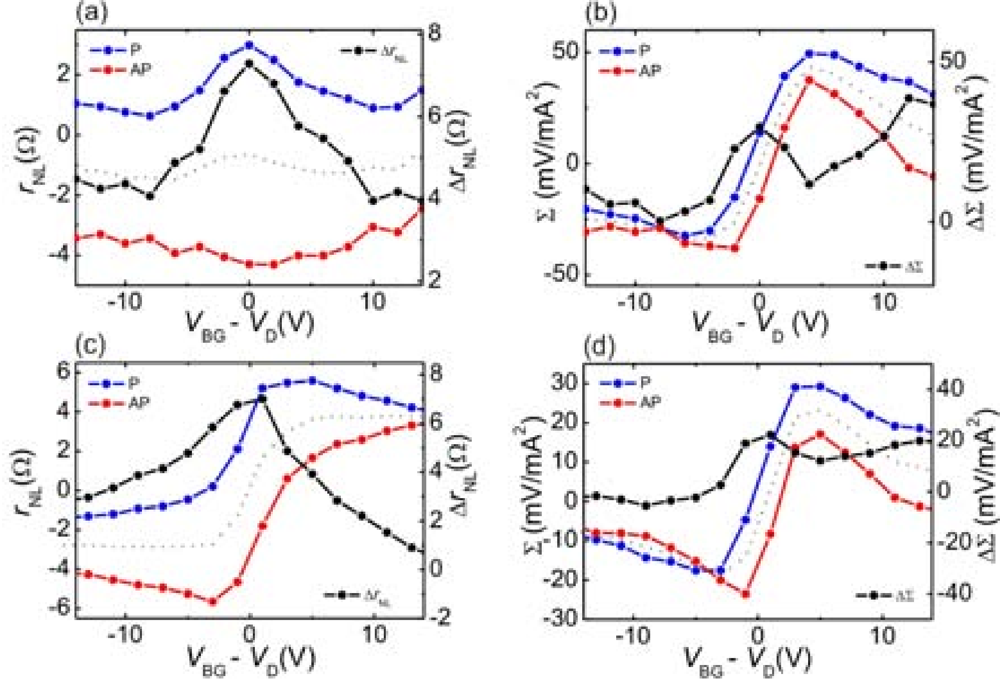


Figure 7.7.: Results of our analysis (a) First order fitting parameter $r_{\mathrm{NL}}$ for P and AP alignment as a function of $V_{\mathrm{BG}}$ at room temperature (b) Second order fitting parameter $\Sigma$ corresponding to the analysis in a) (c) First order fitting parameter $r_{\mathrm{NL}}$ as a function of $V_{\mathrm{BG}}$ at 77 K (d) Second order parameter $\Sigma$ at 77 K

or only weakly temperature dependent. It follows that $\Sigma I^2 = V_{\mathrm{NL}} = -S\Delta T^c$. This is the classical relation 2.3 of the Seebeck effect. Here, $\gamma = 2$ and $\Sigma \propto S$.

Now we consider a current consisting of spin up and spin down particles. Within the two-current model, this means that $V^{\uparrow,\downarrow} = -S^{\uparrow,\downarrow}\Delta T^c$. Therefore, if $S^{\uparrow} \neq S^{\downarrow}$, the higher order contribution of the non local voltage is spin polarized. It can be expressed as $\Delta\Sigma I^{\gamma} = -(S^{\uparrow} - S^{\downarrow})\Delta T^c$, which is the general expression for the anomalous enhancement of the spin signal as introduced in section 7.2.

The power of $I$, $\gamma$, is therefore determined by two different contributions, $\Delta S = (S^{\uparrow} - S^{\downarrow})$ and $\Delta T^c$.

Close to the Dirac point, the Seebeck coefficient is linear with respect to the backgate voltage. It follows that also the the contribution to the spin signal due to $\Delta S = (S^{\uparrow} - S^{\downarrow})$ is linear with respect to the current, $\Delta S \propto I$.

The relation between current and temperature also contributes to $\Sigma I^{\gamma}$. The classical, well known relation is Joule heating, where $\Delta T \propto I^2$. However, in a recent work, Betz *et al.* find a linear relation between current and carrier temperature at low bias, $T^c \propto I$, and $T^c \propto I^{1/2}$ otherwise, due to the presence

of hot carriers induced by the bias [165].

Taking into account all contributions, it becomes clear that $1.5 \leq \gamma \leq 3$. We find that the data is well described by $\gamma = 2$ in eq. 7.1 in all cases, thus favoring $T^c \propto I$.

In short, $r_{\rm NL} \sim R_{\rm NL}$, while $\Sigma \sim S$. Therefore, $\Sigma$ shows a Seebeck-type behavior as a function of the backgate, and $\Delta\Sigma$ is proportional to the derivative of the Seebeck coefficient, as $\Delta S \propto dS/dV_{\rm BG}$.

**Results of the Analysis**

Figure 7.7 shows the results of the analysis of data obtained at room temperature as well as at 77 K.

The first order contribution as a function of backgate voltage $V_{\rm BG}$ gives an indication that the carriers injected into graphene have tunneling like properties, since $\Delta r_{\rm NL}$, shown in Fig. 7.7 (a), exhibits a peak at the Dirac point of graphene. For the conventional spin signal $\Delta R_{\rm NL}$ this is expected if the device has highly resistive contacts, where $\Delta R_{\rm NL} \propto R_{\rm 4P}$ [135]. One can also expect that at low injection currents, any higher order effects are negligible, which is the case here. In Fig. 7.3 (b), we compare $\rho_{\rm 4P}$ and $\Delta R_{\rm NL}$, where $\Delta R_{\rm NL}$ is measured using a DC current of 10 $\mu$A. At currents as low as a few $\mu$A, $\Delta R_{\rm NL} \approx \Delta r_{\rm NL}$.

Also at low temperatures, $\Delta r_{\rm NL}$ exhibits a peak at the Dirac point of graphene, as shown in Fig. 7.7 (c).

The second order parameters $\Sigma^{\uparrow,\downarrow}$ at room temperature are shown as a function of the backgate voltage $V_{\rm BG}$ in Fig. 7.7 (b). The dashed line indicates $\Sigma = (\Sigma^{\uparrow} + \Sigma^{\downarrow})/2$, which is in qualitative agreement with the Seebeck coefficient of graphene, as shown in Fig. 7.8. Rescaling $\Sigma$ by using the relation between bias current and temperature difference obtained by the numerical simulation, we can convert $\Sigma^{\uparrow,\downarrow}$ to the spin dependent Seebeck coefficients of graphene $S^{\uparrow,\downarrow}$. This is demonstrated in detail in appendix B.4.

While $\Sigma$ is proportional to $S$, the anomalous enhancement of the spin accumulation is proportional to $\Delta\Sigma$ and thus $\Delta S$. In fact, $\Delta\Sigma$ as given by the polynomial model corresponds to the derivative of $\Delta R_{\rm NL}$ with respect to the current $I$. This follows from the definition of the model, where $\Delta R_{\rm NL} = \Delta r_{\rm NL} + \Delta\Sigma \cdot I$ and thus $d\Delta R_{\rm NL}/dI = \Delta\Sigma$. We can therefore obtain $\Delta\Sigma$ by fitting the NLIVs with the polynomial model, or by numerically differentiating $\Delta R_{\rm NL}(I)$, as in section 7.3.2.

Since $d\Delta R_{\rm NL}/dI$ is constant over a considerable range of currents, the difference between the two methods is negligible and the values extracted from the curves shown in Fig. 7.6 (b) correspond well with the values of $\Delta\Sigma$ obtained from the fitting, as shown in Fig. 7.7.

At 77 K, as shown in Fig. 7.7 (d), the values of $\Sigma^{\uparrow,\downarrow}$ and $\Delta\Sigma$ are smaller than at room temperature. This is due to the fact that many material parameters of the

system, such as the thermal conductivity or specific heat of graphene are smaller than at room temperature [28]. Especially, $S(77\,\mathrm{K}) < S(300\,\mathrm{K})$, as shown in Fig. 7.3 (d), and thus also $\Sigma$ and $\Delta\Sigma$ are smaller than at room temperature.

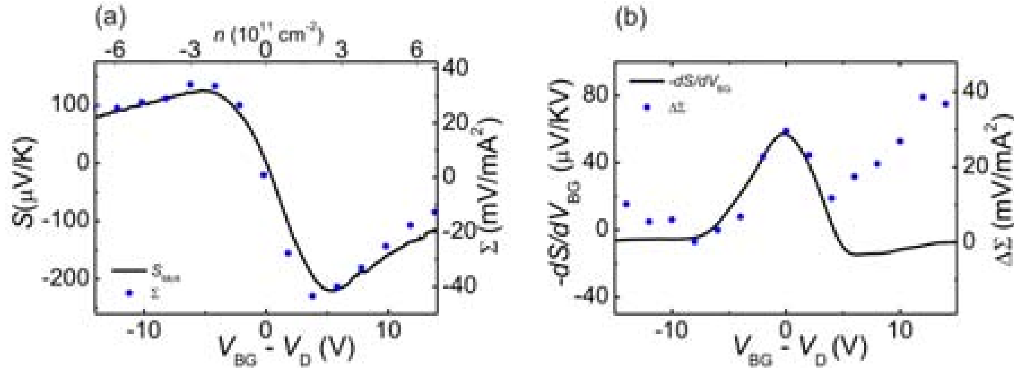


Figure 7.8.: (a) Seebeck coefficient of the device according to the Mott formula in comparision with the second order parameter $\Sigma$ (b) Both $-dS/dV_{\mathrm{BG}}$ as well as $\Delta\Sigma$ exhibit a peak around the Dirac point of graphene

A comparision between $S_{\mathrm{Mott}}$ and $\Sigma$ is shown in Fig. 7.8 (a). In fact, they exhibit the same behavior as a function of the backgate voltage $V_{\mathrm{BG}}$. This can be used in order to obtain a conversion factor between Seebeck coefficient and second order fitting parameter. Here, we obtain $1\,\mathrm{mV/mA}^2 \approx 5\,\mu\mathrm{V/K}$.

In Fig. 7.8 (b), a comparision between $-dS/dV_{\mathrm{BG}}$ and $\Delta\Sigma$ is shown. Again, the curves exhibit qualitative agreement. Moreover, the reason for the peak in $\Delta\Sigma$ around the Dirac point becomes clear. As noted above, within the polynomial model, $\Delta\Sigma = d\Delta R_{\mathrm{NL}}/dV_{\mathrm{BG}}$, meaning that $\Delta\Sigma$ is a measure of the variation of $\Delta R_{\mathrm{NL}}$ with the bias current. Since $-dS/dV_{\mathrm{BG}}$ has a peak around the Dirac point, this implies that at $V_{\mathrm{D}}$, the strongest enhancement of the non local signal with the bias can be found.

Altogether, our analysis demonstrates that due to the spin dependency of the second order parameter $\Sigma$, we observe the anomalous enhancement of the non local voltage, which is most pronounced at the Dirac point of graphene.

### 7.3.4. Hot Carriers

While the analysis of the NLIVs based on the polynomial model delivers a qualitative description of our observations, a discrepancy becomes apparent when trying to obtain quantitative results.

The enhancement of the non local signal can be expressed as $\Delta\mu_S = e\Delta S\Delta T$. While we obtain $\Delta\mu_S$ and $\Delta S$ experimentally, we extract $\Delta T$ from the numerical calulation of the temperature profile of the sample. However, the numerical simulation delivers the temperature of the lattice, which can differ from that of the carriers.

At room temperature, it becomes obvious that the lattice temperature is at least one order of magnitude lower than the temperature required by $\Delta\mu_S = e\Delta S\Delta T$. At lower temperatures such as 77 K, the discrepancy is even more pronounced. We find that values of $\Delta T$ of several hundred Kelvin would be required, implying device temperatures of several thousands of Kelvin.

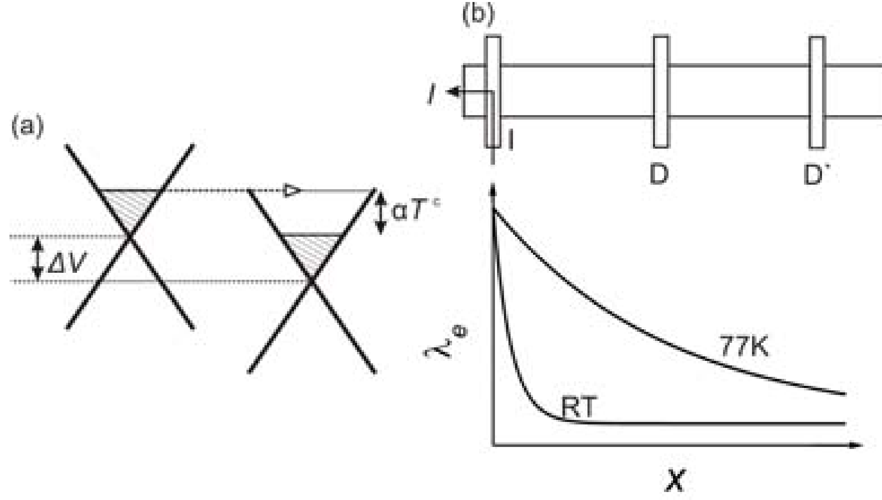


Figure 7.9.: Schematical representation of the physics of hot electrons (a) Schematic representation of the Fermi levels of graphene close to the point of injection and close to the point of detection. (b) Schematic representation of the device and the decay of hot carriers in graphene. At room temperature, the injected, highly energetic carriers quickly thermalize with the lattice, while at 77 K, they reach the two detectors.

We conclude that the numerical model underestimates the temperature of the carriers $T^c$, which might be higher than the temperature of the lattice $T^l$. This conclusion is in agreement with a recent study, where electronic temperatures $T^e$ of up to 1200 K in graphene have been reported [166]. In the following, we simply refer to these carriers, whose energy is considerably higher than that of the lattice, as hot carriers. They thermalize with the lattice via scattering processes, most importantly via disorder assisted scattering, which has been studied in graphene recently [167].

The existence of hot carriers at the point of detection can be explained by the low density of impurities of our devices and the large electric fields. As carriers are accelerated, they gain kinetic energy, which they loose by inelastic scattering with phonons. Because intrinsic optical phonons, which interact strongly with carriers, have an energy ~200 meV, the relaxation for lower energies is slow. Therefore, the carriers arrive at the detector with an energy exceeding the thermal energy for an amount proportional to the temperature of the carriers, $E \propto T^c$, as schematically shown in Fig. 7.9 (a).

In Fig. 7.9 (b), a sketch of the sample is shown together with a simulation of the mean free path $\lambda_e$ of the hot carriers as a function of the lateral distance from the point of injection, based on Ref. [167]. The carriers are injected into graphene at $x = 0$, while the non local voltage $V_{\mathrm{NL}}$ is detected between the detectors D and D′. For our analysis, we therefore have to take into account the temperature difference $\Delta T_{\mathrm{DD'}}$ between the two detectors as well as $\Delta T_{\mathrm{ID}}$ between injector and first detector, and depending on the situation, we have to choose between $\Delta T_{\mathrm{ID}}$ and $\Delta T_{\mathrm{DD'}}$.

For instance, when comparing $V_{\mathrm{th}}$ and $S$, it is valid that $-V_{\mathrm{th}}/\Delta T_{\mathrm{DD'}} = S$, since $V_{\mathrm{th}}$ is detected between D and D′. On the other hand, the higher order contribution to the spin signal is given by the spin dependent $S$ the carriers experience while traveling from injector I to first detector D. This means that $\Delta\mu_S = e\Delta S\Delta T_{\mathrm{ID}}$.

As shown by Song *et al.* [167], the lifetime of hot carriers decreases as the temperature increases, since they thermalize via disorder assisted scattering events. Therefore, at room temperature, $\Delta T_{\mathrm{DD'}} \approx \Delta T_{\mathrm{DD'}}^{\mathrm{lattice}}$. This is supported by the fact that using $\Delta T_{\mathrm{DD'}}$ obtained by the numerical calculation, which delivers the temperature of the lattice, in $-V_{\mathrm{th}}/T_{\mathrm{DD'}} = S$ results in a Seebeck coefficient of graphene which is in good agreement with the values reported in the literature [27, 162].

However, even at room temperature $\Delta T_{\mathrm{ID}} \neq \Delta T_{\mathrm{ID}}^{\mathrm{lattice}}$. Therefore, when trying to quantify our results via $\Delta_2\mu = e\Delta S\Delta T$, as shown above, we observe a discrepancy of one order of magnitude.

The discrepancy is even larger at low temperatures such as 77 K. As schematically shown in Fig. 7.9 (b), at 77 K also $\Delta T_{\mathrm{DD'}} \neq \Delta T_{\mathrm{DD'}}^{\mathrm{lattice}}$, which has to be taken into account when analyzing the data.

Apart from the quantitative discrepancies, a strong indication for the presence of hot carriers in our experiments can be found in the analysis of the data, namely in Fig. 7.7 (c). As pointed out, at low temperatures there is a linear relationship between $T^c$ and $I$ [165]. This means that the Seebeck effect becomes a first order effect with respect to the current, $V_{\mathrm{Seebeck}} \propto I$. In fact, the first order contribution to the non local signal at 77 K exhibits a Seebeck like backgate dependence, which is not observed at room temperature.

## 7.4. Conclusion

In conclusion, we have shown that in graphene the combination of spin currents with its energy dependent mobility and density of states can result in novel phenomena in spin caloritronics. We demonstrate that graphene non local spin valves can act as spin thermocouples, when a sizeable Joule heating is generated. A thermal gradient between injector and detector results in large thermoelectric spin voltages. The difference between the electrochemical potential of spin up and spin down electrons reaches 20 meV and is of the order of typical electronic density distributions of carriers in graphene. Therefore, the coexistence of a large quantity of carriers with electron and

hole character with opposite spin polarization becomes possible. This is reflected in an anomalous increase of the non local spin signal at the Dirac point as a function of the current bias. Our observations suggest that the transport of spin information in ultra clean graphene could be sustained by thermal transport over macroscopic distances, where spin signal relaxation is partially compensated by thermal transport.

# 8. Conclusions

The main topic of this thesis is the study of pure spin and heat currents in graphene non local spin valves via means of electrical spin injection and detection. In a preliminary work, we analytically investigate the tunneling process of conduction electrons between ferro- and non magnetic materials. On the experimental side, we report on electrical detection of spin precession in freely suspended graphene spin valves. In this context, we have developed a novel method for the fabrication of freely suspended graphene devices, which additionally is beneficial for the spin injection/detection efficiency of the devices. In order to investigate these enhanced spin signals, we have performed bias dependent measurements, which ultimately lead to the experimental demonstration of a spin thermocouple in graphene.

In order to further investigate tunneling of conduction electrons between ferro- and non magnetic electrodes, we have developed a theoretical model based on the analytical solution of the one-dimensional, time-independent Schrödinger equation. Focussing on the bias dependence of the spin polarization, we predict a change in sign of the polarization when tunneling takes place from FM to NM.

More importantly, the model shows that a complex behavior of the polarization is intrinsic to the tunneling process of electrons.

Due to its low spin orbit coupling, long spin relaxations times of several tens of $\mu$m in graphene have been predicted. A promising approach to study the intrinsic properties of graphene is to suspend the flakes, thus eliminating the influence of the substrate and enabling cleaning methods which help removing impurities and contamination.

In order to achieve this, we have developed a method to fabricate freely suspended graphene non local spin valves that involves a minimal number of steps and chemicals. It is based on the process of crosslinking the polymer PMMA, which is carried out by overexposure of the polymer by electron beam radiation. We have carried out extensive efforts in order to ensure the feasibility of the method, including characterization via optical, electron beam and atomic force microscopy.

Since the method is acid free, the yield of high quality, as-processed devices is notably improved when comparing to the standard fabrication process, which requires agressive chemicals such as hydrofluoric (HF) acid. However, further improvements in terms of mobility can be expected by employing post processing cleaning methods. These include annealing in an Hydrogen/Argon environment as well as current-induced cleaning. Nevertheless, our as-processed devices exhibit excellent mobility, which can

be as high as $2 \times 10^4\,\mathrm{cm^2V^{-1}s^{-1}}$ at room temperature.

We demonstrate electrical detection of spin preccesion, allowing us to extract the spin relaxation length in these devices, finding values of a few $\mu$m. This is similar to the values obtained in non suspended devices of lower mobility, in contrast to the theoretical predictions. Therefore, it seems that these early predictions have overlooked limiting factors for the spin relaxation length in graphene. To date, no explanation for the discrepancy has been given.

We expect that by applying cleaning methods to freely suspended spin valves, it will be possible to obtain ultra high mobility samples, therefore opening the path to investigating the origins of spin relaxation in intrinsic graphene.

Moreover, the properties of graphene under the influence of external strain have received much attention recently. In this context, freely suspended spin valves are natural candidates for the investigation of pseudomagnetic fields in strained graphene. While many theoretical studies of this topic are available, experimental data is relatively scarce.

Besides studying mechanisms of spin relaxation, we have observed an enhanced spin injection/detection efficiency in our devices. In order to investigate the origins of the enhancement, we have fabricated samples on PMMA and $SiO_2$ substrates. In both cases, we observe the enhanced spin accumulation, which we attribute to the formation of an amorphous carbon (aC) layer at the interface between graphene and ferromagnet due to electron beam induced deposition. Because of the low atomic weight of carbon, the dephasing of spins in the barrier is low, making aC an excellent choice for applications in spintronics.

The interfaces are stable even for large applied bias current densities. We obtain a $10^4$ enhancement of the spin signal as compared to Ohmic contacts, but expect further increase after optimizing the depostion method. While the $IV$ characteristics of the devices are almost linear, the increased contact resistance and spin accumulation suggests that the interface could be a combination of Ohmic and tunneling properties.

The simplicity and transferability of the fabrication process is in contrast to those of $Al_2O_3$ or MgO tunneling barriers, which are the conventional insulators used in spintronics. Therefore, we expect that aC barriers are a viable alternative, which might not only improve the spin injection/detection in non local spin valves in graphene, but in other materials as well.

Finally, we have performed bias dependent measurements in our samples, observing a novel phenonenom which is due to the particular properties of graphene such as its energy dependent mobility and density of states. We demonstrate an anomalous enhancement of the spin accumulation at the Dirac point, which is caused by Joule heating in the injector contacts and the resulting thermal gradient and thus increases with the bias.

Because of this quadratic contribution to the spin accumulation, the electrochemical

potentials of the spin sub bands exhibit supralinear behavior as a function of the bias current. The spin splitting becomes so large, of the order of 20 meV, that at the Dirac point we observe a huge quantity of spin up carriers with electron and spin down carriers with hole caracter, simultaneously. We show that this constitues a spin thermocouple, where the two arms of the device are formed by the different types of spin in a single graphene sheet and the thermoelectric voltage between spin up and spin down contributes to and thus enhances the total spin accumulation.

# 9. Acknowledgements

As it is good tradition, I would like to acknowledege the help I received from many persons during the past five years and express my gratitude to everybody.

First of all, I would like to thank my PhD supervisior, Sergio Valenzuela, for providing me with the opportunity to work at the ICN in Barcelona. I especially appreciate the huge amount of freedom I enjoyed when it came to sample fabrication and conducting measurements. Sergio is certainly one of the best physicists I met, so he has been a great guide and at the same time, I always felt it was a great honour for me to write my PhD thesis in his newly founded group. Beside all these things concerning the work at the institute, I will not forget the unconditional support I experienced from Sergio when I had a hard time after a bicycle accident, which forced me to take a break from my PhD for several months. Especially this kind of support cannot be taken for granted. Thanks for everything, Sergio!

Then, of course, there are the members of the group I got to know over the years. In the beginning, I learned nearly in the lab everything from Marius Costache, how to make samples and especially how to measure them. I still havent´t met anybody who measures as thorough as he does. Marius also told me that ‘If you know how to cook, you know how to make samples‘. I really like that sentence, as it contains a real lesson.

German Bridoux was another great colleague, who joined somewhat later and he was providing heart and soul to the group. He took care of the voluntary work nobody volounteers for and generally was helpful in every aspect. Even though he already left the group, German has proven extremely helpful in proofreading this thesis.

With Juan Sierra, we started talking Spanish in the group which is quite an achievement. Since he also joined the graphene project, I had many fruitful discussions with him. As German, Marius and Sergio, he was very helpful in proofreading my thesis and giving me critical comments, especially any time I mentioned GMR.

Finally, I would like to thank Joris Van de Vondel, with whom I started to work on graphene after spending the first year of my PhD with nanowires. Joris is still the undisputed master of the Scotch tape, so thanks a lot for teaching me how to do it.

There have been many colleagues from other groups, whose help I would like to acknowledge. Maria Josè Esplandiu has been very helpful in questions concerning sample fabrication. Moreover, I especially respect her for her unshakable professionalism amongst the every day chaos of the institute.

From Adrian Bachtold´s group, I owe the biggest thanks to Joel Moser. When Joris and me started exfoliating graphene, he generously showed us all the little tricks and details we needed to know. Johannes Güttinger was very helpful in discussing our results and providing me with a Matlab script for the analysis. I would also like to thank Peter Weber, Ioannis Tsioutsios, Marianna Sledzinska and Daniel García for fruitful discussions regarding sample fabrication and analysis.

From Pietro Gambardella´s group I would like to thank Corneliu Nistor for the Helium, which came just at the right time for me, even though the measurements did not make it into this thesis. From the group of Clivia Sotomayor Torres, I would like to thank Françesc Alzina for the help with the Raman measurements, and also for letting us use the nitrogen vessel for such along time. I would also like to thank Clivia herself, who shared some of her time in order to give me valuable advice regarding the german universitarian system. Many Thanks also to Stephan Roche for making sure UI would not miss the Graphene conference in Bilbao in 2013.

As mentioned above, I had started my PhD working with nanowires grown in the group of Victor Puntes by Miriam Varón, I would like to express my gratitude for the collaboration. Miriam also gave me some helpful advice regarding the PhD procedures at the Autònoma.

Then there are the many employees of the ICN, the UAB and the CNM, who made their contribution.

I would like to thank Xavi Ros and Carlos from maintainence, who we could rely on if something in the lab needed fixing, which was quite frequent. In the CNM clean room, I had the pleasure of working on the excellent nanolithography system kept in shape by Xevi Borrisè, and when he was absent, by Jordi Llobet, who also helped me use the focused ion beam system. On the occasions I had to use the clean room of the UAB, Maria Angeles Benítez and Raquel Palencia have been so kind as to give us a hand whenever we needed the facilities.

I would like to thank Belen Ballesteros and Marcos Rosado of the electron microscopy department, who helped in taking TEM or other special images. Whenever we needed to contact a workshop, or draw technical designs, or order mechanical pieces for the laboratory, Gustavo Ceballos was the man with the connections and also helping with the technical drawings.

Then there were the people in administration. I apologize if I forget somebody, there are just so many. Thanks a lot to Rosa Juan, Anabel Rodríguez, Marta de la Osa, Sandra Domene, Laura Camarero, Inma Caño, Matias Pueyo, Lluis Bellafont and also Oscar Cardenal, Oliver Fernandez and Manfred Hoeflich from IT.

Last but not least, my special thanks to the former boss of the institute, Jordi Pascual, who had the talent of giving everybody, even the most miserable of PhD students, the feeling of being an important part of the ICN. Moreover, he also accepted the responsibility to act as the tutor of my thesis and generally did a great job at the ICN. Without him, I doubt the institute would be where it is now.

Finally, I would like to thank the members of my PhD committee, Luis Hueso, Xavier Cartoixa, Laurent Vila, Teresa Puig and Stephan Roche for the effort of reading my thesis and attending the defence.

Next I would like to acknowledge the help I received from people outside of the university whose support might not have had a direct impact on muy thesis, but which was important for me nevertheless. I will just use the language most fitting to the person from now on.

En primer lugar, quiero dar las gracias a mi esposa, Miriam Jiménez Berruezo. No puedo agradecerte lo suficiente por tu cariño, tu comprensión y el apoyo que me demuestras todos los días.

He tingut molta sort de tenir un amic com el Jordi, qui em va portar a tots els llocs no turístics de Barcelona, i va fer una gran contribució en fer-me sentir benvingut aquí. Vaig perdre el compte de quantes vegades hi vam anar a veure el clàssic juntament amb al Dani.

Siempre fui bienvenido en la casa de Cris, Manolito y Berta. Manolito fue de las pocas personas que fuera del instituto se interesaba por mi investigación. Otra pareja que que me recibió a menudo en su casa fueron Loli y Toni, y Toni fue otra persona a quien le gustaba escuchar acerca de mis estudios.

Muchas gracias también a Juanjo y Silvi, por su amistad incondicional y su ayuda en momentos duros. Gracias también a Anna, Laiki, Ana y Angel, así como Xavi, Cristina y Michael.

También me gustaría dar las gracias a la gente de egarsat, especialmente al doctor Fallone y Salva, que hicieron un trabajo excelente en ponerme de una pieza otra vez.

Schliesslich möchte ich mich bei meiner Familie für die nimmermüde Unterstützung bedanken, die ich über die Jahre immer gespürt habe, und ohne die diese Arbeit nicht möglich gewesen wäre. Vielen Dank an meine Eltern Christa und Henning, an meine Schwester Kristin und an meinen Bruder Helge.

# A. List of Publications

- *Detection of Spin Precession in Freely Suspended Graphene Spin Valves on Cross-Linked Poly(methyl methacrylate)*
  Ingmar Neumann, Joris Van de Vondel, German Bridoux, Marius V. Costache, Françesc Alzina, Clivia M. Sotomayor Torres, and Sergio O. Valenzuela
  *Small* **9**, 156 (2012)

- *Enhanced spin accumulation at room temperature in graphene spin valves with amorphous carbon interfacial layers*
  Ingmar Neumann, Marius V. Costache, German Bridoux, Juan F. Sierra, and Sergio O. Valenzuela
  *Applied Physics Letters* **103**, 112401 (2013)

- *Spin Thermocouple*
  Ingmar Neumann, Juan F. Sierra, Marius V. Costache, and Sergio O. Valenzuela
  *in preparation*

- *Enhanced spin signal in nonlocal devices based on a ferromagnetic CoFeAl alloy*
  German Bridoux, Marius V. Costache, Joris Van de Vondel, Ingmar Neumann, and Sergio O. Valenzuela
  *Applied Physics Letters* **99**, 102107 (2011)

- *Magnon-drag thermopile*
  Marius V. Costache, German Bridoux, Ingmar Neumann, and Sergio O. Valenzuela
  *Nature Materials* **11**, 199-202 (2012)

- *Lateral metallic devices made by a multiangle shadow evaporation technique*
  Marius V. Costache, German Bridoux, Ingmar Neumann, and Sergio O. Valenzuela
  *Journal of Vacuum Science and Technology B* **30**, 04E105 (2012)

- *Fingerprints of Inelastic Transport at the Surface of the Topological Insulator $Bi_2Se_3$: Role of Electron-Phonon Coupling*
  Marius V. Costache, Ingmar Neumann, Juan F. Sierra, V. Marinova, M. M. Gospodinov, Stephan Roche, and Sergio O. Valenzuela
  *Physical Review Letters* **112**, 086601 (2014)

# B. Supplementary Material to Chapter 7

## B.1. Numerical Simulation of the Temperature Profile

In the following, we present results of a numerical simulation of the temperature profile of our devices. It is based on a solution of the steady state heat equation in two dimensions using the numerical calculation software COMSOL.

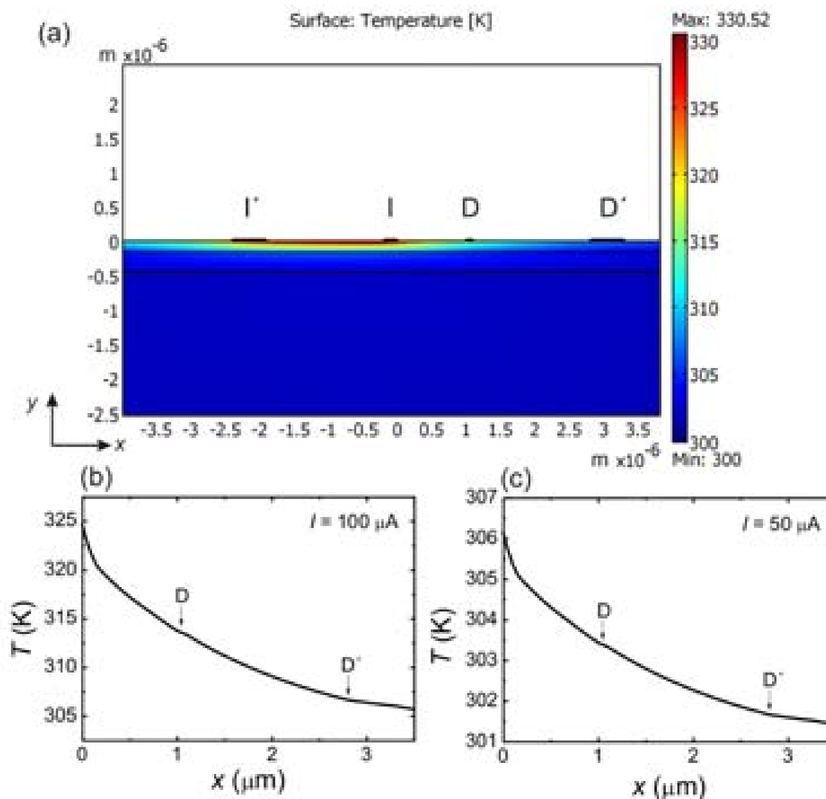


Figure B.1.: (a) Sample geometry used in the numerical calculation of the temperature profile, showing the temperature distribution for an injector current of $I = 100\,\mu\text{A}$ (b) Cross section of the temperature profile along the graphene for a current of $I = 100\,\mu\text{A}$, position of detectors indicated by arrows (c) Cross section for $I = 50\,\mu\text{A}$

The geometry of our model is schematically shown in Fig. B.1 (a). It consists of a 2D cross section of a graphene spin valve perpendicular to the axis of the FMs. Depending on the type of device, the substrate is either given by 300 $\mu$m/440 nm of Si/$SiO_2$ or of 300 $\mu$m/285 nm/200 nm of Si/$SiO_2$/PMMA. In the following, we present results of the numerical simulation of device Q1, which has a Si/$SiO_2$/PMMA substrate. Graphene is represented as a 1 nm thin layer, while the height of the FMs is 26 nm. The width of these FMs is, as shown in Fig. B.1 (a), 500/200/100/500 nm from left to right. The left two electrodes I and I′ serve as injector circuit, while the right two electrodes D and D′ are used to measure the non local voltages $V_{\mathrm{NL}}$. The center to center distance between I and D is $L = 1.15\,\mu$m, while the distance D to D′ is 2 $\mu$m.

The source of heat in our model is Joule heating of the injector circuit, consisting of the two Co electrodes as well as the graphene in between them. This can be written as $P_i = R_i I^2$, where the $R_i$ are the resistances of leads and graphene ($i = 1, 2, 3$). Dividing $P_i$ by the three dimensional volumes $V_i$ of these elements delivers $Q_i = P_i/V_i$. The external temperature is taken into account by the fact that we demand the bottom of the substrate to remain fixed at 300 K. Since the thickness of the Si layer is several orders of magnitude larger than those of the dielectric layers, this is a natural assumption.

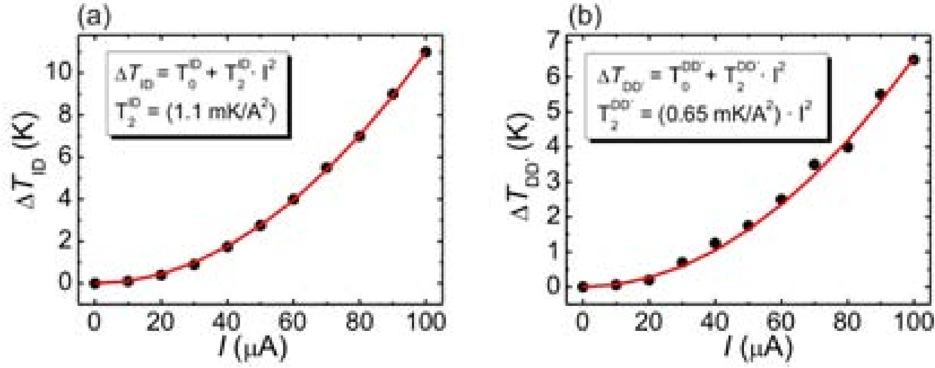


Figure B.2.: Temperature difference between injector I and detector D, $\Delta T_{\mathrm{ID}}$, and between D and D′, $\Delta T_{\mathrm{DD'}}$ as function of the bias current

The resulting heat profile for $I = 100\,\mu$A is shown on a false color scale in Fig. B.1 (a). As shown in the image for a bias current of $I = 100\,\mu$A, only the graphene sheet, $SiO_2$, PMMA and the FMs experience a non negligible deviation from room temperature.

Temperature profiles along the center of the graphene sheet are shown in Fig. B.1, for bias currents of $I = 100\,\mu$A in (b) and $I = 50\,\mu$A in (c). The position of the detectors D and D′ is indicated by arrows and visible as plateaus in the profile. The section between injector I and detector D is the range between $x = 0, ..., 1.05\,\mu$m. For a current of $I = 100\,\mu$A, the temperature close to the device rises to approx. 325 K.

In the following, we turn our attention to the temperature differences between in-

jector I and detector D, $\Delta T_{\mathrm{ID}}$ , and between D and D′, $\Delta T_{\mathrm{DD'}}$. In particular, we study their bias current dependence. Both $\Delta T_{\mathrm{ID}}$ and $\Delta T_{\mathrm{DD'}}$ are shown as a function of the bias current $I$ in Fig. B.2. We obtain these curves by repeatedly performing the numerical calculation of the entire geometry for varying injector currents, ranging from 10 to 100 $\mu$A. Then, we read out temperature profiles along the graphene, such as the ones shown in Fig. B.1, in order to obtain $\Delta T_{\mathrm{ID}}$ and $\Delta T_{\mathrm{DD'}}$. Examining their bias dependence, it becomes clear that both can be described by a parabolic model, delivering a straightforward relationship between $\Delta T$ and $I$. This proves especially useful in the analysis of the NLIVs, as it provides us, for instance, with the possibility of comparing the higher order fitting parameter $\Sigma$ with the Seebeck coefficient of graphene, as shown in section B.4.

Finally, the effect of the hot carriers mentioned in section 7.3.4 is not taken into account by the model, which can only be used to compute the temperature distribution of the lattice. At room temperature, these carriers exist only close to the injector, thus affecting only $\Delta T_{\mathrm{ID}}$. Therefore, while $\Delta T_{\mathrm{DD'}}$ is sufficiently accurate, $\Delta T_{\mathrm{ID}}$ underestimates the temperature difference between injector and detector.

## B.2. Non Local and Thermoelectric Voltage

The average non local voltage discussed throughout chapter 7 is given by $V_{\mathrm{th}} = (V^{\uparrow} + V^{\downarrow})/2$. It is the thermoelectric voltage one would detect in a non magnetic system, as we show in the following.

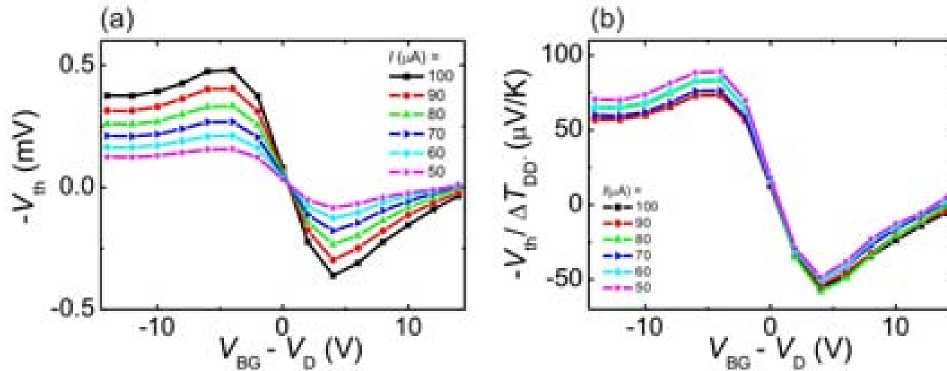


Figure B.3.: (a) Mean non local voltage $-V_{\mathrm{th}}$ as function of backgate voltage $V_{\mathrm{BG}}$ for different bias currents $I$ (b) -$V_{\mathrm{th}}/\Delta T_{\mathrm{DD'}}$ matches $S$ qualitatively and quantitatively.

Thermoelectric voltage and Seebeck coefficient of a material are related via eq. 2.3, $V_{\mathrm{th}} = -S\Delta T$. Experimentally, often both $V_{\mathrm{th}}$ as well as $\Delta T$ are measured in order to obtain $S$, such as in ref. [27]. Here, we use $V_{\mathrm{th}}$ obtained from averaging the detected non local voltages in parallel or anti parallel configuration of the FMs, as well as the

temperature difference $\Delta T_{\mathrm{DD'}}$ obtained from the numerical calculation. These deliver the Seebeck coefficient of graphene via $S = -V_{\mathrm{th}}/\Delta T_{\mathrm{DD'}}$, as shown in Fig. B.3.

In Fig. B.3 (a), the non local voltages in device Q1 are shown as a function of the backgate voltage, for bias currents ranging from 50 to 100 $\mu$A at room temperature. It can be seen that $-V_{\mathrm{th}}$ qualitatively resembles the Seebeck coefficient of graphene.

Scaling these voltage with $\Delta T_{\mathrm{DD'}}$ delivers the Seebeck coefficient of graphene. As shown in Fig. B.3 (b), the resulting $S$ is nearly independent of the measurement current. Moreover, the maximum of $S$ on the left side of $V_{\mathrm{D}}$ equals approx. 100 $\mu$V/K and the minimum on the right side of $V_{\mathrm{D}}$ equals approx. $-50$ $\mu$V/K, similar to the values reported in previous studies [27, 162].

These results show that the average non local voltage is indeed identical with the thermoelectric voltage measured in classical and semiclassical physics. In fact, the detected voltages in ref. [27] or any thermolectric element can be seen as non local voltage, although historically they are referred to as thermoelectric voltages.

## B.3. Temperature obtained via Mott Relation

At lower temperatures such as 77 K, the numerical model described in section B.1 does not provide reliable values because of the strong temperature dependence of the material parameters. However, we can estimate the temperature difference between the detectors, $\Delta T_{\mathrm{DD'}}$, by comparing $V_{\mathrm{th}}$ and $S_{\mathrm{Mott}}$.

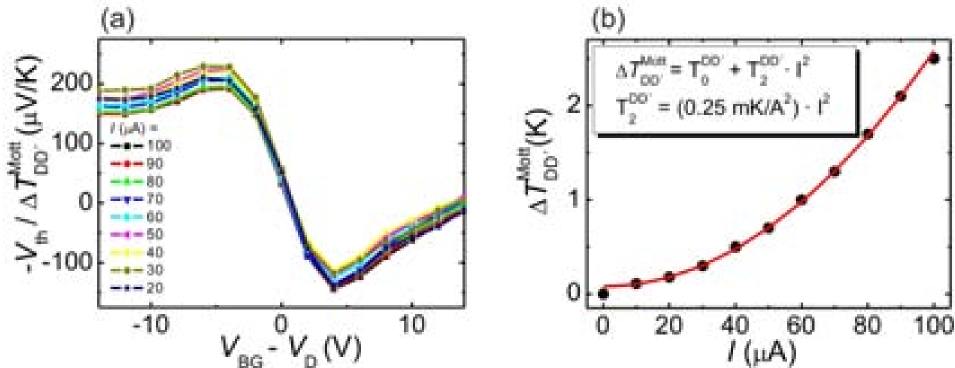


Figure B.4.: (a) Thermolelectric voltage $V_{\mathrm{th}}$ for different bias currents scaled by $\Delta T^{\mathrm{Mott}}_{\mathrm{DD'}}$ in order to match $S_{\mathrm{Mott}}$ (b) Temperature difference $\Delta T^{\mathrm{Mott}_{\mathrm{DD'}}}$ obtained by scaling between $V_{\mathrm{th}}$ and $S_{\mathrm{Mott}}$ as function of the bias

As described in chapter 2, the Mott relation delivers a method to calculate the Seebeck coefficient $S$ of graphene from the backgate dependent conductivity $\sigma$ of graphene. Here, we use the mesoscopic form of the Mott relation [161, 27, 162]. For room temperature and 77 K, $S_{\mathrm{Mott}}$ is shown in Fig 7.3 (d).

The relation $-V_{\mathrm{th}}/\Delta T_{\mathrm{DD'}} = S$ allows us to extract $\Delta T_{\mathrm{DD'}}$. This is shown in Fig. B.4. By matching $-V_{\mathrm{th}}$ and $S_{\mathrm{Mott}}$, we can extract $\Delta T_{\mathrm{DD'}}$ as scaling factor between them. In Fig. B.4 (a), this is shown for different currents. The resulting $\Delta T_{\mathrm{DD'}}$ as function of the current is shown in Fig. B.4 (b). As in case of the numerical calculation, we obtain a quadratic relation between $\Delta T_{\mathrm{DD'}}$ and $I$.

## B.4. Spin Dependent Seebeck Coefficients

Combining the results presented thoughout this appendix with the analysis of the NLIVs of chapter 7, we can gain a better understanding of the involved physics and obtain surprising results.

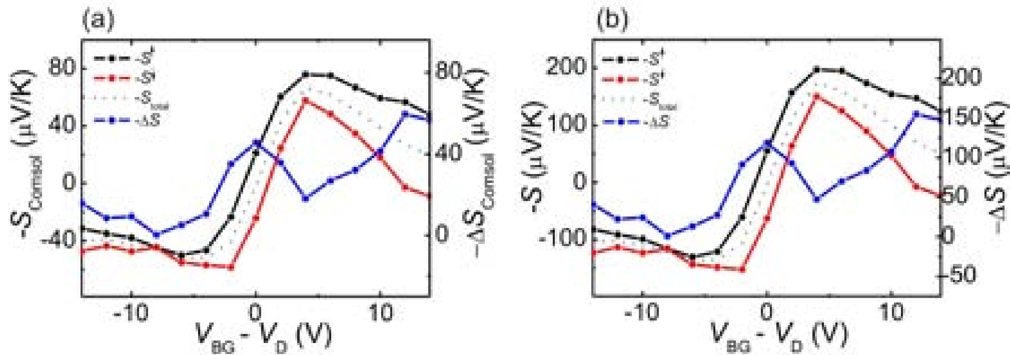


Figure B.5.: Spin dependent Seebeck parameters $S^{\uparrow}$ and $S^{\downarrow}$ obtained from higher order parameter $\Sigma^{\uparrow,\downarrow}$ (a) $S$ and $\Delta S$ according to the numerical simulation (b) $S$ and $\Delta S$ according to temperature differences obtained from Mott relation

As explained in chapter 7, we analyze the NLIVs using $V_{\mathrm{NL}} = V_0 + r_{\mathrm{NL}} I + \Sigma I^{\gamma}$, where we set $\gamma = 2$. Therefore, $\Sigma$ is the parameter describing second order effects. As we show in the following, $\Sigma^{\uparrow,\downarrow}$ can be identified with the Seebeck coefficients of spin up and down, $S^{\uparrow,\downarrow}$. This can be accieved using the relation between $\Delta T_{\mathrm{DD'}}$ and $I$. As discussed in section B.1, the numerical simulation of the temperature profile delivers a scaling factor of $0.65\,\mathrm{mK}/\mu\mathrm{A}^2$ between $\Delta T_{\mathrm{DD'}}$ and $I$. Therefore, $\Sigma$ and $S$ are related via $S^{\uparrow,\downarrow} = -(\Sigma^{\uparrow,\downarrow}/0.65)10^{-3}\,\mu\mathrm{V/K}$. The temperature difference obtained from the Mott relation, as shown in section B.3, delivers $S^{\uparrow,\downarrow} = -(\Sigma^{\uparrow,\downarrow}/0.25)10^{-3}\,\mu\mathrm{V/K}$.

The resulting $S^{\uparrow,\downarrow}$ are shown in Fig. B.5, together with $S = (S^{\uparrow} + S^{\downarrow})/2$ and $\Delta S = S^{\uparrow} - S^{\downarrow}$. In order to stress the similarity between $S$ and $\Sigma$ as shown in Fig. 7.7, we present the results in terms of $-S$. The average value $S$ is in good, quantitative agreement with values found in the literature [27, 162] and with the Seebeck coefficient obtained from the Mott relation, especially $S$ shown in Fig. B.5 (a).

The parameter $\Delta S$ is the spin dependent Seebeck coefficient, as defined as $S_{\mathrm{S}}$ in a previous work by Dejene *et al.* [168], where the authors investigate the spin dependent properties of ferromagnetic metals. Here, we study the non magnetic material

graphene, so it should be valid that $S^{\uparrow} = S^{\downarrow}$ and $\Delta S = 0$. However, due to the large spin accumulatiion, we observe a spin imbalance and $\Delta S \neq 0$. This means that we observe an *effective* spin dependent Seebeck effect in graphene, which leads to the enhancement of the non local signal and which we describe as spin thermocouple.

Finally, we can extract the effective spin dependent Seebeck coefficient $\Delta S$ of graphene. It shows a peak around the Dirac point, which is due to the properties of graphene. As we show in chapter 7, $\Delta S \propto dS/dV_{\mathrm{BG}}$. The values of $\Delta S$ lie in the range of 10 to $40\mu\mathrm{V/K}$, which is an order of magnitude larger than the spin dependent Seebeck coefficients of Co or NiFe [168].

# C. Recipes for the sample fabrication

All devices have been fabricated in a Raith-150$^{\mathrm{Two}}$ EBL system at an accelerating voltage of 30 keV.

**Fabrication of Graphene Devices on a Si-Substrate**

1. Patterning of a substrate with markers (5 nm Ti, 20 nm Au). Substrate: *p*-doped Si/$SiO_2$m, oxide thickness 440 nm or 285 nm
2. Mechanical exfoliation of graphene (Scotch tape)
3. Localization of graphene
4. Design of contacts
5. Spin-coating:
   2 layers PMMA 495 A2 at 2500 rpm (40 s), 1.5 min at 180$^o$ C 1 layer PMMA 950 A2 at 2500 rpm (40 s), 5 min at 180$^o$ C
6. EBL contacts: Dose 420 $\mu$C/cm$^2$
   Small features (contacts): Aperture 20 $\mu$m, stepsize 15 nm
   Leads: Aperture 120 $\mu$m, stepsize 15 nm
   Bondpads: Aperture 120 $\mu$m, stepsize 100 nm
7. Developing: MIBK:Isopropanol (1:3) for 30 s, isopropanol for 90 s
8. E-beam evaporation metal contacts (26 nm of Co), base pressure approx. $1 \cdot 10^{-7}$ mTorr, accelerating voltage 8 keV, Current approx. 50 mA
9. Lift-off in acetone and isopropanol

**Fabrication of Overexposed Graphene Samples (Type B in 6)**

1. Patterning of a substrate with markers (5 nm Ti, 20 nm Au). Substrate: *p*-doped Si/440 nm $SiO_2$
2. Mechanical exfoliation
3. Localization of graphene

4. Design of contacts

5. Overexposure by e-beam: Dose 9000 $\mu$C/cm$^2$, Aperture 20 $\mu$m, stepsize 15 nm

6. Spin-coating:
   2 layers PMMA 495 A2 at 2500 rpm (40 s), 1.5 min at 180$^o$ C
   1 layer PMMA 950 A2 at 2500 rpm (40 s), 5 min at 180$^o$ C

7. EBL contacts: Dose 420 $\mu$C/cm$^2$:
   Small features (contacts): Aperture 20 $\mu$m, stepsize 15 nm
   Leads: Aperture 120 $\mu$m, stepsize 15 nm
   Bondpads: Aperture 120 $\mu$m, stepsize 100 nm

8. Developing: MIBK:Isopropanol

9. E-beam evaporation metal contacts (26 nm of Co)

10. Lift-off

**Fabrication of Graphene Spin Valves using PMMA as Substrate (Suspended Graphene Spin Valves)**

1. Patterning of a substrate with markers (5 nm Ti, 20 nm Au). Substrate: *p*-doped Si/285 nm $SiO_2$

2. Spin coating:
   3 layers PMMA 950 A2 at 2500 rpm (40 s), 1.5 min at 180$^o$ C
   1 layers PMMA 950 A2 at 2500 rpm (40 s), 5 min at 180$^o$ C

3. Mechanical exfoliation

4. Localization of graphene

5. Design of contacts

6. Crosslinking of PMMA: Dose 9000 $\mu$C/cm$^2$, Aperture 20 $\mu$m, stepsize 15 nm
   Overexposure of large areas: Aperture 120 $\mu$m, stepsize 15 nm.
   Depending on the geometry of the overexposed area, either suspeded devices result or those using PMMA as substrate (Type C in chapter 6).

7. Spin-coating:
   2 layers PMMA 495 A2 at 2500 rpm (40 s), 1.5 min at 180$^o$ C
   1 layer PMMA 950 A2 at 2500 rpm (40 s), 5 min at 180$^o$ C

8. EBL contacts, dose 420 $\mu$C/cm$^2$:
   Small features (contacts): Aperture 20 $\mu$m, stepsize 15 nm
   Leads: Aperture 120 $\mu$m, stepsize 15 nm
   Bondpads: Aperture 120 $\mu$m, stepsize 100 nm
9. Developing in MIBK:Isopropanol
10. E-beam evaporation of metal contacts (26 nm of Co)
11. Lift-off in acetone and isopropanol

# D. List of Abbreviations

| | |
|---|---|
| FM | Ferromagnet |
| NM | Non Magnetic Material |
| I | Insulator |
| SC | Superconductor |
| AMR | Anisotropic MagnetoResistance |
| TMR | Tunneling Magnetoresistance |
| P | Parallel |
| AP | Anti Parallel |
| DOS | Density of States |
| NL | Non Local |
| NLSV | Non Local Spin Valve |
| EY | Elliot-Yafet |
| DP | D'yakonov-Perel |
| SLG | Single Layer Graphene |
| BLG | Bi Layer Graphene |
| FLG | Few Layer Graphene |
| MLG | Multi Layer Graphene |
| SEM | Scanning Electron Microscope |
| EBL | Electron Beam Lithography |
| PMMA | Poly(methyl methacrylate) |
| MIBK | Methyl Isobutyl Ketone |
| MBE | Molecular Beam Epitaxy |
| CVD | Chemical Vapor Deposition |
| AFM | Atomic Force Microscope |
| SDT | Spin Dependent Tunneling |
| MTJ | Magnetic Tunnel Junction |
| TEM | Transmission Electron Microscope |
| EBID | Electron Beam Induced Deposition |
| aC | Amorphous Carbon |
| Eq. | Equation |
| Fig. | Figure |

# Bibliography

[1] P. M. Tedrow and R. Meservey, Phys. Rev. Lett. **26**, 192 (1971).

[2] P. M. Tedrow and R. Meservey, Phys. Rev. B **7**, 318 (1973).

[3] M. Julliere, Phys. Lett. A **54**, 225 (1975).

[4] G. Binasch, P. Grünberg, F. Saurenbach, and W. Zinn, Phys. Rev. B **39**, 4828 (1989).

[5] M. N. Baibich, J. M. Broto, A. Fert, F. N. Van Dau, F. Petroff, P. Etienne, G. Creuzet, A. Friederich, and J. Chazelas, Phys. Rev. Lett. **61**, 2472 (1988).

[6] A. G. Aronov, JETP Lett. **24**, 32 (1976).

[7] A. G. Aronov and G. E. Pikus, Sov. Phys. Semicond. **10**, 698 (1976).

[8] M. Johnson and R. H. Silsbee, Phys. Rev. Lett. **55**, 1790 (1985).

[9] M. Johnson and R. H. Silsbee, Phys. Rev. B **37**, 5312 (1988).

[10] M. Johnson and R. H. Silsbee, Phys. Rev. B **37**, 5326 (1988).

[11] F. J. Jedema, A. T. Filip, and B. J. van Wees, Nature **410**, 345 (2001).

[12] S. O. Valenzuela and M. Tinkham, Nature **442**, 176 (2006).

[13] T. Kimura, Y. Otani, and J. Hamrle, Phys. Rev. Lett. **96**, 037201 (2006).

[14] T. Yang, T. Kimura, and Y. Otani, Nature Phys. **4**, 851 (2008).

[15] I. Žutič, J. Fabian, and S. D. Sarma, Rev. Mod. Phys. **76**, 323 (2004).

[16] S. O. Valenzuela, Int. J. Mod. Phys. B **23**, 2413 (2009).

[17] P. R. Wallace, Phys. Rev. **71**, 622 (1947).

[18] K. S. Novoselov, A. K. Geim, S. V. Morozov, D. Jiang, Y. Zhang, S. V. Dubonos, I. V. Grigorieva, and A. A. Firsov, Science **306**, 666 (2004).

[19] K. S. Novoselov, V. I. Fal´ko, L. Colombo, P. R. Gellert, M. G. Schwab, and K. Kim, Nature **490**, 192 (2012).

[20] A. H. Castro Neto, F. Guinea, N. M. R. Peres, K. S. Novoselov, and A. K. Geim, Rev. Mod. Phys. **81**, 109 (2009).

[21] A. K. Geim and K. S. Novoselov, Nature Mater. **6**, 183 (2007).

[22] D. Pesin and A. H. MacDonald, Nature Mater. **11**, 409 (2012).

[23] K. Uchida, S. Takahashi, K. Harii, J. Ieda, W. Koshibae, K. Ando, S. Maekawa, and E. Saitoh, Nature **445**, 778 (2008).

[24] G. E. W. Bauer, E. Saitoh, and B. J. van Wees, Nature Mater. **11**, 391 (2012).

[25] M. V. Costache, G. Bridoux, I. Neumann, and S. O. Valenzuela, Nature Mater. **11**, 199 (2012).

[26] A. A. Baladin, S. Ghosh, W. Bao, I. Calizo, D. Teweldebrhan, F. Miao, and C. N. Lau, Nanoletters **8**, 902 (2008).

[27] Y. M. Zuev, W. Chang, and P. Kim, Phys. Rev. Lett. **102**, 096807 (2009).

[28] A. A. Baladin, Nature Mater. **10**, 569 (2011).

[29] N. W. Ashcroft and N. D. Mermin, *Solid State Physics* (Saunders, Philadelphia, 1976).

[30] P. Drude, Annalen der Physik **1**, 566 (1900).

[31] P. Drude, Annalen der Physik **3**, 369 (1900).

[32] H. Schulz, *Physik mit Bleistift* (Verlag Harri Deutsch, Frankfurt am Main, 2001).

[33] M. Cutler and N. F. Mott, Phys. Rev. **181**, 1336 (1969).

[34] H. Ibach and H. Lüth, *Solid-State Physics* (Springer, Berlin Heidelberg, 2009).

[35] Y. Okimoto, K. Katsufuji, T. Ishikawa, A. Urushibara, T. Arima, and Y. Tokura, Phys. Rev. Lett. **75**, 109 (1995).

[36] R. A. de Groot, F. M. Mueller, P. G. van Engen, and K. H. Buschow, Phys. Rev. Lett. **50**, 2024 (1983).

[37] N. F. Mott, Proc. R. Soc. London, Ser. A **153**, 699 (1936).

[38] N. F. Mott, Proc. R. Soc. London, Ser. A **156**, 368 (1936).

[39] W. Thomson, Proc. R. Soc. London **8**, 546 (1857).

[40] P. C. van Son, H. van Kempen, and P. Wyder, Phys. Rev. Lett. **58**, 2271 (1987).

[41] S. Takahasi and S. Maekawa, Phys. Rev. B **67**, 052409 (2003).

[42] F. J. Jedema, *Electrical Spin Injection in metallic Mesoscopic Spin Valves* (PhD Thesis, Rijksuniversiteit Groningen, 2002).

[43] W. Hanle, Z. Phys. **30**, (1924).

[44] F. J. Jedema, H. B. Heersche, A. T. Filip, J. J. A. Baselmans, and B. J. van Wees, Nature **416**, 713 (2002).

[45] A. Slachter, F. L. Bakker, J.-P. Adam, and B. J. van Wees, Nature Phys. **6**, 879 (2010).

[46] L. Gravier, S. Serrano-Guisan, F. Reuse, and J.-P. Ansermet, Phys. Rev. B **73**, 024419 (2006).

[47] M. Hatami, G. E. W. Bauer, Q. Zhang, and P. J. Kelly, Phys. Rev. B **79**, 174426 (2009).

[48] A. Kretinin, G. L. Yu, R. Jalil, Y. Cao, F. Withers, A. Mishchenko, M. I. Katsnelson, K. S. Novoselov, A. K. Geim, and F. Guinea, arXiV:1309.2894 (2013).

[49] W. Demtröder, *Experimentalphysik 2* (Springer, Berlin, 1999).

[50] S. Kim, J. Nah, I. Jo, D. Shahrjerdi, L. Colombo, Z. Yao, E. Tutuc, and S. K. Banerjee, Appl. Phys. Lett. **94**, 062107 (2009).

[51] S. V. Morozov, K. S. Novoselov, M. I. Katsnelson, F. Schedin, D. C. Elias, J. A. Jaszczak, and A. K. Geim, Phys. Rev. Lett **100**, 016602 (2008).

[52] J. Balakrishnan, G. Kok Wai Koon, M. Jaiswal, A. H. Castro Neto, and B. Özyilmaz, Nature Phys. **9**, 284 (2013).

[53] A. Hoffmann, phys. stat. sol. (c) **4**, 4236 (2007).

[54] W. Hill, Ernie, K. Geim, Andre, K. S. Novoselov, F. Schedin, and P. Blake, IEEE Trans. Magn. **42**, 2694 (2006).

[55] N. Tombros, C. Jozsa, M. Popinciuc, H. T. Jonkman, and B. J. van Wees, Nature **448**, 571 (2007).

[56] S. Cho, Y.-F. Chen, and M. S. Fuhrer, Appl. Phys. Lett. **91**, 123105 (2007).

[57] M. Nishioka and A. Goldhaber, Appl. Phys. Lett. **2007**, 252505 (90).

[58] D. Huertas-Hernando, F. Guinea, and A. Brataas, Phys. Rev. B **74**, 155426 (2006).

[59] D. Huertas-Hernando, F. Guinea, and A. Brataas, Phys. Rev. Lett. **103**, 146801 (2009).

[60] R. J. Elliot, Phys. Rev. **96**, 266 (1954).

[61] Y. Yafet, *Solid State Physics, Vol. 14* (Academic, New York, 1963), p. 2.

[62] M. I. D´yakonov and V. I. Perel, Sov. Phys. Solid State **13**, 3023 (1971).

[63] S. Jo, D.-K. Ki, D. Jeong, H.-J. Lee, and S. Kettemann, Phys. Rev. B **84**, 075453 (2011).

[64] N. Tombros, S. Tanabe, A. Veligura, C. Jòzsa, M. Popinciuc, H. T. Jonkman, and B. J. van Wees, Phys. Rev. Lett. **101**, 046601 (2008).

[65] C. Jòsza, T. Maasen, P. M., P. J. Zomer, A. Veligura, H. T. Jonkman, and B. J. van Wees, Phys. Rev. B **80**, 241403(R) (2009).

[66] K. Pi, W. Han, K. M. McCreary, A. G. Swartz, Y. Li, and R. K. Kawakami, Phys. Rev. Lett. **104**, 187201 (2010).

[67] W. Han and R. K. Kawakami, Phys. Rev. Lett. **107**, 047206 (2011).

[68] I. Neumann, J. Van de Vondel, G. Bridoux, M. V. Costache, F. Alzina, C. M. Sotomayor Torres, and S. O. Valenzuela, Small **9**, 156 (2012).

[69] M. H. Diniz Guimarães, A. Veligura, P. J. Zomer, T. Maasen, I. J. Vera-Marun, N. Tombros, and B. J. van Wees, Nano Lett. **12**, 3512 (2012).

[70] F. Guinea, M. I. Katsnelson, and A. K. Geim, Nature Phys. **6**, 30 (2010).

[71] N. Levy, S. A. Burke, K. L. Meaker, M. Panlasigui, A. Zettl, F. Guinea, A. H. Castro Neto, and M. F. Crommie, Science **329**, 544 (2010).

[72] D. V. Tuan, F. Ortmann, D. Soriano, S. O. Valenzuela, and S. Roche, preprint, submitted to Nature Comm. .

[73] X. S. Li and *et al.*, Science **324**, 1312 (2009).

[74] J. Hackley, D. Ali, J. DiPasquale, J. D. Demaree, and C. J. K. Richardson, Appl. Phys. Lett. **95**, 133114 (2009).

[75] I. Forbeaux, J. M. Themlin, and J. M. Debever, Phys. Rev. B **58**, 16396 (1998).

[76] S. Neubeck, F. Freitag, R. Yang, and K. S. Novoselov, Phys. Status Solidi B **247**, 2904 (2010).

[77] P. Blake, E. W. Hill, A. H. Castro Neto, K. S. Novoselov, D. Jiang, R. Yang, T. J. Booth, and A. K. Geim, Appl. Phys. Lett. **91**, 063124 (2007).

[78] W. Demtröder, *Experimentalphysik 3* (Springer, Berlin, 2000).

[79] A. C. Ferrari, J. C. Meyer, V. Scardaci, C. Casiraghi, M. Lazzeri, F. Mauri, S. Piscanec, D. Jiang, K. S. Novoselov, and A. K. Geim, Phys. Rev. Lett. **97**, 187401 (2006).

[80] C. Binning, C. F. Quate, and C. Gerber, Phys. Rev. Lett. **56**, 930 (1986).

[81] Microchem datasheet PMMA, (2001).

[82] M. V. Costache, B. J. van Wees, and S. O. Valenzuela, in *One-Dimensional Nanostructures: Principles and Application*, edited by T. Zhai and J. Yao (John Wiley & Sons, Inc., 2012).

[83] I. Zailer, J. E. F. Frost, V. Chabasseur-Molyneux, C. J. B. Ford, and M. Pepper, Semicond. Sci. Technol. **11**, 1235 (1996).

[84] L. A. Ponomarenko, R. Yang, T. M. Mohiuddin, M. I. Katsnelson, K. S. Novoselov, S. V. Morozov, A. A. Zhukov, F. Schedin, E. W. Hill, and A. K. Geim, Phys. Rev. Lett. **102**, 206603 (2009).

[85] B. Huard, J. A. Sulpizio, N. Stander, K. Todd, B. Yang, and D. Goldhaber-Gordon, Phys. Rev. Lett. **98**, 236803 (2007).

[86] L. Bockhorn, P. Barthold, D. Schuh, W. Wegscheider, and R. J. Haug, Phys. Rev. B **83**, 113301 (2011).

[87] H. Schmidt, T. Lüdtke, P. Barthold, E. McCann, V. I. Fal´ko, and R. J. Haug, Appl. Phys. Lett. **93**, 172108 (2008).

[88] J. A. Liddle, G. M. Gallatin, and L. E. Ocola, Mat. Res. Soc. Symp. Proc. **739**, 19 (2003).

[89] L. P. Kouwenhoven, C. M. Marcus, L. McEuen, Paul, S. Tarucha, R. M. Westervelt, and N. S. Wingreen, in *Mesoscopic Electron Transport*, edited by L. Sohn, L. Kouwenhoven, and G. Schön (Kluwer, 1997).

[90] M. V. Costache, G. Bridoux, I. Neumann, and S. O. Valenzuela, J. Vac. Sci. Technol. B **30**, 04E105 (2012).

[91] G. Bridoux, M. V. Costache, J. Van de Vondel, I. Neumann, and S. O. Valenzuela, Appl. Phys. Lett. **99**, 102107 (2011).

[92] D. C. Elias, R. R. Nair, T. M. G. Mohiuddin, S. V. Morozov, P. Blake, M. P. Halsall, A. C. Ferrari, D. W. Boukhvalov, M. I. Katsnelson, A. K. Geim, and K. S. Novoselov, Science **323**, 610 (2009).

[93] J. Moser, A. Barreiro, and A. Bachtold, Appl. Phys. Lett. **91**, 163513 (2007).

[94] S. O. Valenzuela, D. J. Monsma, C. M. Marcus, V. Narayanamurti, and M. Tinkham, Phys. Rev. Lett. **94**, 196601 (2005).

[95] A. Messiah, *Quantum mechanics* (Amsterdam: North-Holland Publication, 1961).

[96] E. O. Kane, in *Tunneling Phenomena in Solids*, edited by E. Burstein and S. Lundqvist (Plenum Press, New York, 1969).

[97] R. Holm, J. Appl. Phys. **22**, 569 (1951).

[98] J. G. Simmons, J. Appl. Phys. **34**, 1793 (1963).

[99] C. K. Chow, J. Appl. Phys. **36**, 559 (1965).

[100] K. Gundlach, Solid State Electronics **9**, 949 (1966), provided by the SAO/NASA Astrophysics Data System.

[101] M. B. Stearns, J. Mag. Mag. Mater. **5**, 167 (1977).

[102] J. S. Moodera, L. R. Kinder, T. M. Wong, and R. Meservey, Phys. Rev. Lett. **74**, 3273 (1995).

[103] J. M. De Teresa, A. Barthélémy, A. Fert, J. P. Contour, F. Montaigne, and P. Seneor, Science **286**, 507 (1999).

[104] M. Wilczynski and J. Barnas, J. Appl. Phys. **88**, 5230 (2000).

[105] G. X. Miao and J. S. Moodera, J. Appl. Phys. **106**, 023911 (2009).

[106] S. Vutukuri, M. Chshiev, and W. H. Butler, J. Appl. Phys. **99**, 08K302 (2006).

[107] A. N. Chantis, K. D. Belashchenko, D. L. Smith, E. Y. Tsymbal, M. van Schilfgaarde, and R. C. Albers, Phys. Rev. Lett. **99**, 196603 (2007).

[108] G. Salis, S. F. Alvarado, and A. Fuhrer, Phys. Rev. B **84**, 041307(R) (2011).

[109] B. C. Min, J. C. Lodder, and R. Jansen, Phys. Rev. B **78**, 212403 (2008).

[110] D. L. Smith and P. P. Ruden, Phys. Rev. B **78**, 125202 (2008).

[111] S. Zhang and P. M. Levy, Eur. Phys. J. B **10**, 599 (1999).

[112] G. Eda and M. Chhowalla, Adv. Mater. **22**, 2392 (2010).

[113] F. Torrisi, T. Hasan, W. Wu, Z. Sun, A. Lombardo, T. S. Kulmala, G.-W. Hsieh, S. Jung, F. Bonaccorso, P. J. Paul, D. Chu, and A. C. Ferrari, ACS Nano **6**, 2992 (2012).

[114] H. Min, J. E. Hill, N. A. Sinitsyn, B. R. Sahu, L. Kleinman, and A. H. MacDonald, Phys. Rev. B **74**, 165310 (2006).

[115] T.-Y. Yang, J. Balakrishnan, F. Volmer, A. Avsar, M. Jaiswal, J. Samm, S. R. Ali, A. Pachoud, M. Zeng, M. Popinciuc, G. Güntherodt, B. Beschoten, and B. Özyilmaz, Phys. Rev. Lett. **107**, 047206 (2011).

[116] W. Han, K. M. McCreary, K. Pi, W. H. Wang, Y. Li, H. Wen, J. R. Chen, and R. K. Kawakami, J. Magn. Magn. Mat. **324**, 369 (2011).

[117] Y. Zhou and M. W. Wu, Phys. Rev. B **82**, 085304 (2010).

[118] X. Du, I. Skachko, A. Barker, and E. Y. Andrei, Nature Nanotech. **3**, 491 (2008).

[119] J. Martin, N. Akerman, G. Ulbricht, T. Lohmann, J. H. Smet, K. von Klitzing, and A. Jacoby, Nature Phys. **4**, 144 (2008).

[120] K. I. Bolotin, K. J. Sikes, Z. Jiang, G. Fundenberg, J. Hone, P. Kim, and H. L. Stormer, Solid State Commun. **146**, 351 (2008).

[121] M. Ishigami, J. H. Chen, W. G. Cullen, M. S. Fuhrer, and E. D. Williams, Nano Lett. **7**, 1643 (2007).

[122] K. R. Williams and R. S. Muller, J. Microelectromech. Sys. **5**, 256 (1996).

[123] K. R. Williams, K. Gupta, and M. Wasilik, J. Microelectromech. Sys. **12**, 761 (2003).

[124] J. Velasco Jr., Z. Zhao, H. Zhang, F. Wang, Z. Wang, P. Kratz, L. Jing, W. Bao, J. Shi, and C. N. Lau, Nanotechnology **22**, 285305 (2011).

[125] N. Tombros, V. Veligura, J. Junesch, J. J. van den Berg, P. J. Zomer, M. Wojtaszek, I. J. Vera-Marun, H. T. Jonkman, and B. J. van Wees, J. Appl. Phys. **109**, 093702 (2011).

[126] M. V. Costache, M. Zaffalon, and B. J. van Wees, Phys. Rev. B **74**, 012412 (2006).

[127] W. Han, K. Pi, W. Bao, K. M. McCreary, Y. Li, W. H. Wang, C. N. Lau, and R. K. Kawakami, Appl. Phys. Lett. **94**, 222109 (2009).

[128] L. Reimer, *Transmission Electron Microscopy-Physics of Image Formation and Microanalysis* (Springer, Berlin, 1997).

[129] D. Teweldebrhan and A. A. Baladin, Appl. Phys. Lett. **94**, 013101 (2009).

[130] A. Barreiro, F. Börrnert, S. M. Avdoshenko, B. Rellinghaus, G. Cunibert, M. H. Rümmeli, and L. M. K. Vandersypen, Sci. Rep. **3**, 1115 (2013).

[131] A. Eichler, J. Moser, J. Chaste, M. Zdrojek, I. Wilson-Rae, and A. Bachtold, Nature Nanotech. **6**, 339 (2011).

[132] N. N. Klimov, S. Jung, S. Zhu, T. Li, C. A. Wright, S. D. Solares, D. B. Newell, N. B. Zhitenev, and J. A. Stroscio, Science **336**, 1557 (2012).

[133] H. Dery, H. Wu, B. Ciftcioglu, M. Huang, Y. Song, R. K. Kawakami, J. Shi, I. Krivorotov, I. Žutič, and L. J. Sham, IEEE Trans. Electron Devices **59**, 259 (2012).

[134] S. Maekawa, S. O. Valenzuela, E. Saitoh, and T. Kimura, *Spin Current* (Oxford University Press, Oxford, 2012), pp. 177–305.

[135] W. Han, K. Pi, K. M. McCreary, Y. Li, J. J. I. Wong, A. G. Swartz, and R. K. Kawakami, Phys. Rev. Lett. **105**, 167202 (2010).

[136] T. Miyazaki and N. J. Tezuka, Magn. Magn. Mat. **139**, L231 (1995).

[137] S. S. P. Parkin, C. Kaiser, A. Panchula, P. M. Rice, B. Hughes, M. Samant, and S.-H. Yang, Nature Mater. **3**, 862 (2004).

[138] S. Yuasa, T. Nagahama, A. Fukushima, Y. Suzuki, and K. Ando, Nature Mater. **3**, 868 (2004).

[139] G. Mihajlović, D. K. Schreiber, Y. Liu, J. E. Pearson, S. D. Bader, A. K. Petford-Long, and A. Hoffmann, Appl. Phys. Lett. **97**, 112502 (2010).

[140] P. Laczkowski, L. Vila, V.-D. Nguyen, A. Marty, J.-P. Attanè, H. Jaffrès, J.-M. George, and A. Fert, Phys. Rev. B **85**, 220404(R) (2012).

[141] C. Zhang, Y. Wang, B. Wu, and Y. Wu, Appl. Phys. Lett. **101**, 022406 (2012).

[142] W. F. van Dorp and C. W. Hagen, J. Appl. Phys. **104**, 081301 (2008).

[143] P. Lemoine, S. S. Roy, J. P. Quinn, P. D. Maguire, and J. A. D. Mclaughlin, Appl. Phys. A **86**, 451 (2007).

[144] K. Rykaczewski, M. R. Henry, S.-K. Kim, A. G. Fedorov, D. Kulkarni, S. Singamaneni, and V. V. Tsukruk, Nanotechnology **21**, 035202 (2010).

[145] Y. Yoshikawa, S. Akita, and Y. Nakayama, J. Appl. Phys. **46**, L359 (2007).

[146] W. Han, W. H. Wang, K. Pi, K. M. McCreary, W. Bao, Y. Li, F. Miao, C. N. Lau, and R. K. Kawakami, Phys. Rev. Lett. **102**, 137205 (2009).

[147] M. Shiraishi, M. Ohishi, R. Nouchi, N. Mitoma, T. Nozaki, T. Shinjo, and Y. Suzuki, Adv. Funct. Mater. **19**, 3711 (2009).

[148] P. Barthold, T. Lüdtke, H. Schmidt, and R. J. Haug, New J. Phys. **13**, 043020 (2011).

[149] F. Xia, V. Perebeinos, Y.-m. Lin, Y. Wu, and P. Avouris, Nature Nanotech. **6**, 179 (2011).

[150] P. Blake, Sol. St. Commun. **149**, 1068 (2009).

[151] P. Lazìc, G. M. Sipahi, R. K. Kawakami, and I. Žutìc, preprint, submitted to Appl. Phys. Lett. (2013).

[152] W. Zhao, S. M. Kozlov, O. Höfert, K. Gotterbarm, M. P. A. Lorenz, F. Viñes, C. Papp, A. Görling, and H.-P. Steinrück, J. Phys. Chem. Lett. **2**, 759 (2011).

[153] Y. Fukuma, L. Wang, H. Idzuchi, S. Takahashi, S. Maekawa, and Y. Otani, Nature Mater. **10**, 527 (2011).

[154] C. Jòsza, M. Popinciuc, N. Tombros, H. T. Jonkman, and B. J. van Wees, Phys. Rev. B **79**, 081402(R) (2009).

[155] M. Popinciuc, C. Jòsza, P. J. Zomer, N. Tombros, A. Veligura, H. T. Jonkman, and B. J. van Wees, Phys. Rev. B **80**, 214427 (2009).

[156] J. C. t. Meyer, Phys. Rev. Lett. **108**, 196102 (2012).

[157] M. Johnson and R. H. Silsbee, Phys. Rev. B **35**, 4959 (1987).

[158] J. Flipse, F. L. Bakker, A. Slachter, F. K. Dejene, and B. J. van Wees, Nature Nanotech. **7**, 166 (2012).

[159] I. Neumann, M. V. Costache, G. Bridoux, J. F. Sierra, and S. O. Valenzuela, Appl. Lett. Phys. **103**, 112401 (2013).

[160] K. Grosse, M.-H. Bae, F. Lian, E. Pop, and W. P. King, Nature Nanotech. **6**, 287 (2011).

[161] M. Cutler and N. F. Mott, Phys. Rev. **181**, 1336 (1969).

[162] P. Wei, W. Bao, Y. Pu, C. N. Lau, and J. Shi, Phys. Rev. Lett. **102**, 166808 (2009).

[163] W. Han, W. H. Wang, K. Pi, K. M. McCreary, W. Bao, Y. Li, F. Miao, C. N. Lau, and R. K. Kawakami, Phys. Rev. Lett. **102**, 137205 (2009).

[164] I. J. Vera-Marun, V. Ranjan, and B. J. van Wees, Nature Phys. **8**, 313 (2012).

[165] A. C. Betz, F. Vialla, D. Brunel, C. Voisin, M. Picher, A. Cavanna, A. Madouri, G. Fève, J.-M. Berroir, B. Plaçais, and E. Pallecchi, Phys. Rev. Lett. **109**, 056805 (2012).

[166] D. K. Efetov and P. Kim, Phys. Rev. Lett. **105**, 256805 (2010).

[167] J. C. W. Song, M. Y. Reizer, and L. S. Levitov, Phys. Rev. Lett. **109**, 106602 (2012).

[168] F. K. Dejene, J. Flipse, and B. J. van Wees, Phys. Rev. B **86**, 024436 (2012).

Knowledge without understanding is pointless.